Orbital motion of substellar companions

Orbitbewegung substellarer Begleiter

Dissertation
zur Erlangung des akademischen Grades

doctor rerum naturalium (Dr. rer. nat.)

vorgelegt

dem Rat der Physikalisch-Astronomischen Fakultät
der Friedrich-Schiller-Universität Jena

VON **Dipl.-Phys. Christian Ginski**
GEBOREN AM 15. APRIL 1985 IN JENA

Gutachter

1. Prof. Dr. Ralph Neuhäuser, Astrophysikalisches Institut und Universitätssternwarte Jena

....

2. Prof. Dr. João Alves (Korreferent), Universität Wien, Institut für Astronomie

....

3. Prof. Dr. Peter H. Hauschildt, Universität Hamburg, Hamburger Sternwarte

....

Tag der Disputation: 20.11.2012
                       ....

For my Wife

Abstract

With the availability of adaptive optics systems at 8 m-class telescopes, the direct detection of low-mass companions such as brown dwarfs and giant Jupiter-like planetary-mass objects, in up to 200 pc from the Sun, is possible. Since this detection method is especially sensitive for wide companions, it is a very good complement to radial velocity and transit search programs.

The two common problems with these type discoveries are to ascertain if the candidate companion is orbiting the primary star, and to determine its mass to decide whether or not it is a substellar or even a planetary mass companion. Companionship is usually investigated by comparing the proper motion of the candidate companion to that of the primary star. If both objects are co-moving it is very likely that they are gravitationally bound. However, there is always the small chance of a coincidental alignment of the two objects, even more so if the primary star is a member of a young moving group or association (where almost all members have very similar proper motions). Only the detection of curvature of the orbit, meaning acceleration or deceleration in differential proper motion, can doubtlessly confirm that two objects are orbiting each other. Furthermore, the luminosity-age-mass models which are used to estimate the companion's mass are uncertain at very young ages (<10 Myr). Direct imaging surveys on the other hand target especially young associations, due to the more favoreable contrast ratio between primary star and low-mass companions. If significant orbital motion is detected, it is possible to fit Keplerian orbital elements for the companion and determine the system mass by Kepler's third law as generalized by Newton. Even if no curvature is detected, the detection of small differential motion can already be used to constrain the orbital elements of the system.

This work explores the possibilities of detecting orbital motion of six brown dwarf and planetary mass companions discovered over the past decade. Deep near-infrared (NIR) adaptive optics (AO) images were taken for each of the discussed targets, available archival data has been re-reduced, and literature data points were considered. As a result of this analysis, differential motion between primary stars and substellar companions could be clearly detected in three of the six discussed systems, namely HD 130948, DH Tau and GSC 08047-00232. In addition, there was marginal differential motion detected in the HD 203030 system. This differential motion is in all cases consistent with slow orbital motion, although no curvature of the orbits could yet be detected.

A method to constrain the orbital elements of the discussed systems was developed. The Least Squares Monte Carlo (LSMC) approach covers large areas of the parameter space by combining the random Monte Carlo approach with the ability of the Levenberg-Marquardt algorithm to find local minima. The LSMC fit was implemented with the PYTHON programming language. With this fitting program, the orbital parameters of the HD 130948 system and the GSC 08047-00232 system were successfully constrained.

Mit der Verfügbarkeit von Teleskopen der 8 m Klasse ist die direkte Detektion von massearmen Begleitern in einer Entfernung von bis zu $200\,\mathrm{pc}$ von der Sonne möglich. Da diese Detektionsmethode insbesondere geeignet ist um weite Begleiter zu detektieren, ergänzt sie hervorragend die erfolgreichen Radialgeschwindigkeits- und Transitsuchprogramme.

Die zwei wesentlichen Herausforderungen dieser Art von Entdeckungen sind zum einen die Verifikation, dass sich der gefundene Begleiterkandidat im Orbit um den Primärstern befindet, und zum anderen die Bestimmung der Masse des Begleiterkandidaten. Um festzustellen ob der Begleiterkandidat gravitativ an den Primärstern gebunden ist, wird normalerweise die Eigenbewegung der beiden Objekte am Himmel miteinander verglichen. Bewegen sich beide Objekte gemeinsam, so ist es sehr wahrscheinlich, dass sie auch gravitativ gebunden sind. Es sollte allerdings berücksichtigt werden, dass immer die Möglichkeit besteht, dass die beiden Objekte sich nur zufällig gleich bewegen. Dies ist insbesondere der Fall wenn der Primärstern ein Mitglied einer jungen Assoziation oder Eigenbewegungsgruppe ist (in beiden Fällen zeigen Mitglieder solcher Gruppen sehr ähnliche Eigenbewegungen). Nur die Detektion von Orbitkrümmung, d.h. Beschleunigung oder Abbremsung der differentiellen Eigenbewegung von Primärstern und Begleiter, kann ohne Zweifel bestätigen, dass beide Objekte sich im Orbit umeinander befinden. Des weiteren sollte berücksichtigt werden, dass die theoretischen Leuchtkraft-Alter-Masse Modelle, welche verwendet werden um die Begleitermasse zu bestimmen, bei jungen Systemaltern ($<10\,\mathrm{Myr}$) nicht gut kalibriert sind. In Beobachtungskampagnen zur direkten Detektion von massearmen Begleitern werden aber meist gerade junge Assoziationen untersucht, da hier der Kontrast zwischen Primärstern und massearmen Begleiter höher ist als bei älteren Objekten. Falls eine signifikante Orbitbewegung detektiert werden kann, so ist es möglich die Keplerschen Bahnelemente für den Begleiter zu bestimmen, um damit die Systemmasse mittels Newtons Version des dritten Keplerschen Gesetzes zu berechnen. Selbst wenn keine Orbitkrümmung detektiert werden kann, ist es möglich die Bahnelemente von Systemen anhand der geringen differentiellen Bewegung von Primärstern und Begleiter einzugrenzen.

Diese Arbeit untersucht die Möglichkeit der Detektion von Orbitbewegung von sechs Braunen Zwergen bzw. Begleitern mit planetarer Masse, welche in der vergangenen Dekade entdeckt wurden. Tiefe, durch adaptive Optik korrigierte, nah-Infrarot Aufnahmen wurden für jedes der diskutierten Systeme aufgenommen. Zusätzlich wurden verfügbare Archivaufnahmen ausgewertet und Literaturwerte berücksichtigt. Das Resultat dieser Analyse ist die klare Detektion von differentieller Bewegung zwischen Primärsternen und Begleitern in den Fällen von HD 130948, DH Tau und GSC 08047-00232. Des weiteren wurde eine marginale Bewegungsdifferenz auch im Falle des HD 203030 Systems detektiert. Die gefundenen differentiellen Bewegungen sind in allen Fällen konsistent mit langsamen Orbitbewegungen. Es konnte allerdings bisher keine Orbitkrümmung detektiert werden.

Eine Methode zur Einschränkung der Bahnelemente der diskutierten Systeme wurde entwickelt. Die Methode der kleinsten Quadrate wurde hierfür mit einem Monte Carlo Ansatz kombiniert. Diese Herangehensweise deckt große Bereiche des Parameterraums ab, während

gleichzeitig lokale Minima mittels des Levenberg-Marquardt Algorithmus gefunden werden können. Ein Programm zur Durchführung dieser Untersuchungsmethode wurde in der Programmiersprache PYTHON geschrieben. Mit diesem Programm konnten die Bahnelemente des HD 130948 Systems und des GSC 08047-00232 Systems erfolgreich eingeschränkt werden.

Acknowledgements

I have to thank many people for their direct or moral support before and during the creation of this dissertation.

First and foremost I want to thank my doctoral advisor Prof. Dr. Ralph Neuhäuser for suggesting and mentoring this PhD thesis. I highly appreciate his continued support and trust.

I also want to thank Dr. Markus Mugrauer for his guidance throughout the creation of my Diploma thesis and the following 3 years as PhD student. I learned a great deal from him, especially during our shared observation projects at the Calar Alto Observatory in Spain.

The time at the AIU Jena in general has been one of the most professionally and socially rewarding in my life. I want to thank all my colleagues there, some of which have meanwhile become good friends.

In particular I would like to thank Dr. Tobias Schmidt for his helpfulness whenever I came across a problem in the past 3 years. I also had many fruitful discussions with Dr. Thomas Eisenbeiß and Dr. Markus Hohle for which I am very grateful. Furthermore I want to thank Dr. Tristan Röll for introducing me to the Python programming language which was used as the primary tool for all research conducted in this thesis. Additionally, the many wide ranged and critical discussions we conducted taught me to question everything and in particular myself, which in turn, I believe, made me a better scientist.

In addition, to the scientific staff at the AIU I would like to thank Jürgen Weiprecht for the computer support and Monika Müller for all the administrative problems she solved for me. Besides my friends and colleagues at the AIU, I am deeply indebted to my family, who supported me throughout my entire life. Without my mother Silke Ginski, my grandmother Gisela Mäder and my aunt Kerstin Mäder, I would not be who and what I am at this point of my life.

At last I want to thank the most important person in my life. The one who supported me like no one else and kept me sane during the creation of this thesis. The most brave and kind person that I have the priviledge to know, my loving wife Donna Keeley.

Contents

List of Figures

List of Units

This work employs units of measurement which are commonly used in astronomy, but which are not part of the SI unit system. In the following, these units are defined and the conversion to SI units is given.

1 AU (Astronomical Unit) is the mean distance between Earth and Sun.
$$1\,\text{AU} = 1.49597871 \cdot 10^{11}\,\text{m}$$

1 pc (Parsec) is the distance at which an object has a parallax angle of 1 arcsec with respect to 1 AU.
$$1\,\text{pc} = 2.06264834 \cdot 10^5\,\text{AU} = 3.08567800 \cdot 10^{16}\,\text{m}$$

1 arcsec (Arc Second) is a unit of angular measurement that equals the 21600th part of a circle. 1 arcsec is also written as 1".
$$1\,\text{arcsec} = \frac{1}{3600}^{\circ} = \frac{\pi}{10800}\,\text{rad}$$

1 mas (Milliarcsecond) is the 1000th part of an arc second.
$$1\,\text{mas} = 10^{-3}\,\text{arcsec} = \frac{\pi}{10800000}\,\text{rad}$$

1 M$_\odot$ (Solar rest mass) is the rest mass of the sun.
$$1\,\text{M}_\odot = 1.9889 \cdot 10^{30}\,\text{kg}$$
$$1\,\text{M}_\odot \approx 1048\,\text{M}_{Jup}$$

1 M$_{Jup}$ (Jovian rest mass) is the rest mass of Jupiter.
$$1\,\text{M}_{Jup} = 1.8996 \cdot 10^{27}\,\text{kg}$$
$$1\,\text{M}_{Jup} \approx 9.6 \cdot 10^{-4}\,\text{M}_\odot$$

JD (Julian Date) is the date in days counted from January 1st 4713 B.C., 12:00 noon.

1   Introduction

Planets move in ellipses with the Sun at one focus.
Johannes Kepler

Over 400 years ago Johannes Kepler published his first two laws of planetary motion in *Astronomia nova*, revolutionizing astronomical calculations. Since then, our understanding not only of celestial mechanics, but also of the universe in general has greatly improved. In an attempt to understand our own solar system and therefore to some extent our place in the universe, we use telescopes of the 8 m class to image giant extrasolar planets. We do this in order to understand extrasolar systems in the same way that Kepler tried to understand our own.

1.1   Planet and brown dwarf definition and formation

The International Astronomical Union (IAU) decided upon a definition of the term "planet" at its general assembly on 2006 August 24. Thereby, an object must fulfill the following three criteria to be called "planet":

(i) It is a celestial object in orbit around the Sun.

(ii) It has sufficient mass for its self-gravity to overcome rigid body forces so that it assumes a hydrostatic equilibrium (nearly round) shape.

(iii) It has cleared the neighbourhood around its orbit.

While this new definition is straightforward for most bodies in the solar system, it completely ignores the issue of very low mass objects found as companions to stars other than the sun. Even if one was to replace "Sun" with the more generic "Star", the definition would be very impractical for extrasolar objects, since it is currently not possible to resolve very low mass objects to check for their shape or to determine whether there are additional objects of even lower mass in a similar orbit. Hence it is necessary to find another way of defining planets and other low-mass substellar objects, even if it is an "unofficial" definition.

There are several ways that have been considered to distinguish between substellar objects and low-mass stars. Theoretically, objects with masses below $0.078\,M_{\odot}$ are not able to ignite core hydrogen burning by means of their own gravity (Burrows et al. 1997). Therefore, this could be used as a mass limit to separate stellar and substellar objects. Objects below that mass limit are, however, still able to burn deuterium. Since the planets in our own solar system are non-fusors, it is necessary to further distinguish between substellar objects. The theoretical mass limit for deuterium burning is $0.0124\,M_{\odot}$. Thus objects below this mass limit could be called "planet", while objects with masses between $0.0124\,M_{\odot}$ and $0.078\,M_{\odot}$

belong in the "brown dwarf" regime. Brown dwarfs distinguish themselves from low-mass stars in that they never reach the main sequence, since they cannot establish stable hydrogen burning. In addition, the interior of brown dwarfs is partially degenerated[1] (see, e.g. Chabrier et al. 2000). In Fig. 1, evolutionary tracks by Burrows et al. (1997) for low-mass stars, brown dwarfs and planets are shown. While stars assume a stable luminosity after an initial phase of contraction, brown dwarfs and planets are just cooling down and hence becoming less luminous over time.

The discussed mass limits as defining factors for planets and brown dwarfs have, however, several disadvantages. The mass limits are not sharp boundaries, since the ability to ignite hydrogen or deuterium fusion also depends on other factors such as metallicity or density of the objects (Spiegel et al. 2011). Consequently there might be a whole class of borderline objects which burned some of their deuterium or hydrogen for a short amount of time. In addition, Lucas and Roche (2000) report the discovery of more than a hundred free-floating objects in the brown dwarf and planetary mass regime from their deep imaging survey in Trapezium. Similar results are reported by Sumi et al. (2011), who conducted a microlensing survey of the Galactic Bulge. This raises the question whether such free-floating objects should be regarded as planets even if they are in the mass range below $0.0124 \, M_\odot$, since this condradicts the general idea of a low-mass object orbiting a star. Furthermore, the mass of an object is not a directly observable value, but needs to be inferred either from luminosity and spectra in combination with theoretical models, or from orbit determinations which might not be easily obtainable depending on the individual systems (for further discussion of this problem see section 1.2).

Another school of thought is to distinguish between low-mass stellar objects, brown dwarfs and planets by means of their formation. The general idea is that objects which form by gravitational collapse of dust clouds or fragmentation of circumstellar dust disks could be regarded as low-mass stars or brown dwarfs (see for example Heacox 1999), while objects which form by core accretion could be defined as planets. There is, however, still an ongoing discussion on formation scenarios of substellar companions. It might be that the different types of formation are not distinct, but rather that a combination of different effects leads to the formation of brown dwarfs and planets as well as low-mass stars (see e.g. Boss 1997, Boss 2002). Additionally, it is usually not possible to infer from observational values how an individual object has formed, although there might be some indication in the shape of the orbit, e.g. as reported in Ribas and Miralda-Escudé (2007).

Finally, it is observed that there is an underabundance of objects with masses between roughly $\sim 0.025 \, M_\odot$ and $0.078 \, M_\odot$ at close ($< 5 \, \mathrm{AU}$) separations to their host stars. This area is usualy referred to as the "brown dwarf desert" (see e.g. Grether and Lineweaver 2006). In Fig. 2(a) companion mass versus orbit period is plotted for companions to

---

[1]The core density of brown dwarfs increases faster than the core temperature, due to ineffective gravitational heating at low masses. The density reaches the point where electrons become quantum-mechanically degenerated due to the Pauli principle before the temperature is high enough to ignite core hydrogen burning (see, e.g. §8.3.2 in Unsöld and Baschek 1988).

solar-type stars (Grether and Lineweaver 2006). While many stellar and planetary mass companions have been detected, there are no brown dwarfs in that orbit period range. Additionally, Fig. 2(b) shows the mass histogram of all planetary mass companions detected so far, which are listed at *exoplanet.eu* by Schneider et al. (2011). Only published objects with a (minimum) mass smaller than $0.025\,M_\odot$ are considered, as this is the mass limit adopted by Schneider et al. (2011). The mass distribution falls exponentially towards higher masses, which could indicate that the brown dwarf desert extends into wider separations. One should, however, note that over 90 % of the companions listed in *exoplanet.eu* are found by radial velocity and transit search programs (for further explanation see section 1.2), and are therefore highly biased towards short periods. There are also other studies which found that the brown dwarf desert does not seem to extend to wide separations, e.g. Gizis et al. (2001). It is a matter of discussion if the brown dwarf desert at short periods is a direct result of formation mechanisms. Brown dwarfs formed by gravitational instability at the same time as their host star might not be able to survive but are rather consumed by the primary within a short period of time.

In summary, the definition of planets around stars other than the sun, as well as brown dwarfs, is still a matter of ongoing discussion. Since there are good arguments for and against all of the above considerations, an upper mass limit of $0.0124\,M_\odot$ is choosen for planetary mass objects in this work, and $0.078\,M_\odot$ for brown dwarfs.
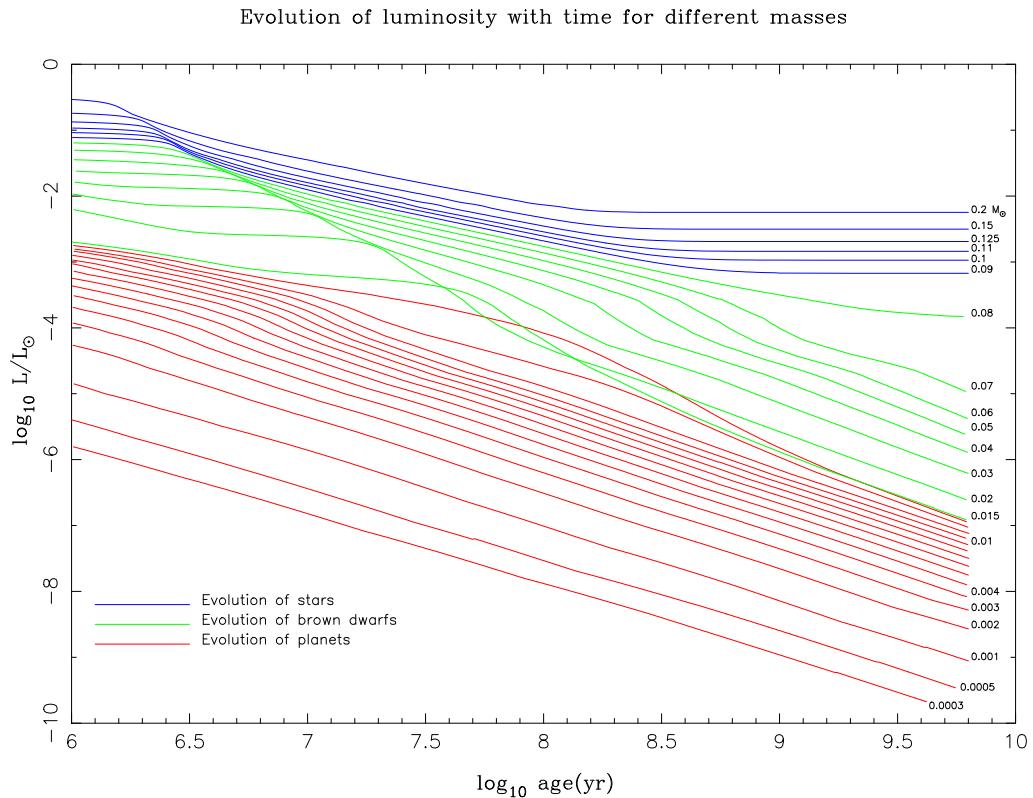
Figure 1: Diagram by Burrows et al. (1997) showing luminosity versus age of low mass stars, brown dwarfs and extrasolar giant planets.
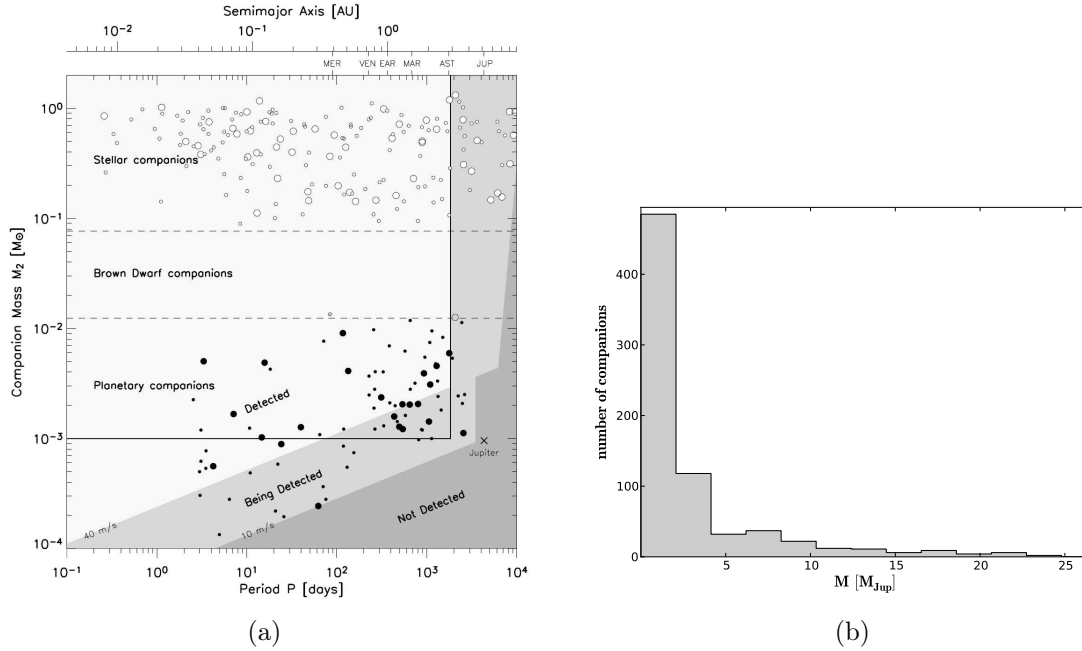
Figure 2: *Left:* Minimum mass versus semi-major axis and orbit period for substellar and stellar companions to solar analogs, detected via radial velocity measurements (Grether and Lineweaver 2006). The area of non-detections due to the current sensitivity limit of the radial velocity technique is marked in dark grey, while the area within the sensitivities of current surveys is marked in light grey. The area between $0.013\,\mathrm{M_\odot}$ and $0.08\,\mathrm{M_\odot}$ is marked as brown dwarf desert. *Right:* Mass histogram of all planetary mass objects discovered by different methods. Minimum mass was used for objects discovered by the radial velocity technique. All data was collected from *exoplanet.eu* by Schneider et al. (2011).

1.2   Detection methods of substellar companions

The search for substellar companions is perhaps one of the most challenging endeavors in the field of astronomical research in the past twenty years. Nevertheless, several different detection methods have been applied successfully, leading to the discovery of 760 planet candidates in 609 systems to date (all planet candidates listed in *exoplanet.eu* by Schneider et al. 2011).

The most successful method by far is the measurement of Doppler shifts of stellar spectral lines, due to periodic changes of the radial velocity of the observed star. Such periodic changes in radial velocity would be expected if another body is present in the system and thereby introducing a "wobble movement" to the primary star, as both objects are orbiting around their common center of mass. This method was already proposed sixty years ago by Struve (1952), but was not feasible at the time due to low precision of the available instruments. The first radial velocity planet candidate was discovered by Mayor and Queloz (1995). Today over 90 % of known planet candidates have been discovered or confirmed by this technique. Despite these successes, this particular technique also has a few disadvantages. Due to the unknown orbit inclination (see also section 1.3), only the minimum mass $m \cdot \sin i$ can be calculated, and hence some of the detected objects will be more massive

and might rather be brown dwarfs than planetary mass objects. Also, the technique is most sensitive to objects of high masses with short orbital periods. Thus the detected planet candidate sample is highly biased towards such objects.

Another very successful detection method for substellar companions is the transit technique. To find a substellar object, one monitors the luminosity of a given star. In the case of an (spatially unresolved) object passing between the primary and the observer, the luminosity first decreases and later increases again as the transit event ends. The great advantage of the transit method is that it allows measurement of the radius of an unresolved object via fitting of the respective transit lightcurve. Additonaly, in cases where the radial velocity signal of a discovered transit object can be measured, this allows calculation of the mass of the object, since the inclination of the orbit must be close to $90°$ for a transit event to occur. With mass and radius one can then calculate the density of the discovered objects and can therefore estimate their composition. A large number of such transiting objects has recently been discovered by the "Kepler" space mission (Borucki et al. 2010). It is however remarkable, that the transit search technique can also be employed on telescopes of the $\sim 1\,$m class, e.g. as done by Alonso et al. (2004), Pollacco et al. (2006), and Neuhäuser et al. (2011a). As with radial velocity measurements, the transit technique also has the disadvantage of a high bias towards detection of objects with very short orbital periods. Additionally, the possibility of detecting false positives such as eclipsing binaries with gracing ecplises exist.

In this work, objects detected by direct imaging are discussed. The direct imaging technique employs telescopes of the $8\,$m class to spatially resolve substellar companions to nearby (typically within $100\,$pc) stars. Direct imaging surveys such as Neuhäuser et al. (2005), Schmidt et al. (2008) and Chauvin et al. (2010), have discovered 31 extrasolar planet candidates to date, and even more wide brown dwarf companions, thereby filling an important gap in the detection space of substellar companions. In Fig. 3 (minimum) mass versus (projected) separation is shown for all planetary mass companions discovered by 2nd of March 2012 (data as given at *exoplanet.eu* by Schneider et al. 2011). While radial velocity and transit surveys are most sensitive to very close companions ($< 2\,$AU), the direct imaging technique can discover objects with projected separations typically larger than $10\,$AU.

The two common problems one faces after direct detection of a companion candidate are determining the mass of the object and if it is physically associated with the primary star. There are two established criteria to test for companionship:

(i) Multiple images in different observing epochs can be taken to confirm that the companion candidate is co-moving with the primary star.

(ii) Photometry and spectra can be taken to confirm that the object is low-mass and of a similar age as the primary star.

Most direct imaging surveys concentrate on young nearby moving groups or associations, since brown dwarfs and giant planetary mass objects are more luminous at young ages

($< 100\,$Myr), as can be seen in Fig. 1. Two members of the same moving group would, however, exhibit a similar age and motion on the sky. It is therefore possible that even close companion candidates are just members of the same moving group as their primary star, which happen to have a small projected separation, but are located at slightly different distances.

The mass of a companion can be determined by comparing its brightness with luminosity-mass models such as the DUSTY models presented in Chabrier et al. (2000). In the case of substellar objects, such models are highly degenerated with the age of the objects, since neither brown dwarfs nor planetary mass objects are massive enough to start hydrogen burning and therefore never reach the main sequence. Instead they are just cooling after their initial phase of contraction and possibly deuterium burning.

Rather than comparing the objects' luminosity with luminosity-mass-age models, one can also take high resolution spectra of the objects and compare them with model spectra of substellar atmospheres such as the DRIFT-PHOENIX models by Helling et al. (2008). From spectra it is possible to determine temperature and surface gravity. Luminosity and temperature give the radius of the object, and with radius and surface gravity it is possible to calculate the object's mass (as done in e.g. Schmidt et al. 2008).

However, imaging surveys for substellar companions concentrate mainly on young objects, due to the more favorable contrast ratio between primary star and companion. At young ages, the aforementioned theoretical models are more uncertain, because the starting conditions of the model simulations are still influencing the results (see Baraffe et al. 2002), and the formation processes of brown dwarfs and planetary mass objects are not yet completely understood. Hence models might under- or overestimate the masses of substellar companions.
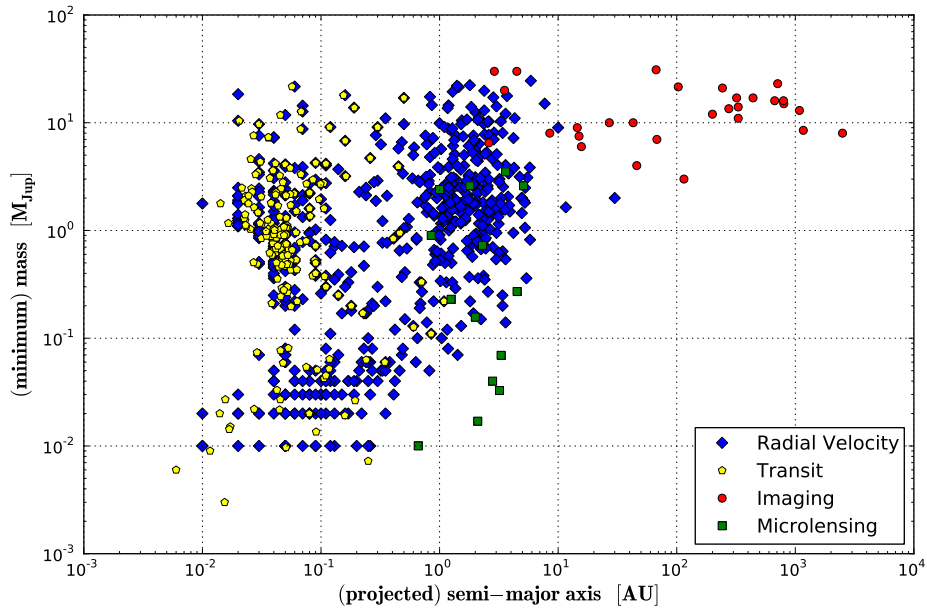
Figure 3: Mass versus separation of extrasolar giant planets as listed in *exoplanet.eu* by Schneider et al. (2011). Each planet has been color-coded according to its discovery method.

1.3   Keplerian orbits and orbital elements

The orbital motion of two objects around their common center of mass is a classical two-body problem and can therefore be described analytically. According to Kepler's first law, both bodies move around the center of mass in ellipses. To fully describe the system, one would have to determine semi-major axis and eccentricity for both orbits, as well as a reference point for each orbit that is occupied by the orbiting object at a given time. In addition, unlike in theoretical considerations, it is not possible to freely choose the point of observation, hence the orientation of the orbit in regard to the observer on Earth needs to be described. In total, two sets of six parameters are needed to describe the movement of two objects of known mass which are bound by gravity. For practical reasons, this system of parameters is usually halved by describing the movement of the less massive or luminous body in regard to the heavier and brighter one. The remaining parameters are the "orbital elements" of the system (see e.g. Montenbruck 2005):

Semi-major axis (a) of the orbit ellipse is directly related to the orbital period (P) by Kepler's third law $4\pi^2 a^3 = G(M_1 + M_2)P^2$

Eccentricity (e) of the orbit. In case of a circular orbit $e = 0$, whereas $e \in (0,1)$ for an elliptical orbit. If $e \geq 1$ the orbit is not closed and has a parabolic ($e = 1$) or hyperbolic ($e > 1$) shape.

Inclination (i) is the angle between the orbital plain and the reference plane. The reference plane is the sphere of the sky. The inclination can assume values from $0°$ to

180°, where 0° and 180° mean that the orbit is observed face-on, while an inclination of 90° means that the orbit is observed edge-on. Values between 0° and 90° indicate a prograde orbit, while values between 90° and 180° indicate a retrograde orbit.

Longitude of the ascending node (Ω) is the angle between the reference direction and the line of intersection of orbit and reference plane. The reference direction in the context of this work is north. Ω is measured from north over east towards the point in the line of intersection where the orbiting object is emerging from the reference plane (the so-called "ascending node").

Argument of periastron (ω) is the angle between the ascending node and the direction of the periastron, measured in the direction from north to east.

Time of periastron passage ($\mathbf{T}_0$) is the Julian date at which the orbiting body passes through its periastron.
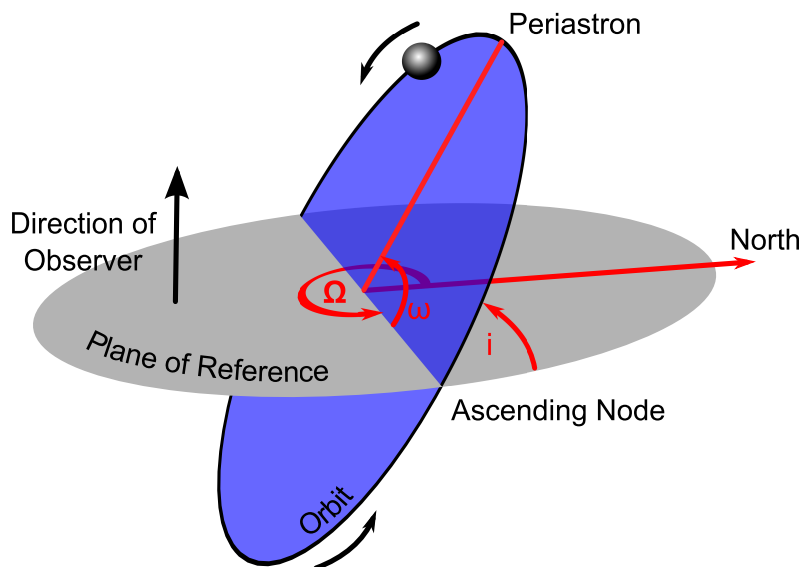
Figure 4: Schematics of the angular orbital elements of the Keplerian orbit.

The orienting angles of the orbit i, Ω and ω can be seen in Fig. 4. If all orbital elements are known, the position of the orbiting body in regard to the primary body can be calculated at any given time. To fit the orbital elements of a given system with unknown masses of the orbiting bodies, a minimum of four astrometric measurements (consisting of separation of both objects and position angle of the companion) are necessary, since in this case the system posseses seven degrees of freedom (6 orbital elements and the mass of the system). The detection of orbital motion of a substellar companion around a primary star would ascertain that both objects are bound by gravity, and would, at the same time, allow the total system mass to be calculated dynamically by Kepler's third law. Orbital motion can be detected as differential proper motion between primary star and companion. Due to the large projected separations of companions found by imaging, in most cases one will only be

able to detect a linear trend in separation and position angle (PA) of the companion over time, as was recently done in the cases of GQ Lup b by Neuhäuser et al. (2008), TWA 5 b by Neuhäuser et al. (2010) and HR 7329 B by Neuhäuser et al. (2011b). However, even such a linear trend can be used to constrain possible orbits of the system. If curvature of the orbit is detected, i.e. an acceleration or deceleration of differential proper motion, it is possible to fit and constrain the orbital elements even more precisely.

This work explores the possibilities of detecting orbital motion of several brown dwarf and planetary mass companions discovered over the past decade. Deep near-infrared (NIR) adaptive optics (AO) images were taken for each of the discussed targets, available archival data has been re-reduced, and literature data points were considered. Observation strategy and data reduction are described in detail, with special emphasis on the astrometric calibration. The relative proper motion of primaries and companions is examined and a strategy to constrain the orbital elements is introduced. In addition, detection limits for all deep observations are computed.

I don't pretend we have all the answers. But the questions are certainly worth thinking about.

Arthur C. Clarke

2 Target sample

In the following the target systems of this study are each briefly characterized. Their properties are then compared to the whole population of known, directly imaged substellar companions in section 2.2. At the end of this section, an overview over the most important properties of each target system is given in Tab. 1.

2.1 Individual Targets

2.1.1 HD 130948

The star HD 130948 is a young solar analog located at $\alpha = 14^h\,50^m\,15^s.81$ and $\delta = 23°\,54'\,42''.6$ (van Leeuwen 2007) in the constellation of Boötes at a distance of $18.17 \pm 0.11\,\mathrm{pc}^2$ (van Leeuwen 2007). Its spectral type is G 1 V (Chen et al. 2000), and its age was recently determined by Dupuy et al. (2009) to be $0.79^{+0.22}_{-0.15}\,\mathrm{Gyr}$ using gyrochronology[3]. Due to its proximity it exhibits a high proper motion of $143.91 \pm 0.37\,\mathrm{mas/yr}$ in right ascension and $32.69 \pm 0.34\,\mathrm{mas/yr}$ in declination (van Leeuwen 2007).

Potter et al. (2002) discovered a binary brown dwarf companion 2.64 ± 0.01 arcsec southeast of the primary, using the Gemini North telescope with the Hokupa'a AO (Graves et al. 1998) and the QuIRC instrument (**Qu**ick **I**nf**r**a**r**ed **C**amera, Hodapp et al. 1996). The discovery image is shown in Fig. 5. They determined the absolute infrared magnitudes to be $M_J = 12.6 \pm 0.2\,\mathrm{mag}$, $M_H = 11.9 \pm 0.1\,\mathrm{mag}$, $M_K = 11.0 \pm 0.1\,\mathrm{mag}$ and $M_J = 12.9 \pm 0.2\,\mathrm{mag}$, $M_H = 12.3 \pm 0.1\,\mathrm{mag}$, $M_K = 11.3 \pm 0.1\,\mathrm{mag}$ for the B and C component respectively. Considering the models of Chabrier et al. (2000), they estimated a mass of less than $0.075\,\mathrm{M}_\odot$ for the B component and less than $0.065\,\mathrm{M}_\odot$ for the C component. They also took medium-resolution spectra of both binary components with the Keck
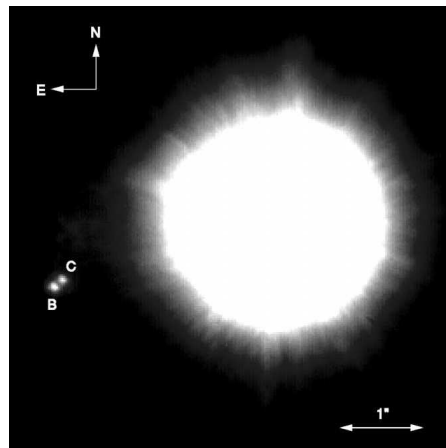
Figure 5: Discovery image of the companions to HD 130948 by Potter et al. (2002). The image is 20 s exposure in H band, taken with the Gemini North Telescope using the Hokupa'a AO and the QUIRC instrument.

---

[2]if not stated otherwise all uncertainties given in this work are always $1\,\sigma$ uncertainties
[3]age estimation based on the rotational period of the star, see Barnes (2003) and Barnes (2007)

II telescope and the NIRSPEC instrument (**N**ear-**I**nfra**R**ed echelle **SPEC**trograph, McLean et al. 1998), determining the spectral type to be dL2 with an uncertainty of two spectral subclasses.

More recently, Dupuy et al. (2009) presented observations of the BC system which enabled them to fit the apparent orbit of C around B and dynamically determine the mass of the BC system. They calculated a mass of 0.109 ± 0.003 M$_\odot$.

2.1.2   HD 203030

HD 203030 is a G 8 dwarf (Jaschek 1978) located at $\alpha = 21^h 18^m 58^s.219$ and $\delta = 26° 13' 49''.96$ (van Leeuwen 2007) in the constellation of Vulpus. The parallax of 24.46 ± 0.74 mas (corresponding to 40.9 pc) and proper motion of 132.84 ± 0.79 mas/yr in right ascension and 8.44 ± 0.65 mas/yr in declination, were measured by the Hipparcos satellite mission (van Leeuwen 2007). The mass of HD 203030 was determined independently in several studies and ranges from $0.93\,M_\odot$ to $1\,M_\odot$ (Allende Prieto and Lambert 1999, Metchev and Hillenbrand 2009, Casagrande et al. 2011). The age was first estimated by Montes et al. (2001), who claim a likely membership of HD 203030 in the young supercluster IC 2391 by kinematics. The age of IC 2391 members varies between 35 Myr and 55 Myr (Eggen 1991). This could not be confirmed by Metchev and Hillenbrand (2006), who did a detailed study of age indicators of the star. They find that chromospheric and coronal activity correspond to an age of 130 Myr to 400 Myr, consistent also with rotational period and Li abundance (Strassmeier et al. 2000). Additionally, they find that optical colors and luminosity place HD 203030 on the main sequence at an age range of 0.1 Gyr to 10 Gyr, i.e. in agreement with the higher age estimate.
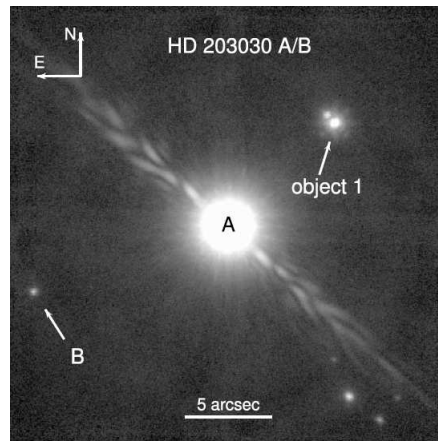
Figure 6: Discovery image of the companion to HD 203030 by Metchev and Hillenbrand (2006). The image was taken in K$_s$ band at the Palomar Observatory. HD 203030 A was placed behind a coronagraph. Object 1 is a background object. The bright structure ranging from the upper left to the lower right is introduced by an oil streak on the secondary telescope mirror.

The companion to HD 203030 was discovered by Metchev and Hillenbrand (2006), using the Hale 200 inch and KeckII 10 m telescope at the Palomar Observatory. The discovery image is shown in Fig. 6. The companion is located at a separation of ~ 11.9 arcsec (corresponding to ~ 487 AU) to the southeast (PA of $\sim 108.8°$) of the primary. Companionship of the object was confirmed by common proper motion with the primary in the same study. The infrared magnitudes of the companion were measured in the discovery study to be $m_J = 18.13 \pm 0.55$ mag, $m_H = 16.85 \pm 0.12$ mag and $m_{K_s} = 16.21 \pm 0.10$ mag. Using these and the models by Burrows et al. (1997), Chabrier et al. (2000) and Baraffe et al. (2003), a mass range of $0.012\,M_\odot$ to $0.031\,M_\odot$ is given, provided that the age range of the object is 130 Myr to 400 Myr. This places the companion with a high probability in the brown dwarf regime.

The spectral type of the companion was determined by near infrared spectroscopy in the K band to be L 7.5 ± 0.5 (Metchev and Hillenbrand 2006), i.e. close to the L/T transition[4]. The authors note that the companion exhibits an unsually low effective temperature given the late spectral type. They suggest that this could be an indication that the L/T transition extends to lower temperatures than previously expected.

2.1.3 DH Tau

DH Tau is a classical T Tauri star of spectral type M 1 (Watson et al. 2009) located at $\alpha = 04^h\,29^m\,41^s.558$ and $\delta = 26°\,32'\,58''.27$ (Cutri et al. 2003) in the constellation of Taurus. It is part of the Taurus Molecular Cloud (TMC), which had its spectroscopic distance determined by Kenyon et al. (1994) to be 140 ± 10 pc. It exhibits an average proper motion of 12 ± 4 mas/yr in right ascension and -25 ± 3 mas/yr in declination, as determined
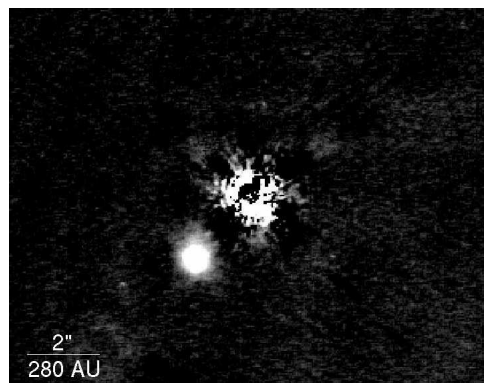
Figure 7: Discovery image of the companion to DH Tau by Itoh et al. (2005). The image was taken in K band with the CIAO instrument at the Subaru telescope. DH Tau A was placed behind a coronagraph and only B is visible. North is up and east is to the left.

---

[4]Spectral type L is characterized by red near infrared colors (J-K ~ 2, Kirkpatrick 2000) and very weak or absent TiO and VO lines (see e.g. Martin et al. 1997), as compared to M dwarfs. Spectral type T is much bluer (J-K ~ 0, Kirkpatrick 2000), due to strong methane absorption bands (Kirkpatrick 2000)

by Monet et al. (2003), Hanson et al. (2003) and Zacharias et al. (2004). DI Tau, another member of the TMC, is a wide stellar companion to DH Tau (Itoh et al. 2005), with a separation of 16 arcsec ($\sim$ 2240 AU). DI Tau by itself is a close (0.12 arcsec) binary (Chen et al. 1990). Mass and age of DH Tau and DI Tau have been estimated by Hartigan et al. (1994), using spectroscopy as well as optical and infrared photometry. Utilizing the models by D'Antona and Mazzitelli (1994) and Swenson et al. (1994), they derive a mass range for DH Tau of 0.24 M$_\odot$ to 0.32 M$_\odot$ and an age range of 0.1 Myr to 0.7 Myr. DI Tau is probably of the same age, but slightly more massive with a mass range between 0.28 M$_\odot$ and 0.40 M$_\odot$. A similar study has been conducted by White and Ghez (2001), who used the BCAH98 models by Baraffe et al. (1998). They estimate a higher mass for DH Tau of 0.53$_\odot$ and a much higher age of 4.4 Myr.

Furlan et al. (2006) conducted a photometric and spectroscopic survey in the wavelength range of 5 μm to 36 μm amongst members of the TMC using the Spitzer Space Telescope. They found that DH Tau exhibits an excess of luminosity in the mid infrared, typically associated with a transitional disk that lacks the warm inner dust which would otherwise produce an excess in the near-infrared as well. Gräfe et al. (2011) tried to resolve the inner structure of this disk, using VISIR (**V**LT **I**mager and **S**pectrometer for mid **I**nfrared, Lagage et al. 2004) on the Very Large Telescope (VLT) of the European Southern Observatory (ESO), but were not successful. They do, however, provide a limit for the inner disk radius of $< 15.5^{+9.0}_{-2.0}$ AU.

The Companion to DH Tau was discoverd by Itoh et al. (2005) using the CIAO instrument (**C**oronagraphic **I**mager with **A**daptive **O**ptics, Murakawa et al. 2004) on the Subaru Telescope. The discovery image is shown in Fig. 7. The companion is located 2.3 arcsec to the southeast of the primary at a PA of 139.8°. They confirm companionship by common proper motion using Hubble Space Telescope (HST) archival images from 1999, in which the companion is resolved as well. To estimate the mass of the companion, near-infrared spectra were taken with the OHS/CISCO instrument (**OH**-Airglow **S**uppressor/ **C**ooled **I**nfrared **S**pectrograph and **C**amera for **OH**S, Motohara et al. 2002), also on the Subaru Telescope. By comparison with model spectra by Tsuji et al. (2004), an effective temperature between 2700 K and 2800 K, and a surface gravity of $log\,g = 4.0$ to 4.5 are derived for the companion. Using these and the models by D'Antona and Mazzitelli (1997) and Baraffe et al. (2003), a mass range of 0.03 M$_\odot$ to 0.05 M$_\odot$ and an age range of 3 Myr up to 10 Myr are calculated. This places the companion in the brwon dwarf regime. The authors note that the calculated companion age seems to be older than the age of the primary, which they attribute to model imprecisions and an uncertain bolometric luminosity of the primary.
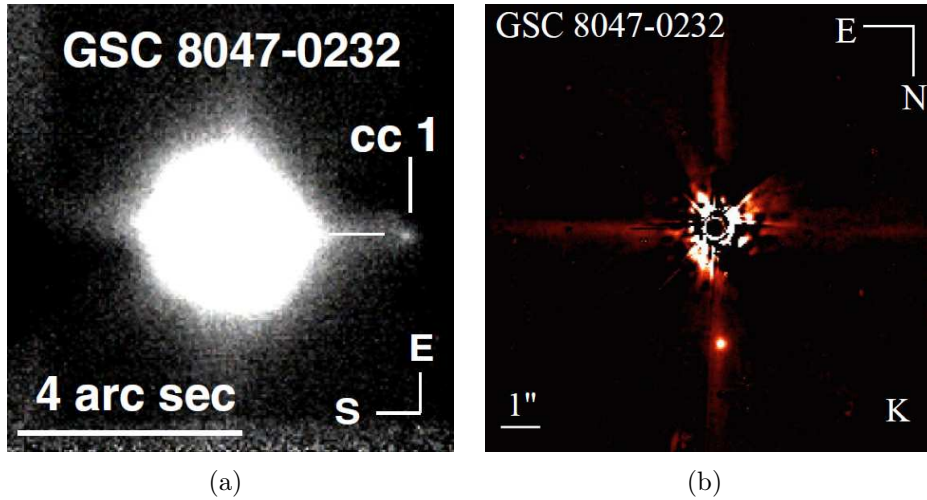
Figure 8: Discovery images of the substellar companion to GSC 08047-00232 by Neuhäuser et al. (2003) and Chauvin et al. (2003), in the left and the right panel respectively.

2.1.4   GSC 08047-00232

GSC 08047-00232 is a K 2 dwarf (Torres et al. 2006) located at $\alpha = 01^h\,52^m\,14^s.627$ and $\delta = -52°\,19'\,33''.06$ (Hog et al. 1998) in the constellation of Eridanus. Its proper motion was measured by Hog et al. (1998) to be $46.90 \pm 1.7\,\text{mas/yr}$ in right ascension and $-3.10 \pm 1.7\,\text{mas/yr}$ in declination.

GSC 08047-00232 was first identified to be a member of the 20 Myr - 30 Myr old Horologium Association (Torres et al. 2000) by its space motion and position in the color magnitude diagram. The parallax of GSC 08047-00232 was not measured directly, but Torres et al. (2000) inferred a distance of $\sim 89\,\text{pc}$ from kinematic considerations. In the same study, the mass of GSC 08047-00232 was estimated to lie between $0.7\,\text{M}_\odot$ and $1\,\text{M}_\odot$ by comparing optical photometry with models by Siess et al. (1997).

The Horologium Association was later combined with the Tucana Association (Zuckerman and Webb 2000), to the Tucana-Horologium (TucHor) Association (Zuckerman et al. 2001). TucHor has an average distance of $\sim 45\,\text{pc}$ (Zuckerman and Webb 2000) as determined by Hipparcos parallaxes. Strong $\text{H}\alpha$ emission as well as x-ray luminosity and Li lines lead to an age estimate of $\sim 40\,\text{Myr}$ by Zuckerman and Webb (2000). This was later refined by Stelzer and Neuhäuser (2000), who estimate an age as young as 10 Myr to 30 Myr, by comparing x-ray activity of TucHor members with other young associations of known age. The companion to GSC 08047-00232 was discovered independently by Neuhäuser et al. (2003) and Chauvin et al. (2003), using the speckle camera SHARP I (**S**ystem for **H**igh **A**ngular **R**esolution **P**ictures, Hofmann et al. 1992) on the 3.5 m ESO New Technology Telescope (NTT) and the ADONIS/SHARP II AO system (**AD**aptive **O**ptics **N**ear **I**nfrared **S**ystem, Beuzit et al. 1997) on the ESO 3.6 m telescope respectively. Both discovery images are shown in Fig. 8. The companion is located at a separation of $\sim 3.2\,\text{arcsec}$ to the north of the primary.

Chauvin et al. (2003) use available photometric data of the primary star to compare it with the BCAH98 models by Baraffe et al. (1998) and find the best fit at a photometric distance of $\sim 85\,$pc and a mass between $0.8\,M_\odot$ and $0.9\,M_\odot$. This puts the GSC 08047-00232 system farther away than average for TucHor members, but is in agreement with the first distance estimate by Torres et al. (2000). This distance was later also confirmed by Neuhäuser and Guenther (2004). Adopting this distance, Chauvin et al. (2003) estimate a mass range for the companion of $20\,M_{Jup}$ to $40\,M_{Jup}$, utilizing the DUSTY models by Chabrier et al. (2000) at a model age of $50\,$Myr. Similar mass estimates are made by Neuhäuser and Guenther (2004), who compare various models and find a most likely mass of $\sim 25\,M_{Jup}$. Later studies by Chauvin et al. (2005) and Chauvin et al. (2010) place the companion at masses of $25 \pm 10\,M_{Jup}$ and $20 \pm 5\,M_{Jup}$, using again the DUSTY models by Chabrier et al. (2000) and an age of $30\,$Myr.

The spectral type of the companion was first determined by Neuhäuser and Guenther (2004) using infrared spectroscopy. They estimated a spectral type of M 8 ± 2. Chauvin et al. (2005) obtained similar results and gave a spectral type of M 9.5 ± 1.

Chauvin et al. (2005) showed for the first time, that GSC 08047-00232 B is co-moving with A. Previously, companionship was concluded from photometry and spectroscopy only. They could reject the background hypothesis with $3.1\,\sigma$. This is also confirmed in Chauvin et al. (2010).

It was discussed more recently by Torres et al. (2008) that the GSC 08047-00232 system might be a member of the Columbia Association, rather than TucHor. Columbia shares a young age of $\sim 30\,$Myr but is slightly further away than TucHor. Both TucHor and Columbia are subgroups of the proposed GAYA (Great Austral Young Association, Torres et al. 2001) Complex.

2.1.5 1RXS J160929.1-210524

The K 7 dwarf (Lafrenière et al. 2008) 1RXS J160929.1-210524 is located at $\alpha = 16^h\,09^m\,30^s.31$ and $\delta = -21°\,04'\,58''.95$ (Zacharias et al. 2009) in the constellation of Scorpius. Its proper motion was determined by Zacharias et al. (2009) to be $-11.2 \pm 1.5\,$mas/yr in right ascension and $-21.9 \pm 1.5\,$mas/yr in declination. It is a member of the young Upper Scorpius OB Association (US, Preibisch and Zinnecker 1999), which is a part of the Scorpius-Centaurus Complex.

The mean distance of US was inferred by the measurement of Hipparcos parallaxes of member stars to be $145 \pm 2\,$pc (de Zeeuw et al. 1999), with an intrinsic scatter not larger than $20\,$pc (Preibisch et al. 2002). The age of US has recently become a matter of discussion. Originally it was determined in de Zeeuw and Brand (1985) and de Geus et al. (1989) to be ~ 5 - $6\,$Myr, by the H-R main-sequence turn-off point of high mass member stars. This was later confirmed in Preibisch and Zinnecker (1999) and Preibisch et al. (2002). There
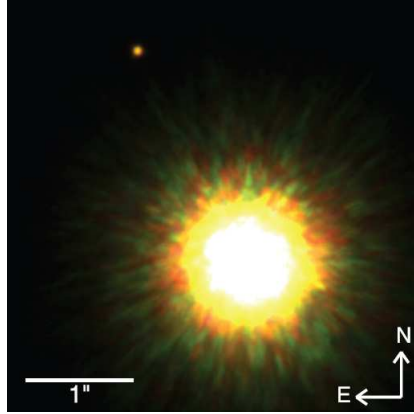
Figure 9: Discovery image of the companion to 1RXS J160929.1-210524 by Lafrenière et al. (2008). The image is a composite of J, H and K_s band observations, taken with the Gemini North Telescope and the NIRI instrument.

is, however, a recent paper by Pecaut et al. (2012), stating that they found US members of spectral type F to be underluminous by a factor of ~ 2.5, given the young age. They placed the various US members in H-R diagrams and therby determined a mean age of 11 ± 2 Myr.

Carpenter et al. (2009) used the Spitzer Space Telescope's MIPS instrument (**M**ultiband **I**maging **P**hotometer for **S**pitzer, Rieke et al. 2004) to search for infrared excesses in US, which would indicate debris disks around the concerning stars. They could not find any indication for such an excess around 1RXS J160929.1-210524 in $24\,\mu$m or $70\,\mu$m. It is therefore unlikely that 1RXS J160929.1-210524 harbors a debris or dust disk.

The substellar companion to 1RXS J160929.1-210524 was discoverd by Lafrenière et al. (2008), using the Gemini North Telescope with its AO system ALTAIR (**ALT**titude conjugate **A**daptive optics for the **I**nfra**R**ed, Richardson et al. 1998) and the NIRI instrument (**N**ear **i**nfrared **i**mager, Hodapp et al. 2003). The discovery image is shown in Fig. 9. The companion is located 2.22 arcsec north-east of the primary (~ 330 AU), at a PA of 27.7°. From near-infrared spectroscopy Lafrenière et al. (2008) inferred a spectral type of L4$^{+1}_{-2}$. Near-infrared magnitudes of the primary were taken from 2MASS (Two-Micron-All-Sky-Survey, Skrutskie et al. 2006) observations, and the companion's respective magnitudes were calculated from the contrast ratio to the primary star to be $m_J = 17.9 \pm 0.12$ mag, $m_H = 16.87 \pm 0.07$ mag and $m_K = 16.17 \pm 0.18$ mag. Given these magnitudes and using the age of 5 Myr for US and a distance of 145 ± 2 pc, Lafrenière et al. (2008) estimate a mass of the companion of $8^{+4}_{-2}\,M_{Jup}$, utilizing the DUSTY models by Chabrier et al. (2000). They are also using the 2MASS magnitudes of A, and the models of Baraffe et al. (1998) to estimate the mass of the primary to be $0.85\,^{+0.2}_{-0.1}\,M_\odot$. Since these mass limits for the companion are below the mass limit for deuterium burning of $\sim 13\,M_{Jup}$, Lafrenière et al. (2008) state that the companion should be a planetary mass object. Given the recent revision of the age for US, Pecaut et al. (2012) recalculated the mass, using the luminosities by Lafrenière et al. (2008) and the DUSTY models by Chabrier et al. (2000). They calculate

a mass of 14^{+2}_{-3} M$_{Jup}$, placing the companion just above the deuterium burning mass limit, and hence state that it seems more likely to be a brown dwarf, rather than a planetary mass object.

The common proper motion of the companion with the primary was more recently confirmed in Lafrenière et al. (2010) with a significance of $6\,\sigma$.

2.1.6 UScoCTIO 108

UScoCTIO 108 is a brown dwarf located at $\alpha = 16^h\,05^m\,53^s.94$ and $\delta = -18°\,18'\,42''.7$ in the constellation of Scorpius. It is a member of the Upper Scorpius Association (US), which was introduced in the previous section. It was discovered in the survey by Ardila et al. (2000) carried out at the Cerro Tololo Inter-American Observatory (CTIO). Ardila et al. (2000) give an I band magnitude of m$_I = 15.88 \pm 0.07$ mag and a R-I color of 2.19 ± 0.12 mag. The membership in US was determined by photometry and low resolution spectroscopy, and the mean distance of the association of 145 ± 2 pc (de Zeeuw et al. 1999) was adopted, as well as the age of the association of ~ 5 Myr as given in Preibisch and Zinnecker (1999) and Preibisch et al. (2002).

The companion to UScoCTIO 108 was discovered by Béjar et al. (2008), using 2MASS images. They then did follow-up observations using the Wilhelm Herschel Telescope and the Telescopio Nazionale Galileo. Additionally, they used the NIRSPEC instrument on the Keck II Telescope to obtain high resolution near-infrared spectra. The discovery image, as provided in Béjar et al. (2008), is shown in Fig. 10. The companion is located at a distance of 4.6 arcsec to the south of the primary, at a PA of 177°.

Béjar et al. (2008) fit the spectrum of UScoCTIO 108 and its companion by comparison with other young and field dwarfs. They give a spectral type of M 7 $\pm$ 0.5 for the primary and M 9.5 for the companion. In addition, they find H α and He I emission lines in the

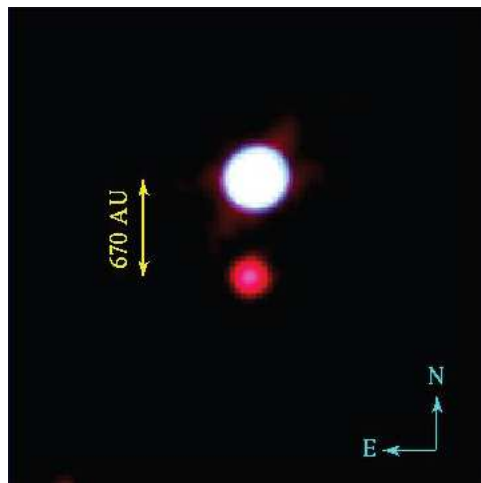Figure 10: Discovery image of the companion to UScoCTIO 108 by Béjar et al. (2008). The image is a composite of I, Z and K' band observations, taken with the William Herschel Telescope and the Telescopio Nazionale Galileo.

primary spectrum, which are an indicator for ongoing accretion from a disk and strong Li lines, which are an indicator for youth, consistent with the membership of both objects in the US. They also give infrared colors for both objects of J-K'$_A = 0.91 \pm 0.04$ mag and J-K'$_B = 0.91 \pm 0.04$ mag. Using their photometry and the COND models by Baraffe et al. (2003), as well as the distance and age of US as described, they estimate a mass of $60 \pm 20\,\mathrm{M}_{Jup}$ for the primary and $14^{+2}_{-8}\,\mathrm{M}_{Jup}$ for the companion, placing the companion just above the deuterium burning mass limit of $\sim 13\,\mathrm{M}_{Jup}$. Therefore, the companion is most likely a low mass brown dwarf. This mass estimate changes slightly if the revised age for US is used as given in Pecaut et al. (2012). They calculate a companion mass of $16^{+3}_{-2}\,\mathrm{M}_{Jup}$ using the DUSTY models by Chabrier et al. (2000), making it even more likely that UScoCTIO 108 B is indeed a brown dwarf, rather than a planetary mass object.

Béjar et al. (2008) perform no proper motion analysis to confirm companionship of UScoCTIO 108 B, but rather calculate the probability for another US member to be within 10 arcsec of UScoCTIO 108 as only 1.3 %, given the density of US. If indeed bound, UScoCTIO 108 A and B form the widest substellar binary known to date.

2.2 General Properties

To put this work in context, it is neccessary to compare the general properties of the target sample with the whole population of directly imaged substellar companions. There is no single up-to-date database available that contains information of all such companions. To obtain a comprehensive picture of the whole population, several sources were considered. For all companions discovered before August of 2009, the database available at *www.bdcompanions.org* by Bird and Metchev (2010) was consulted. This database is dedicated to brown dwarf and super-Jupiter like planetary mass objects discovered as companions to stellar primaries, and was last updated on 2009 August 13. For directly imaged planetary mass objects discovered since August 2009, the database at *www.exoplanet.eu* by Schneider et al. (2011) was utilized. The resulting list of objects was cross-referenced with all available publications of late 2009 till early 2012, which added three more brown dwarf companions discovered by Thalmann et al. (2009), Scholz (2010), Mugrauer et al. (2010) and Biller et al. (2010).

The distribution of directly imaged substellar companions on the sky is shown in Fig. 11. A few "clumps" can be observed in some regions of the sky, which represent very well observed young associations of stars such as the Taurus star-forming region or the Upper-Scorpius association. Our target stars (marked in red) spread over a range of declinations from +30° to -60°, which roughly corresponds to the range of declinations at which one can observe targets at a reasonalbe altitude with the ESO VLT, the main instrument that was utilized to gather further astrometric data points.

In Fig. 12, projected separation versus discovery epoch and distance are shown for the
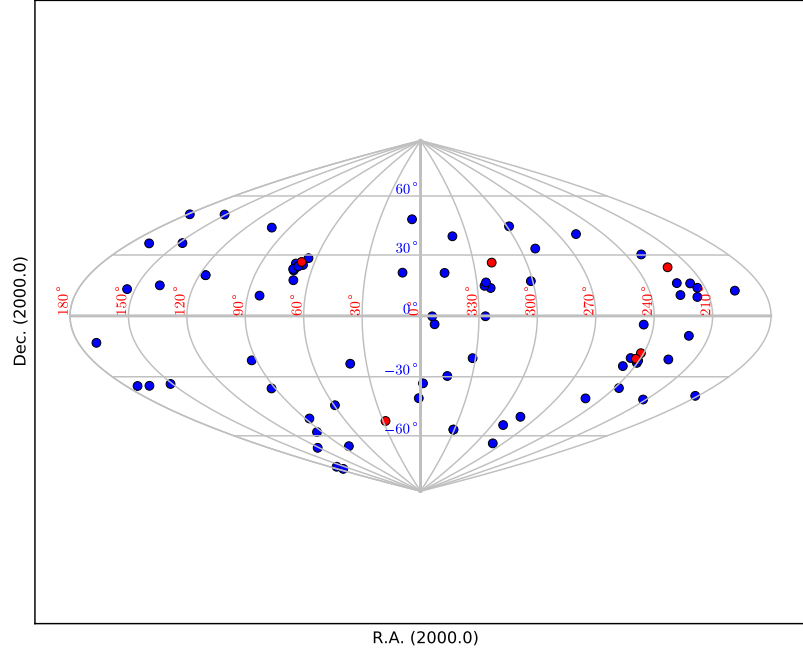
Figure 11: Distribution of directly imaged substellar companions on the sky. Stars discussed in this study have been marked red.

whole companion population and the target sample. Most objects were discovered after 1998, giving a maximum time baseline of 14 years to date. The targets of this study were discovered between 2001 and 2008, giving shorter baselines. The range of separations for all companions discovered so far reaches from just inside 0.1 arcsec to close to 1000 arcsec, with the majority lying under 10 arcsec. If we only consider companions with separation < 100 arcsec, since they are far more likely to exhibit a measureable orbital motion, the average separation of this sub-group is 8 arcsec. The average separation of the target sample is 4.5 arcsec, i.e. slightly smaller than the average of the aforementioned sub-group, but ranges from ~ 12 arcsec to ~ 2.2 arcsec.

The distance distribution of the whole population in Fig. 12(b) can be roughly divided into two subgroups of systems closer than ~ 60 pc and systems further away than ~ 110 pc. The target sample is equaly divided between these two groups.

In Fig. 13 the mass of the detected companions is plotted versus the projected separation. If we assume that the projected separation equals the semi-major axis a of the orbit of the given object, then according to:

$$P = 2\pi \sqrt{\frac{a^3}{G \cdot (M_* + M_{comp})}}$$

(wherein $G = 6.67384(80) \cdot 10^{-11} \, m^3 kg^{-1} s^{-2}$ is the gravitational constant and M_* is the mass of the primary star), the period P of the orbit would be smaller for smaller projected

(a)   (b)
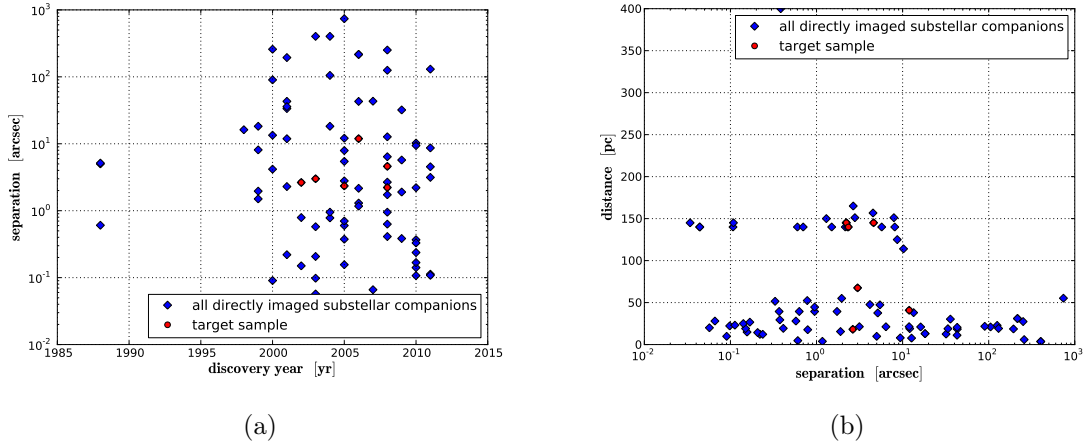
Figure 12: Separation versus discovery year, and distance versus separation, for all directly imaged substellar companions. Targets discussed in this study are marked red. Separation is displayed on a log-scale.

separations and larger companion masses M_{comp}. It is, however, unlikely that a significant number of systems are oriented so that we could actually observe the semi-major axis as projected separation. The average projected separation of the whole population is 1072 AU and ranges from ~ 1 AU to ~ 41000 AU, while the average projected distance for the target sample of this work lies at 352 AU and ranges from 48 AU to 667 AU. The average mass of the population is 40 M_{Jup} with a range from $\sim 3 M_{Jup}$ to $\sim 94 M_{Jup}$. The target companions are on average less massive with 28 M_{Jup} and cover a range from $\sim 8 M_{Jup}$ (first mass estimate of 1RXS J160929.1-210524 b) to $\sim 58 M_{Jup}$ (mass estimate of HD 130948 B).

In Fig. 14, the age distribution of all directly imaged substellar companions is shown. In cases where age ranges were given, the median age has been adopted. The general age range of the population lies between 1 Myr and 10 Gyr, with the average being 1.3 Gyr. The stars of the target sample are between 1 Myr and 0.8 Gyr old, i.e. younger than the average.

In conclusion, the target sample consists of 6 stars and their substellar companions, which are distributed on the sky so that they can be observed with the ESO VLT at a reasonable altitude. The companions are on average at smaller projected separations than the whole population of such companions detected so far, and should therefore have a slightly higher chance to exhibit orbital motion. Because all target companions are young, less massive bodies (if present), which may also influence the orbit, should have been detected in the deep VLT/NaCo images which were taken (detection limits are discussed in section 5.3). The time baseline ranges from two to seven years and is shorter than the maximum time baseline which could be achieved for some objects not discussed in this work. Thus, if orbital motion is detected for the given target sample, it is possible that there are more objects which exhibit measureable orbital motion.
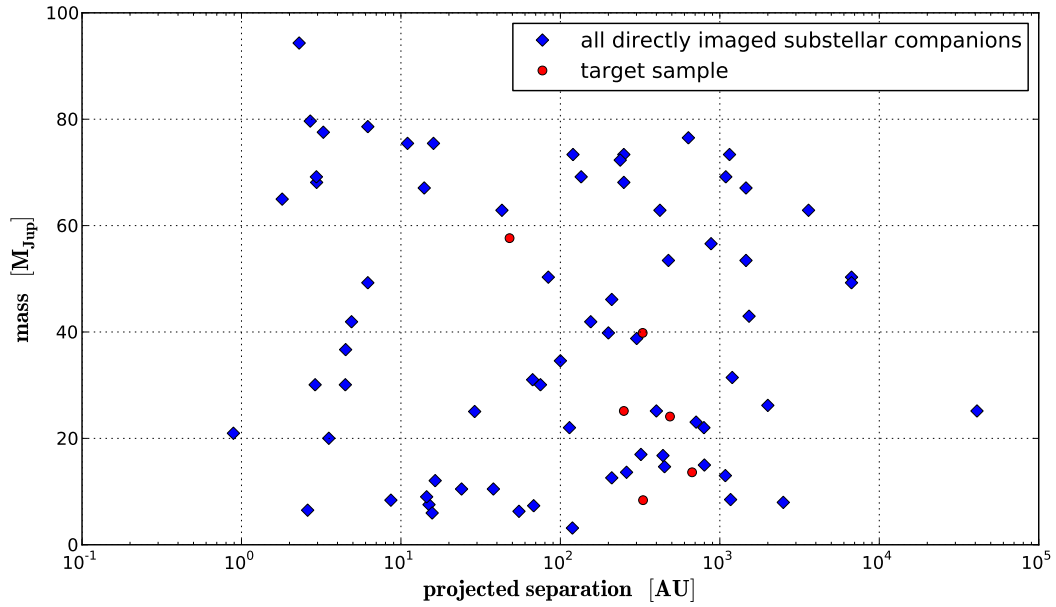
Figure 13: Mass versus projected separation for all directly imaged substellar companions. Stars discussed in this study have been marked red. Masses are in all cases the mean values from the given ranges. Separation is displayed on a log-scale.
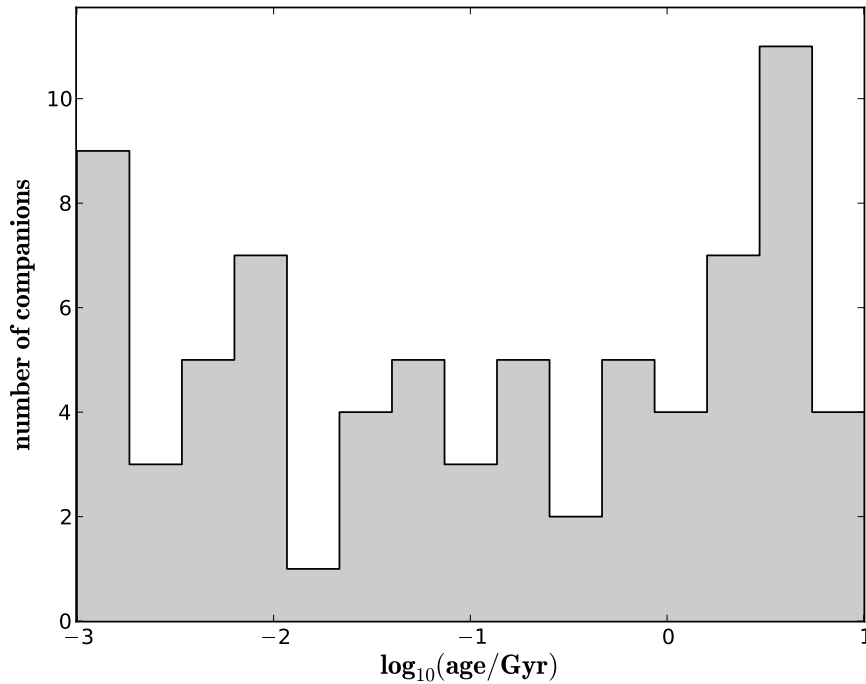
Figure 14: Age distribution of all directly imaged substellar companions. For display reasons, the decadic logarithm of the age in Gyr is shown. In cases where age ranges were given, the median age was adopted.

Table 1: Summary of target properties. The references for the listed values are given in sections 2.1.1 to 2.1.6. In cases were there are several possible values for a parameter given in the literature, a range is given in the table.

	HD 130948	HD 203030	GSC 08047	DH Tau	1RXS J1609	UScoCTIO 108
The Primary						
R.A.	$14^h\,50^m\,15^s.81$	$21^h\,18^m\,58^s.22$	$01^h\,52^m\,14^s.63$	$04^h\,29^m\,41^s.56$	$16^h\,09^m\,30^s.307$	$16^h\,05^m\,53^s.94$
Dec	$23°\,54'\,42''.6$	$26°\,13'\,49''.96$	$-52°\,19'\,33''.06$	$26°\,32'\,58''.27$	$-21°\,04'\,58''.95$	$-18°\,18'\,42''.7$
Spectral Type	G 1 V	G 8 V	K 2 V	M 1	K 7 V	M 7 ± 0.5
Mass [M$_\odot$]	1	0.93 - 1	0.7 - 1	0.24 - 0.53	$0.85\,^{+0.2}_{-0.1}$	0.057 ± 0.019
Age [Myr]	790^{+220}_{-150}	130 - 400	10 - 40	0.1 - 4.4	5 - 13	5 - 13
Distance [pc]	18.17 ± 0.11	40.9 ± 1.2	45 - 85	140 ± 10	145 ± 20	145 ± 20
Proper Motion R.A. [mas/yr]	143.91 ± 0.37	132.84 ± 0.79	46.90 ± 1.7	12 ± 4	−11.2 ± 1.5	-8 ± 14
Proper Motion Dec [mas/yr]	32.69 ± 0.34	8.44 ± 0.65	-3.10 ± 1.7	-25 ± 3	−21.9 ± 1.5	-17 ± 13
The Companion						
Discovery Year	2001	2002	2001	2002	2008	2007
Separation [arcsec]	2.64 ± 0.01	11.923 ± 0.021	3.210 ± 0.118	2.340 ± 0.006	2.219 ± 0.032	4.6 ± 0.1
Proj. Separation [AU]	48 ± 2	487 ± 1	273 ± 10	328 ± 1	330 ± 5	667 ± 14
Position Angle [°]	104.5 ± 0.5	108.76 ± 0.12	359.2 ± 2.3	139.56 ± 0.17	27.7 ± 0.6	177 ± 1
Spectral Type	$dL2 \pm 2$ / $dL2 \pm 2$	L 7.5 ± 0.5	M 9.5 ±1	-	L4$^{+1}_{-2}$	M 9.5
Mass Estimate [M$_\odot$]	<0.075 / <0.065	0.012 - 0.031	0.019 - 0.038	0.03 - 0.05	0.006 - 0.015	$0.013^{+0.002}_{-0.008}$

3 Data Aquisition and Reduction

This study utilizes data taken at the Calar Alto and ESO Paranal observation sites, as well as data obtained from various public science archives. In section 3.1 the instruments used for data aquisition are briefly characterized. In sections 3.2 and 3.3 the observation and archive data as well as the reduction strategies are described.

3.1 Telescopes and Instruments

3.1.1 NAOS-CONICA at the ESO Very Large Telescope

The **N**asmyth **A**daptive **O**ptics **S**ystem (NAOS) and the **CO**udé **N**ear **I**nfrared **CA**mera (CONICA) are mounted on the Nasmyth focus of Unit Telescope 4 (UT 4) "Yepun". UT 4 is one of the four 8.2 m telescopes of the ESO at the Cerro Paranal observation site in the Chilenean Attacama desert.

NAOS is equipped with two Shack-Hartmann wavefront sensors[5] for visual and near-infrared light, to measure and correct for wavefront distortions due to the turbulent atmosphere. Wavefront corrections are applied via a tip-tilt mirror and a deformable mirror. Dichroic filters are used to split the light from the telescope between the NAOS AO system and the CONICA detector. A measure for the accuracy of the applied wavefront corrections is the Strehl ratio. The Strehl ratio is the percentage of total flux from a source that is concentrated in its PSF core. Provided a sufficently bright ($V \leq 10$ mag) reference star close to the science target (< 30 arcsec), and good seeing conditions (≤ 0.8 arcsec), NAOS can provide Strehl ratios close to 50 % in the K band (Girard 2012).

CONICA is a high resolution infrared camera and spectrometer. It is outfitted with an InSb Aladdin 3 array of 1026×1024 pixels, sensitive in a wavelength range of $0.8\,\mu$m to $5.5\,\mu$m. The optical path of the instrument includes several wheels containing, among other things, narrow and broad band filters, polarizers, grisms and various camera objectives. In this study, the K_s broad band filter and the $2.17\,\mu$m narrow band filter are utilized alongside the S 13 and S 27 camera objectives. With the S 13 camera objective, CONICA has a pixel scale of ~ 13.22 mas/pixel and a field of view of approximately 14×14 arcsec, while, with the S 27 objective, it has a pixel scale of ~ 27.05 mas/pixel and a field of view of 28×28 arcsec. Several detector readout modes and associated instrument settings are available for observations. All data in this study was taken with the detector set to *HighDynamic* mode, which is a compromise setting with an intermediate full well depth of 15000 ADU and a high gain of $11.0\,e^-$/ADU, best suited to detect faint sources close to the bright target stars. The readout sequence was set to *Double RdRstRd*, meaning that the array is first read, then reset and read again. The minimum detector integration time for a single exposure (DIT)

---

[5]A Shack-Hartmann wavefront sensor consists of an array of lenses that are each focused on a CCD array. By measuring the focus position of each lens, local tilts of the wavefront can be determined.

in this mode is 0.3454 s.

The NAOS AO system is exclusively operating with the CONICA camera, and the setup is therefore usually referred to as NaCo. A detailed description of the instruments can be found in Girard (2012). The on-sky performance is also discussed in Rousset et al. (2003) and Lenzen et al. (2003).

3.1.2   ALFA and Ω-CASS at the Calar Alto 3.5 m Telescope

The **A**daptive optics with a **L**aser **F**or **A**stronomy system (ALFA) was installed on the Calar Alto 3.5 m telescope alongside the infrared multimode imager and spectrometer for the Cassegrain focus Ω-CASS. Both instruments are meanwhile decommissioned. The Calar Alto telescopes of the German-Spanish Astronomical Centre are located at the Sierra de Los Filabres in the province of Almeria, Spain.

ALFA was equipped with one Shack-Hartmann sensor to measure the wavefront distortion in the visual light. The distortion was then corrected by a tip tilt mirror and a deformable mirror. ALFA could use a natural guide star as reference object or a built-in laser guide star, which produced an artifical reference star in the mesospheric sodium layer. For all observations discussed in this study, a natural guide star was used. Given a bright natural guide star ($V \sim 7$ mag) and good seeing conditions of 0.9 arcsec to 1.2 arcsec, ALFA could achieve Strehl ratios of $\sim 40\,\%$ (Davies et al. 1999).

Ω-CASS consisted of a Rockwell 1024×1024 pixel HgCdTe HAWAII array, sensitive in a wavelength range from 1.0 μm to 2.5 μm, as well as several near-infrared broad- and narrow-band filters, polarizers and grisms. The camera optics could be adjusted for low and high resolution imaging with or without AO support by ALFA. All observations relevant in this study have been obtained in the H-band, in high resolution mode with a pixel scale of ~ 0.04 mas/pixel and a field of view of approximately 41×41 arcsec.

Several detector readout modes were available, of which the double correlated readout mode was utilized for all observations. The minimum detector integration time in this readout mode is 0.842 s.

A detailed description of the ALFA system is given in Kasper et al. (2000), while Lenzen et al. (1998) give an overview on Ω-CASS.

3.2   Observation Data

All targets discussed in this study were observed with VLT/NaCo between July and October of 2009 in service mode as part of program 083.C-0283(A). In addition, the HD 130948 system was observed as part of other observing programs on 2002 April 26 and 2006 April 15 with the Calar Alto 3.5 m telescope. An overview of all observations is given in Tab. 2.

Table 2: Observation epochs

Date	Telescope	Filter	DIT [s]	NDIT	NExp	Target Observed
2002-04-26	Caha 3.5 m	H	0.842	49	24	HD 130948
2006-04-15	Caha 3.5 m	H	0.842	49	28	HD 130948
2009-07-03	VLT	NB 2.17	0.4	149	21	HD 130948
2009-08-15	VLT	K_s	1	60	23	1RXS J160929.1-210524
2009-08-16	VLT	K_s	60	1	31	UScoCTIO 108
2009-08-20	VLT	NB 2.17	0.5	120	23	HD 203030
2009-09-13	VLT	K_s	0.6	100	44	GSC 08047-00232
2009-10-01	VLT	K_s	1	60	22	DH Tau

VLT/NaCo observations

In the case of the VLT/NaCo observations, the single exposure times (DIT) were adjusted for each target to not saturate the primary stars, in order to enable high precision astrometry. The bright primary stars were used as reference sources for AO corrections. Observations were done in the K-band, since substellar companions are brightest in this wavelength range. In the cases of HD 130948 and HD 203030, the minimum detector integration time of 0.3454 s would have been too long in broad band filters to not saturate the primaries, hence in these two cases the narrow band filter with a central wavelength of 2.17 μm (located in the K-band) was utilized.

For all observations the jitter technique was applied to sample the bright infrared sky background. Thereby, a number (NDIT) of several short exposures (DIT integration time) is taken at one position of the detector, then the primary is moved by a few arcsec to a different position on the detector. The process is repeated a number (NExp) of times. In all but one case the S 13 objective of NaCo was used, since the companions are within a few arcsec of the primary stars. In the case of HD 203030, however, the companion is separated from the primary by ~ 11.9 arcsec. Since NaCo has only a field of view of 14×14 arcsec with the S 13 objective, it would not have been possible to dither the star position on the detector in the described fashion. Thus, for the observations of the HD 203030 system, the S 27 objective was utilized.

In addition to the science exposures, sky flats were taken at the beginning and end of each observation night, as well as images of wide binary stars which were used for astrometric calibration (for a detailed discussion of this topic see section 4).

For reduction of the data, the ESO ECLIPSE software package (Devillard 2001) was used, and most specifically the *jitter* routine included therein. First each image is flatfielded, then the difference of subsequent images is computed to subtract the sky background. The resulting images are then automatically shifted and added up. The results for each of the target stars are shown in Fig. 15.

After basic image reduction, the PSF of the primary star was subtracted in all cases using

simulated roll subtraction. Thereby, the image is rotated by 360° in steps of small angular increments. The difference between the rotated image and the original image is computed for each step and all difference-images are averaged to produce the final PSF subtracted image. This technique eliminates all radial symmetric parts of the primary stars' PSF. For all images an angular increment of 2° was applied. The results are shown as well in Fig. 15.

Calar Alto observations

The observations of the HD 130948 system at the Calar Alto 3.5 m telescope were carried out with ALFA/Ω-CASS in the H band. The primary star was used as reference source for AO corrections. The jitter technique was employed again to sample the sky background. The shortest possible detector integration time of 0.842 s was choosen for each individual exposure. In 2002 the short exposures add up to a total integration time of 16.5 min, and in 2006 to a total integration time of 19.3 min. In both epochs the primary stars' PSF core was saturated. Saturation is more prominent in the 2002 epoch due to better observing conditions and AO correction, and hence a better Strehl ratio of the resulting images. Sky flats and astrometric calibration binaries were imaged in both observing epochs.
The data reduction and PSF subtraction were performed analogus to the VLT/NaCo data. The binary companion is clearly detected in the PSF-subtracted images shown in Fig. 15(a) and Fig. 15(b).
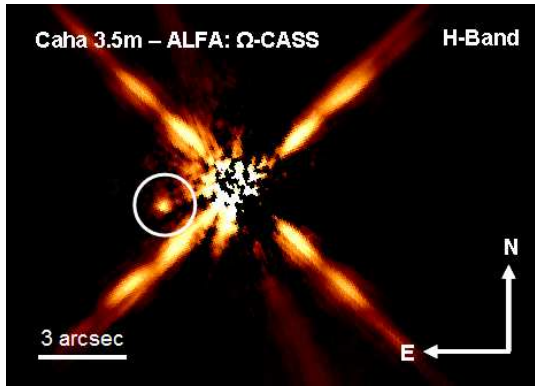
(a) HD 130948 at 2002-04-26 PSF-subtracted
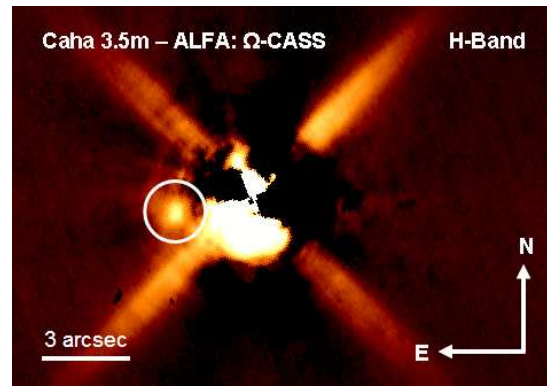
(b) HD 130948 at 2006-04-15 PSF-subtracted
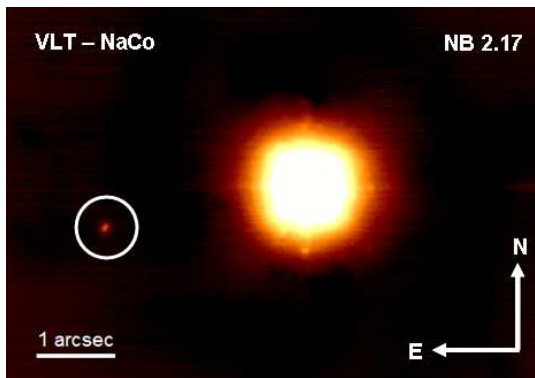
(c) HD 130948 at 2009-07-03
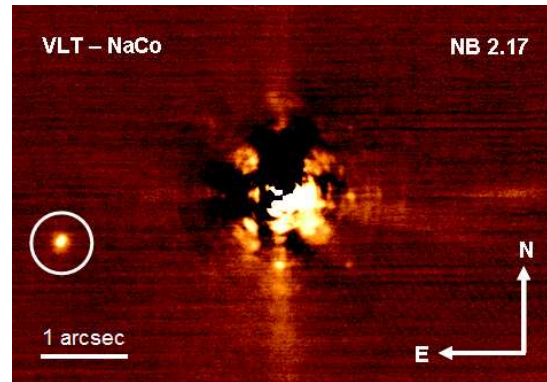
(d) HD 130948 at 2009-07-03 PSF-subtracted
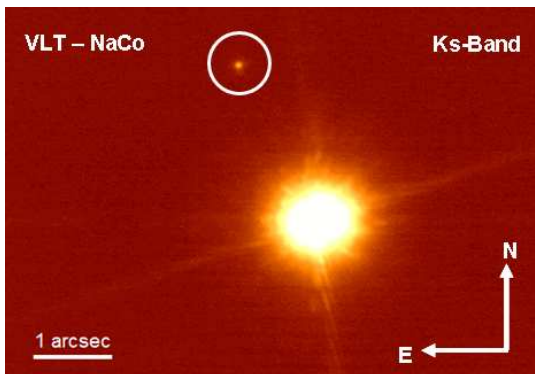
(e) 1RXS J160929.1-210524 at 2009-08-15
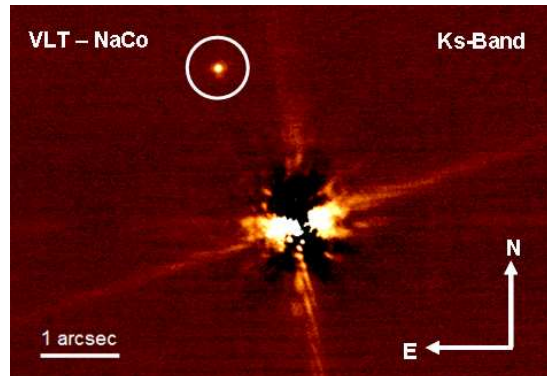
(f) 1RXS J160929.1-210524 at 2009-08-15 PSF-subtracted
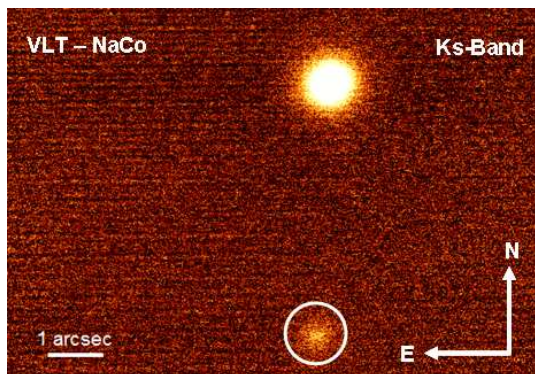
(g) UScoCTIO 108 at 2009-08-16
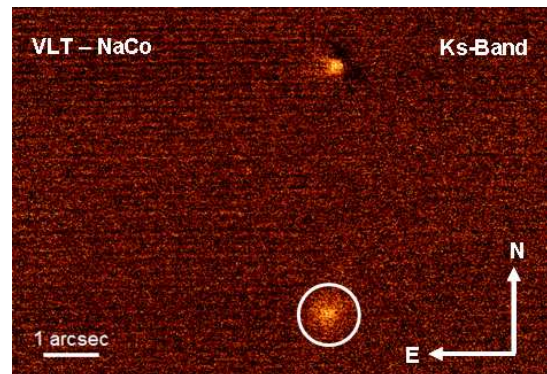
(h) UScoCTIO 108 at 2009-08-16 PSF-subtracted
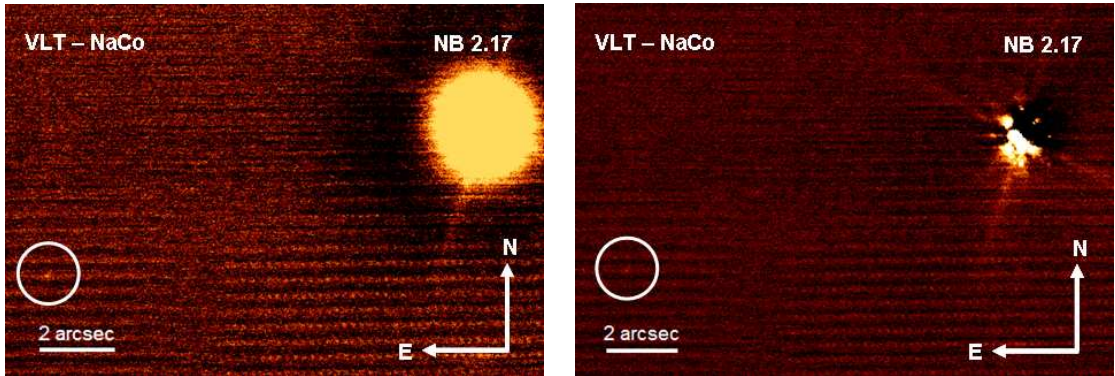
(i) HD 203030 at 2009-08-20

(j) HD 203030 at 2009-08-20 PSF-subtracted
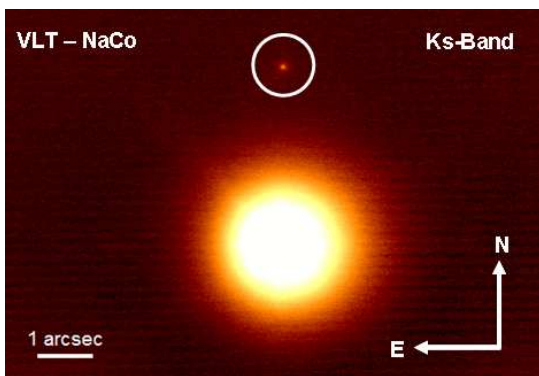
(k) GSC 08047-00232 at 2009-09-13
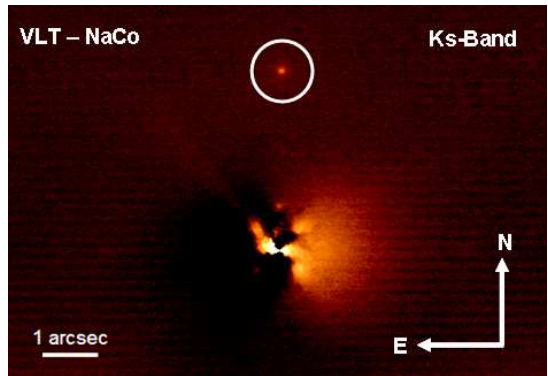
(l) GSC 08047-00232 at 2009-09-13 PSF-subtracted
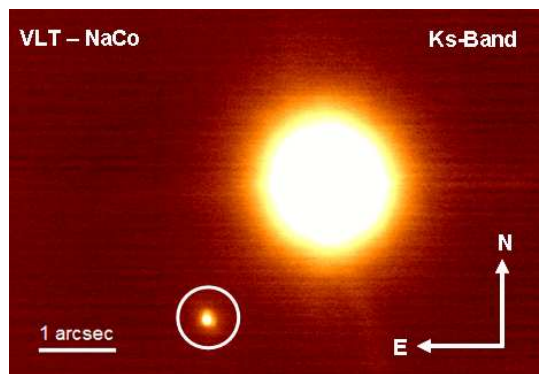
(m) DH Tau at 2009-10-01
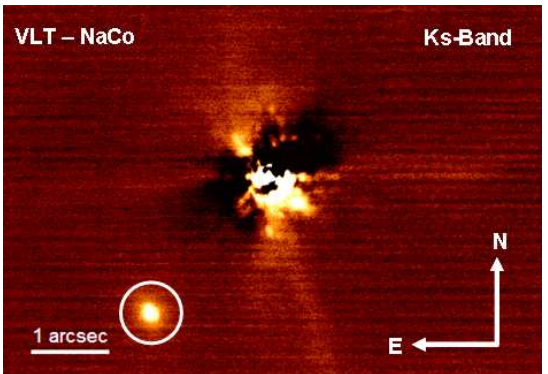
(n) DH Tau at 2009-10-01 PSF-subtracted

Figure 15: Final reduced VLT/NaCo and Calar Alto images of the target stars. The first two Calar Alto images are PSF subtracted to make the companions visible. In all other cases the panels on the left show the reduced NaCo images and the panels on the right the respective PSF subtracted images. PSF subtraction was always done by simulated roll subtraction.

3.3 Archive Data

For all targets discussed in this work, the Hubble Space Telescope science archive, the ESO science archive, the SMOKA science archive, and the Gemini science archive were checked for additional unpublished high-resolution imaging observations. In the case of HD 130948, several such observations were found and subsequently used to gather additional astrometric data points. No other publicly available unpublished observations were found for the rest of the target sample. An overview of all utilized archival observation epochs of the HD 130948 system is given in Tab. 3.

Table 3: Archive epochs of HD 130948

Date	Telescope	Instrument	Filter	exposure time [s]
2001-06-28	Gemini-North	Hokupaa+QuIRC	H	6×0.5
2002-04-23	Gemini-North	Hokupaa+QuIRC	H	16×5
2002-09-06	HST	ACS	F850LP	200
2003-05-21	Subaru	IRCS	H	$19 \times 4 \times 5$
2005-02-23	HST	ACS	F850LP	300
2005-04-17	Gemini-North	NIRI	CH4(short)	$90 \times 1 \times 30$

Gemini-North Telescope

HD 130948 was observed with the Gemini North telescope several times. The first observations were executed with the Hokupa'a natural guide star adaptive optics system, which has been replaced by the Altair system in 2003, and its near infrared camera QuIRC, which has also since been decommissioned. HD 130948 was observed with this instrument setup on six different occasions between 2001 February 24 and 2002 April 23. Of these, only the observing epochs on 2001 June 28 and 2002 April 23 are included in this study, since the images in all other observing epochs were taken with a Wollaston prism in place, resulting in a split field of view with different image polarisations. The Wollaston prism might introduce additional geometric distortions which would affect the astrometry and hence such observing epochs are excluded.

In the 2001 epoch, six images with an individual effective integration time of 0.5 s were taken, and in 2002, sixteen images with an individual effective integration time of 5 s were taken. The PSF core of the primary is in all cases saturated. The binary companion is clearly detected in all single exposures. All images were flat field corrected. Additionally, the flat field images were used to create a bad pixel map to correct for hot and cold pixels. The values of all identified bad pixels were replaced by the median of the adjacent pixels. The resulting images are shown in Fig. 16(a) and Fig. 16(c) respectively. The PSF of the primary was subtracted from each image by applying a gaussian filter and then subtracting

the resulting image from the original. The results are shown in Fig. 16(b) and Fig. 16(d) respectively.

There were additional observations of the HD 130948 system available in the Gemini science archive on 2005 April 17. They were carried out with the NIRI detector and the Altair adaptive optics system. Ninety images with an individual exposure time of 30 s were taken in an angular differential imaging (ADI, Marois et al. 2006) sequence. This means that the instrument rotator is turned off and the field of view is slowly rotating as the the telescope tracks the target on the sky. In all single exposures the binary companion is clearly detected, while the primary star is highly saturated. To subtract the primary star's PSF, all slightly rotated images were averaged to reconstruct a model PSF. The averaged PSF was then subtracted from all single exposures. The corresponding images are shown in Fig. 16(k) and Fig. 16(l).

Hubble Space Telescope

HD 130948 was observed with the Hubble Space Telescope's (HST) ACS (Advanced Camera for Survey, Clampin et al. 2000) instrument in high resolution mode on 2002 September 6 and on 2005 February 23. Both epochs are public and can be accessed in the HST science archive. A variety of wide-, medium- and narrow-band filters in the visual wavelength range were used in both epochs, but only in the images taken with the F850LP (roughly corresponding to I-band, Ubeda 2011) filter are the BC companions detected with high signal-to-noise. Exposure times of 200 s and 300 s were used in the 2002 and 2005 epochs respectively.

The ACS data was used as provided by the HST science archive reduction pipeline. All images are flatfielded and dark subtracted, as well as corrected for geometrical distortion by the MultiDrizzle pipeline (Koekemoer et al. 2002).

The primary was always occulted by an 1.8 arcsec coronagraphic spot. Since the coronagraph of the ACS is inserted into the aberrated beam, there is still some light from the primary's PSF core reaching the detector. This results in a fainter and slightly distorted version of the star's PSF appearing at the position of the primary behind the occulting spot on the detector, as well as bright diffraction rings. To remove this residual light of the primary, an image with slightly different orientation taken in the 2005 epoch was used to perform a roll subtraction on the 2005 data. For the 2002 data such a rolled image was not available. It was, however, possible to subtract the 2005 image from the 2002 image, since both were taken with the same instrument settings and therefore show similar diffraction patterns.

Subaru Telescope

The HD 130948 system was observed with the Subaru telescope and its IRCS (Kobayashi et al. 2000) instrument on 2003 May 21 in the H-band. IRCS was in high resolution imaging mode with an approximate pixel scale of 23 mas/pixel. The AO36 adaptive optics system (the predecessor of the current AO188 system, Takami et al. 2004) was utilized, with HD 130948 as guide star. The data is publicly avaiable in the SMOKA science archive. The jitter technique was used to sample the infrared sky background. Due to the long exposure times, the core of the bright primary's PSF is saturated in all images.

ESO-ECLIPSE software was used to flatfield, background-subtract and co-add all images. The final co-added image has an effective integration time of 6.3 min and can be seen in Fig. 16(g).

To subtract the primary's PSF, a simulated roll subtraction was performed as explained in the previous section. The quality of the subtraction result depends strongly on the position of the center of radial symmetry of the primary star. To improve the result, a Monte Carlo simulation was performed, drawing random positions from a normal distribution centered on the photocenter of the saturated primary with a full width at half maximum of three pixels. For each position, a simulated roll subtraction with angular increments of two degrees was performed and the residual noise in the PSF core was measured after subtraction. The resulting image with minimal residual noise after 1000 runs is shown in Fig. 16(h).
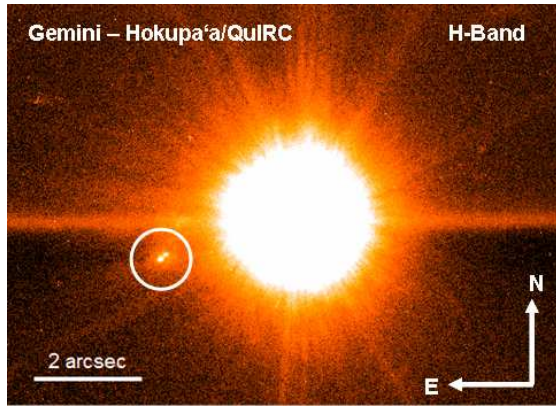
(a) 2001-06-28
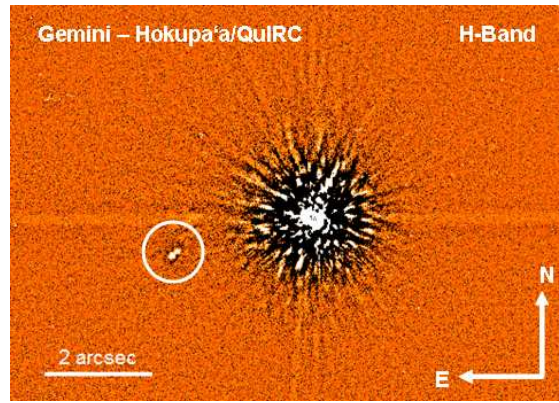
(b) 2001-06-28 PSF-subtracted
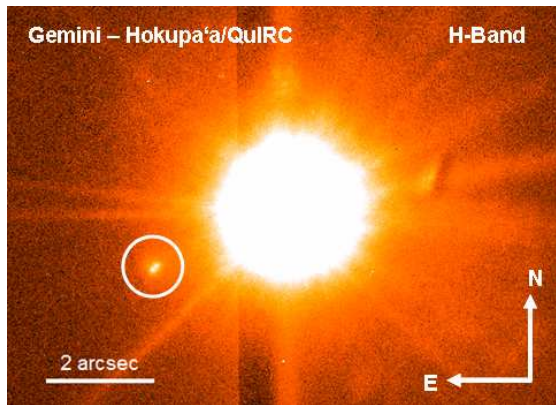
(c) 2002-04-23
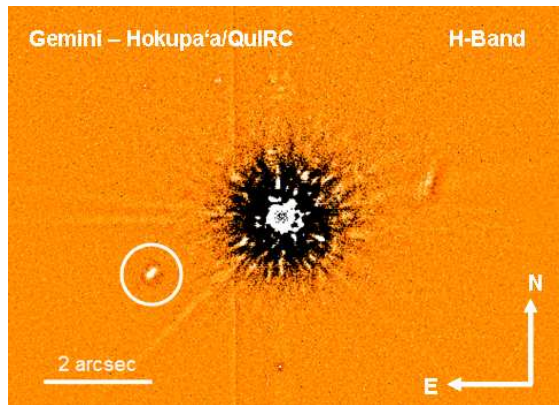
(d) 2002-04-23 PSF-subtracted
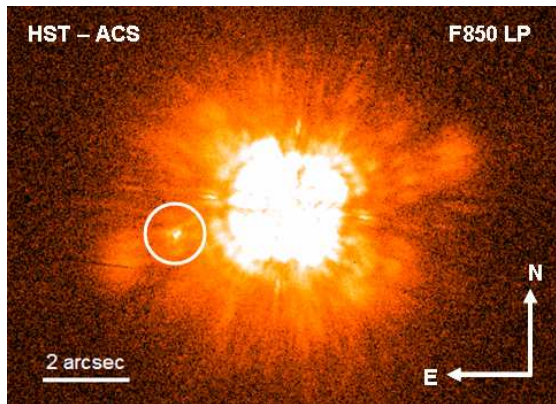
(e) 2002-09-06
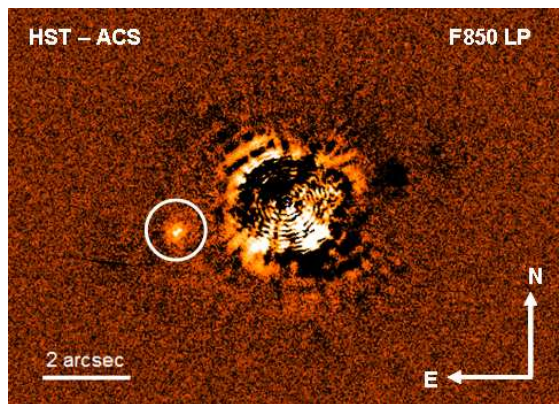
(f) 2002-09-06 PSF-subtracted
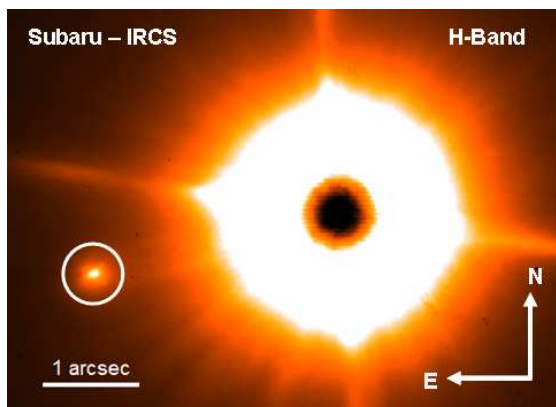
(g) 2003-05-21
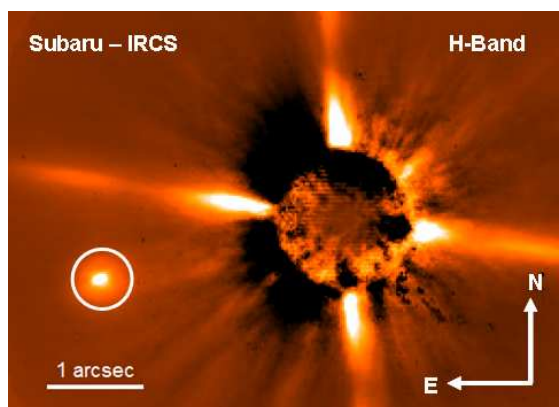
(h) 2003-05-21 PSF-subtracted

(i) 2005-02-23

(j) 2005-02-23 PSF-subtracted

(k) 2005-04-17

(l) 2005-04-17 PSF-subtracted
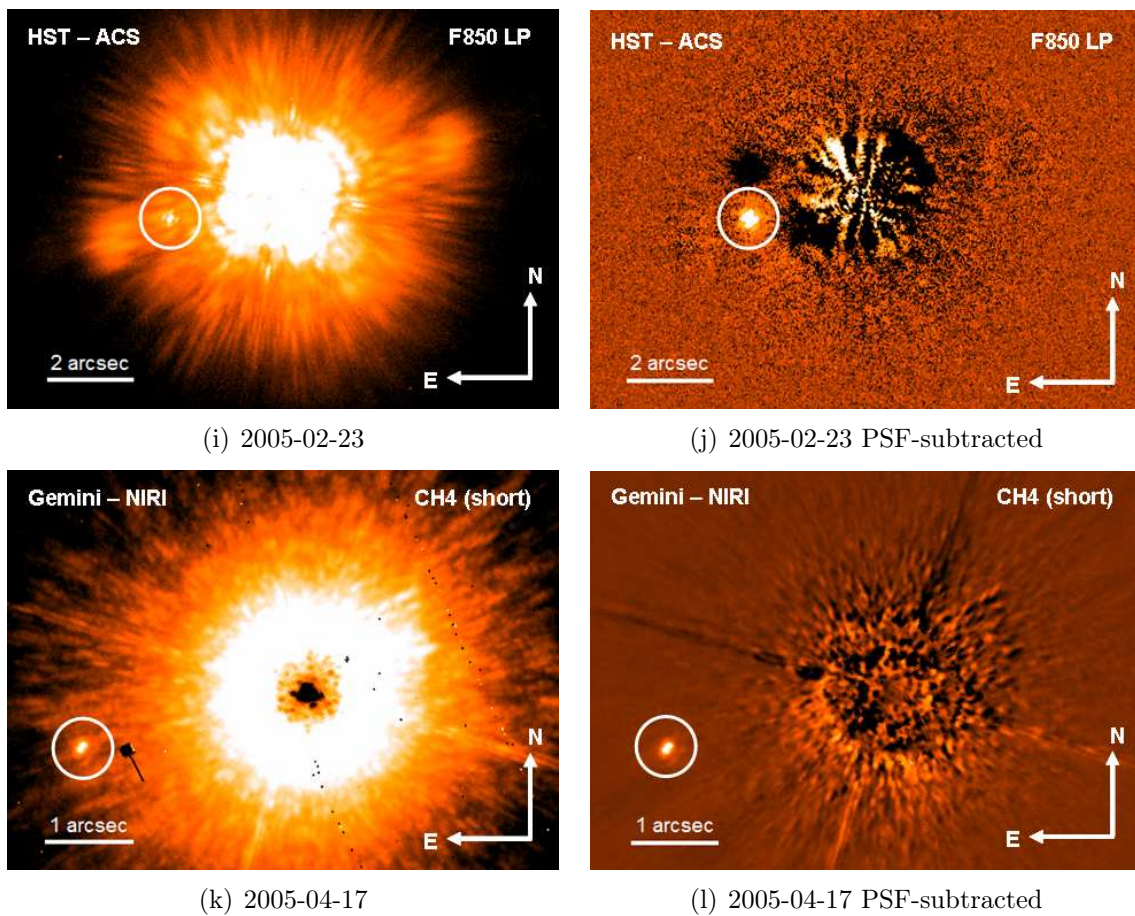
Figure 16: Final reduced archive images of HD 130948. In the left panels the reduced images are shown and in the right panels the PSF subtracted images are shown.

4 Astrometric Calibration and Measurements

4.1 VLT/NaCo Data

Calibration

For astrometric calibration of the VLT/NaCo data, one of the two wide binaries HIP 73357 and HIP 6445 was imaged in every observing night, using the same instrument settings and observing technique as the science targets. Since the science targets were observed as part of a larger observing program, there are additional observing nights available for both binaries. An astrometric calibration was done for all these nights to check for consistency of the overall calibration results, and to monitor possible short term variations of pixel scale and orientation of the detector.

For both calibration systems, precise astrometric measurements with Hipparcos are available, which are shown in Tab. 4.

Table 4: Hipparcos measurements of the NaCo calibration binaries

Binary	Sep [arcsec]	PA [°]
HIP 73357	8.433 ± 0.023	337.34 ± 0.16
HIP 6445	8.356 ± 0.010	220.98 ± 0.07

The Hipparcos measurements were obtained in epoch 1991.25, while the science data was taken in the second half of 2009. HIP 73357 is located at a distance of 102.25 pc from the sun. Both components are of spectral type A (Mason et al. 2001). Assuming a total system mass of $\sim 3\,M_\odot$ and a circular orbit with a radius of 8.4 arcsec, the orbital period of the system would be approximately 14600 yr. In the case of an orbit which is viewed edge-on, this would mean that the separation of the two components would change by $\sim 2\,$mas/yr or 41 mas in the $\sim 18\,$yr time difference between the Hipparcos measurement and the science epochs. In the case of a face-on orbit, the PA would change by $\sim 0.025°$/yr or $\sim 0.45°$ in 18 yr. This simple estimate shows that the possible orbit motion of the calibration binaries needs to be considered.

For both calibration binaries, additional astrometric data points taken over the past $\sim 170\,$yr are available in the Washington Double Star Catalog (WDS, Mason et al. 2001). With these data points it is possible to fit the linear change of separation and position angle of the binary components. The corresponding diagrams for both binaries are shown in Fig. 17.

In the case of HIP 73357, 27 data points are available which yield a linear decrease in position angle of $0.0397 \pm 0.0066°$/yr and a decrease in separation of 0.0019 ± 0.0012 arcsec/yr. For HIP 6445 only 8 data points were available, yielding an increase in position angle of $0.0053 \pm 0.0061°$/yr and an increase in separation of 0.0018 ± 0.0011 arcsec/yr. It is, however, problematic that the WDS does not give any uncertainties for any of the astrometric

(a) PA of HIP 73357

(b) Separation of HIP 73357

(c) PA of HIP 6445

(d) Separation of HIP 6445
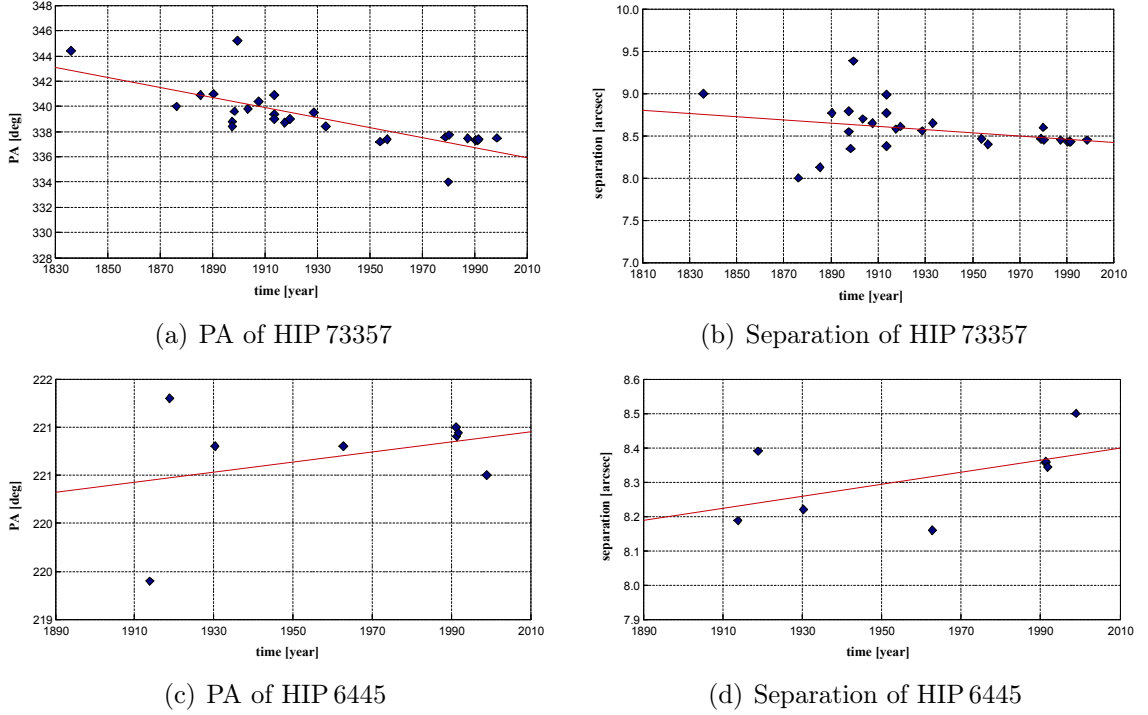
Figure 17: WDS astrometric data points for HIP 73357 and HIP 6445. The red lines indicate the linear fit to the change of position angle and separation over time.

data points. In addition, the data points show a large scatter, which is especially problematic in the case of HIP 6445 where only a few data points are available.

Given the calculated rate of change in separation and position angle, it is possible to extrapolate the ephemerides of both binaries at the time of the science epochs from the Hipparcos epoch. To then determine pixel scale and orientation of the detector, the detector positions of both binary components are measured in each individual jitter position in the respective observing night. This is done to account for geometric distortion of the detector. The measurements are done with ESO-MIDAS (**M**unich **I**mage **D**ata **A**nalysis **S**ystem, Warmels 1992), by fitting a two dimensional Gaussian to the star positions. Pixel scale and orientation for each individual jitter position can then be calculated and the results averaged. The resulting pixel scales and orientations are shown in Tab. 5. Additionally, the pixel scales are plotted versus time in Fig. 18.

Table 5: Astrometric calibration of all VLT/NaCo epochs using WDS orbital motion fit

Epoch	Calibrator	Pixel scale [arcsec/pixel]	Orientation [°]
2009.495	HIP 73357	0.013204 ± 0.000070	0.05 ± 0.28
2009.497	HIP 73357	0.013202 ± 0.000070	0.07 ± 0.28
2009.500	HIP 6445	0.013309 ± 0.000048	0.50 ± 0.18
2009.506	HIP 73357	0.013202 ± 0.000050	0.05 ± 0.20
2009.623	HIP 73357	0.013200 ± 0.000071	0.15 ± 0.28
2009.702	HIP 6445	0.013320 ± 0.000048	0.46 ± 0.19
2009.751	HIP 6445	0.013312 ± 0.000048	0.46 ± 0.18

Figure 18:   Derived pixel scales of NaCo S 13 for the science epochs versus time, after pre-calibration of the calibration binaries with WDS data.

It can be seen that the pixel scales derived from each binary are consistent in different epochs, while they vary significantly betwen the two binaries. This suggests that the instrument itself is stable within the uncertainties of the measurements, but that the orbital motion correction for the calibration binaries, as derived from the WDS data, is inaccurate. This is not entirely suprising, given the large scatter of the data points and particularly the few data points available for HIP 6445.

To correct for this discrepancy, a more precise calibration of the binary ephemerides is necessary. For this purpose, images of the globular cluster 47 Tuc were used. These were taken approximately one year after the science epochs with VLT/NaCo in the frame of a different observing program alongside images of the two calibration binaries. HIP 6445 and 47 Tuc were imaged in epoch 2010.604 with the NaCO S 27 objective, while HIP 73357 was imaged in epoch 2010.631 alongside 47 Tuc with the NaCo S 13 objective. For 47 Tuc, precise astrometry from HST observations is avilable. In Fig. 19, an HST/ACS image of 47 Tuc is shown. The field of view of the NaCo S 13 objective is indicated.

GAIA (**G**raphical **A**stronomy and **I**mage **A**nalysis tool,Draper 2000) and the included SEXTRACTOR (**S**ource **Extractor**, Bertin and Arnouts 1996) were used to extract the star positions from the the HST image, and to create an astrometric reference catalog. The same was done for the NaCo images of 47 Tuc. A PYTHON routine was then written to match the NaCo catalogs with the reference and compute the pixel scales and detector orientations for each pair of stars. Sigma clipping was then applied to exclude all stars
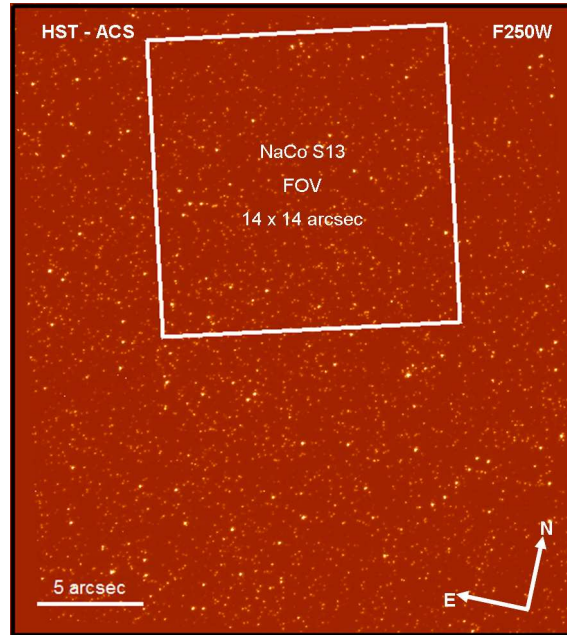
Figure 19: HST/ACS image of 47 Tuc taken on 2002 July 24. The white rectangle indicates the field of view of NaCo S 13. The image was taken with the F 250 W wide band filter in the ultra-violet.

from the NaCo catalogs which produced significantly different pixel scales and orientations. These discrepancies are most likely caused by a higher proper motion of such stars and hence larger deviations from the measured HST positions.

The NaCo images of both 47 Tuc observing epochs are shown in Fig. 20. Stars that were used for astrometric calibration are marked with white circles.

For epoch 2010.604, a pixel scale of 0.013272 ± 0.000051 arcsec/pixel, and a detector orientation of $0.41° \pm 0.18°$ were calculated. In the case of epoch 2010.631, the pixel scale is larger due to the S 27 objective of NaCo. It was calculated to be 0.027083 ± 0.000059 arcsec/pixel. Detector orientation in the same epoch is $0.52° \pm 0.16°$.

After calibrating the detector with the 47 Tuc images, the separation and position angle of both binary stars could be measured in the respective observing epochs. The results are listed in Tab. 6. With these precise astrometric measurements and the aforementioned Hipparcos measurements of epoch 1991.25, the linear orbit motion between the two epochs was calculated. For HIP 73357 the result is an increase in separation of 0.0008 ± 0.0015 arcsec/yr and a decrease of the position angle of $0.016 \pm 0.012°$/yr. In the case of HIP 6445, there is an increase in separation of 0.0004 ± 0.0017 arcsec/yr and a decrease of the position angle of $0.005 \pm 0.010°$/yr. The ephemerides for both binaries for the 2009 science epochs were calculated using these values. The results are listed as well in Tab.6.

With the new calculated ephemerides, the pixel scales and orientations of the 2009 images were recalculated. The results are listed in Tab. 7, and the resulting pixel scales are ploted versus time in Fig. 21. The new pixel scales now only vary within their uncertainties
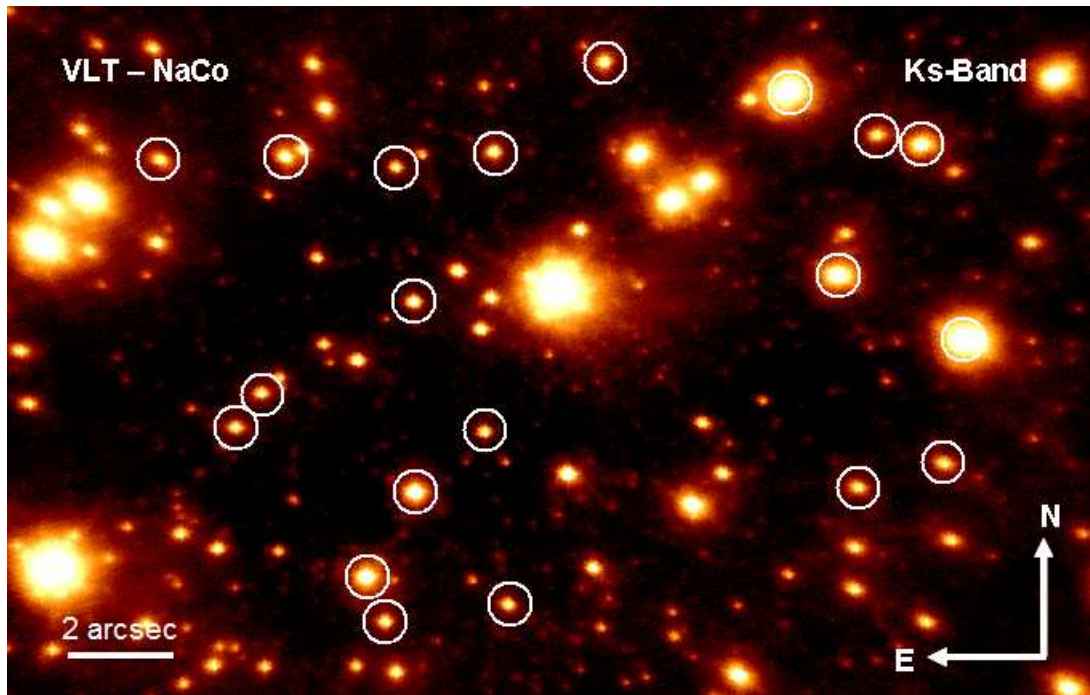
(a) Epoch 2010.631
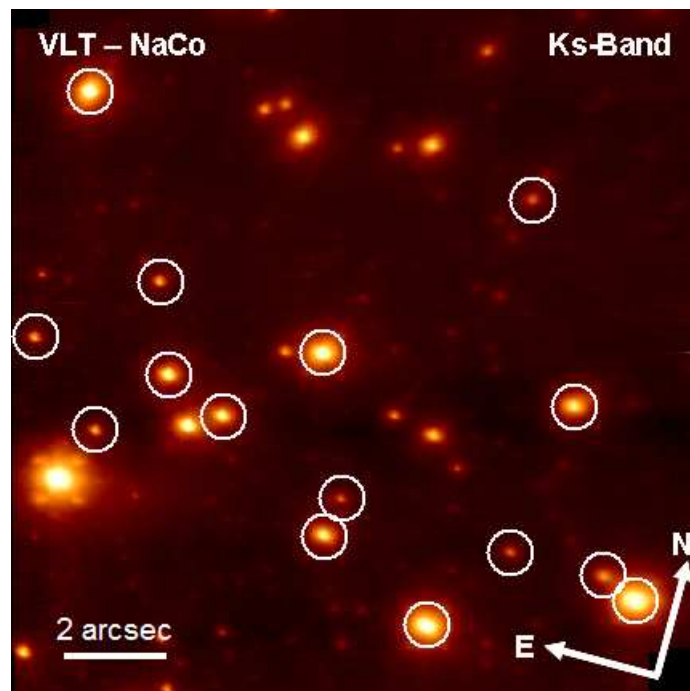
(b) Epoch 2010.604

Figure 20: VLT/NaCo images of the globular cluster 47 Tuc. The stars marked with white circles were used for astrometric calibration. The image in epoch 2010.631 was taken with the S 27 objective, while the image in epoch 2010.604 was taken with the S 13 objective.

and are not significantly different for the two calibration binaries. The orientations of the images in the different observing epochs still vary slightly with the calibration binary, although the variance has been significantly reduced in regard to the WDS calibration. This might indicate that the orbital motion of the calibrators is not described well with the linear

approximation that was used. The variation is, however, only in the order of 1σ and is therefore deemed acceptable.

Table 6: 47 Tuc-calibrated ephemerides of the NaCo calibration binaries

Binary	Epoch [yr]	Sep [arcsec]	PA [°]	Note
HIP 73357	2010.631	8.449 ± 0.019	337.04 ± 0.17	measured
HIP 73357	2009.623	8.448 ± 0.020	337.05 ± 0.19	calculated
HIP 73357	2009.506	8.448 ± 0.020	337.06 ± 0.19	calculated
HIP 6445	2010.604	8.365 ± 0.032	220.88 ± 0.19	measured
HIP 6445	2009.751	8.364 ± 0.034	220.88 ± 0.20	calculated
HIP 6445	2009.702	8.364 ± 0.034	220.88 ± 0.20	calculated

Table 7: Final astrometric calibration of all VLT/NaCo epochs

Epoch	Calibrator	Pixel scale [arcsec/pixel]	Orientation [°]
2009.495	HIP 73357	0.013281 ± 0.000032	0.49 ± 0.19
2009.497	HIP 73357	0.013279 ± 0.000032	0.51 ± 0.19
2009.500	HIP 6445	0.013279 ± 0.000054	0.29 ± 0.20
2009.506	HIP 73357	0.013279 ± 0.000032	0.49 ± 0.19
2009.623	HIP 73357	0.013278 ± 0.000032	0.59 ± 0.19
2009.702	HIP 6445	0.013282 ± 0.000054	0.27 ± 0.20
2009.751	HIP 6445	0.013274 ± 0.000053	0.26 ± 0.20

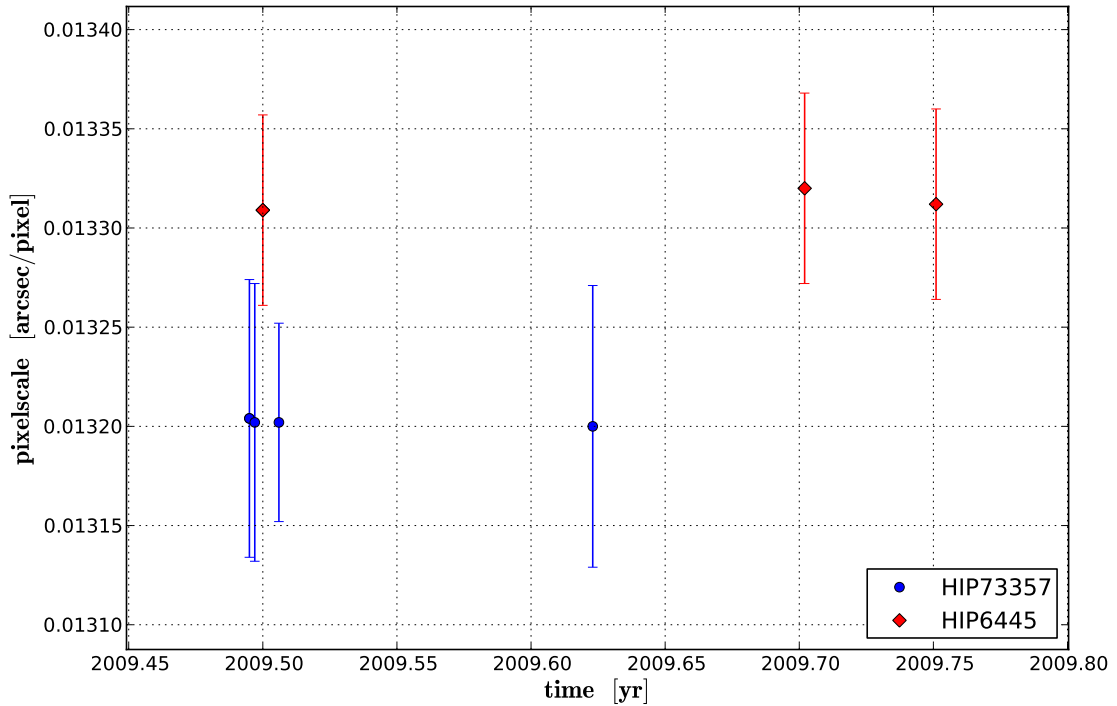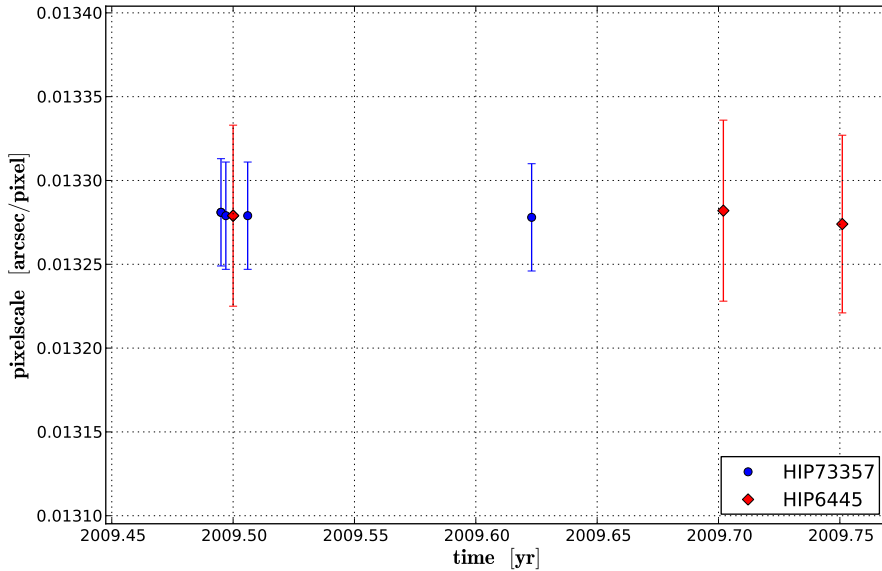Figure 21: Derived pixel scales of NaCo S 13 for the science epochs versus time, after pre-calibration of the calibration binaries with the globular cluster 47 Tuc.

Measurement

All astrometric measurements were done with ESO-MIDAS in the final reduced images. A two dimensional Gaussian was fitted to measure the primary stars' positions. The PSFs of the primaries were then removed in the way described in the previous section before the companion positions were measured. In the case of HD 130948 BC, the center of light of the unresolved BC companion was measured, rather than fitting a Gaussian, since the PSF was extended along the BC direction.

For each target, the pixel scale and orientation derived for the specific observing epoch was then used to convert pixel coordinates into separation and position angle. For HD 203030, no calibrator taken with the S 27 objective was available in the 2009 observing run. Therefore the pixel scale provided in the image header (0.02715 arcsec/pixel) was adopted. This pixel scale agrees within $1.4\,\sigma$ with the pixel scale calculated for the S 27 objective in 2010 (with 47 Tuc as calibrator).

To calculate the uncertainties of the astrometric data points, the $1\,\sigma$ measurement errors of the pixel positions of primary and companion, as well as the uncertainty of pixel scale and detector orientation were considered. In the case of HD 203030 there is no uncertainty given for the pixel scale provided in the image header. Hence, the uncertainty of the pixel scale of the 2010 calibration epoch was adopted as a typical uncertainty for the S 27 pixel scale.

All VLT/NaCo astrometric data points of the target stars are listed in Tab. 8.

Table 8: VLT/NaCo astrometric data points for all discussed targets

Target	Epoch	Separation [arcsec]	PA [°]
HD130948[1]	2009.506	2.6007 ± 0.0074	102.21 ± 0.25
1RXS J160929.1-210524	2009.623	2.2062 ± 0.0056	27.25 ± 0.22
UScoCTIO 108	2009.623	4.579 ± 0.015	176.96 ± 0.27
HD 203030	2009.637	11.976 ± 0.029	109.09 ± 0.25
GSC 08047-00232	2009.702	3.2316 ± 0.0135	358.53 ± 0.24
DH Tau	2009.751	2.3464 ± 0.0097	138.47 ± 0.24

[1] measurement of the photocenter of the BC component relative to A

4.2 Calar Alto Data

Calibration

Several binary stars were imaged as astrometric calibrators for the two Calar Alto observing epochs of 2002.318 and 2006.288. For all stars, precise astrometric measurements from Hipparcos are avilable, as well as additional astrometric data points from the WDS. The Hipparcos epoch was again used as the starting point, then the linear orbital motion as fitted by the WDS data points was considered. To also take field distortions into account,

the separation and position angle of the binaries were measured at different jitter positions and the results were averaged.

In the case of the 2006 epoch, the two binaries HIP 43100 and HIP 31515 were used for the astrometric calibration. The Hipparcos measurements of these two binaries are listed in Tab. 9.

Table 9: Hipparcos measurements of the Calar Alto calibration binaries

Binary	Separation [arcsec]	PA [°]
HIP 43100	30.483 ± 0.013	307.55 ± 0.02
HIP 31515	30.233 ± 0.007	106.43 ± 0.01

First the pixel scale and orientation for each binary were calculated, resulting in 0.07738 ± 0.00049 arcsec/pixel and $21.06° \pm 0.46°$ for HIP 43100, and 0.07747 ± 0.00019 arcsec/pixel and $21.03° \pm 0.07°$ for HIP 31515. Then the weighted average was derived. For weighting, the number of available measurements was used, which is 14 for HIP 43100 and 6 for HIP 31515. The final averaged result is listed in Tab. 10.

The calibration for the 2002 epoch was done by Mugrauer et al. (2004), who also list the calibration binaries used. The result is as well listed in Tab. 10.

Table 10: Final astrometric calibration of both Calar Alto epochs

Epoch [year]	Pixel scale [arcsec/pixel]	Orientation [°]
2002.318[1]	0.07760 ± 0.00030	22.27 ± 0.05
2006.288	0.07741 ± 0.00040	21.05 ± 0.34

[1] as reported in Mugrauer et al. (2004)

Measurement

Although the primary stars were saturated in both observing epochs, there was enough of the flanks of their PSFs left to again fit a two dimensional Gaussian to the stars with ESO-MIDAS. After this measurement of the stars' positions, their PSFs were subtracted to enable a high precision measurement of the companions' positions. The BC binary was again not resolved but the PSF was slightly extended in BC direction. The position of the photocenter of the BC system was measured using a CENTROID algorithm.

With the pixel positions and the calibrated pixel scale and image orientation, the separation and position angle of the BC system in regard to A were calculated. The final astrometric data points are listed in Tab. 11.

Table 11: Calar Alto astrometric data points for the HD 130948 system

Epoch [year]	Separation [arcsec]	PA [°]
2002.318	2.6135 ± 0.0267	103.37 ± 0.47
2006.288	2.6152 ± 0.0323	102.10 ± 0.78

4.3 Archive Data

4.3.1 Gemini-North Data

Calibration

A precise astrometric calibration of the data taken with the Gemini North Telescope was not possible, since no astrometric calibrators were available in the Gemini Science Archive. In particular, none of the targets imaged in the same nights as the science target were suitable for an astrometric calibration.

In the case of the 2001 and 2002 Hokupa'a/QuIRC observation epochs of HD 130948, the astrometry web page of the instrument (Rigaut 2000) is utilized. An average pixel scale of 0.01998 ± 0.00008 arcsec/pixel is given, which is inferred from binary observations. The average orientation of the detector is given with $0.30° \pm 0.07°$. In addition, the author states that the instrument's orientation shows some erratic behavior with changes in the order of $\sim 1°$ between observing nights. Hence, for this work, a detector orientation of $0.30° \pm 1°$ was adopted.

For the 2005 NIRI observation epoch there was no additional information about the general astrometric accuracy of the instrument available. Therefore, the information given in the image headers was adopted. The pixel scale is given with 0.021859 arcsec/pixel, but without confidentiality limit. The orientation of the detector was changing over time since all images in this observing epoch were taken as part of an ADI sequence. For all astrometric measurements, the detector orientation was taken from the header of the images in question. Considering that no uncertainty limit is given for pixel scale and detector orientation, these uncertainties are neglected for astrometric calculations of this observing epoch. This implies that the astrometric accuracy of these calculations is overestimated.

Measurement

The Hokupa'a/QuIRC and NIRI images are very different. While the former are only slightly saturated, the NIRI images show a strong saturation of the primary with large negative values in the PSF core. Furthermore, in the 2001 and 2002 QuIRC images, the BC binary companion is clearly resolved, while this is only marginaly the case in the 2005 NIRI epoch due to the less favorable orbit position of B and C. This distinctive data required the utilization of different measurement techniques.

Hokupa'a/QuIRC - Measurement

The primary position in the Hokupa'a/QuIRC images was measured using the CENTROID algorithm of ESO-MIDAS. The typical uncertainty of these measurements was in the order of ~0.1 pixel. The position of the resolved companion could not be measured in the same way, since the respective ESO-MIDAS task does not give results for "dubious" sources, meaning extended sources with more than one peak. The independent measurements of the B and C components were attempted by fitting a Gaussian to the respective positions using again ESO-MIDAS. The overall accuracy of these measurements was, however, only in the order of ~0.5 pixel. Precision could be increased by subtracting the PSF of the C component before measuring the position of the B component and vice versa. The accuracy of this method is nonetheless limited by the availablity of a good reference PSF for subtraction. Since the primary was saturated and there are no other objects in the field besides the BC companion, it was not possible to build a reference PSF. Finally, a subtraction by simulated rotation to increase the overall astrometric accuracy was evaluated. However, due to the small separation between B and C (~0.1 arcsec), the flanks of the non-subtracted component would usualy still suffer from under-subtraction of non-radial symmetric artifacts of the PSF of the subtracted component.

Due to the discussed difficulties, it was decided to measure the center of light of the BC binary instead of measuring the position of the B and C components separately. For this purpose a PYTHON program was created, the source code of which is given in appendix A.2. The program takes the approximate detector position of the object to be measured and the size of the measuring box as input. The measuring box is centered on the provided coordinates. The program then measures the background level of the image by averaging pixel values in four directly adjacent boxes left, right, below and above the measuring box. The same boxes are also used to calculate the background noise by means of the standard deviation. In the next step, all pixels in the measuring box whose value is smaller than three times the noise plus the background level are set to zero. This is done to avoid a contamination of the astrometric measurement result by background pixels which carry no object information. Once this is completed, the measurement box is checked for "lone pixels", meaning single pixels which are not connected to any other pixel which carries object information. Such "lone pixels" could be the result of a poorly compensated "hot pixel" of the detector or of a cosmic ray striking the detector on that position. All identified "lone pixels" are set to zero as well. The remaining non-zero pixels in the measuring box are then used to calculate the photocenter of the desired object. The built-in PYTHON function CENTRE_OF_MASS, which calculates the barycenter of a provided matrix, is utilized for this calculation.

The whole process of measurement as described is repeated a total of 6 times starting with the box size provided by the user and followed by box sizes that are increased by one pixel

on each successive step. The result of each measurement is saved, and the average and standard deviation of all measurements is computed. This is done to consider the effects of different box sizes on the outcome of the measurement. In addition, the uncertainty of the measurement for the initial box size provided by the user is calculated by adopting the calculated background noise as 1σ uncertainty for each pixel value. Analogous to the measurement, only the non-zero object pixels are considered. The total uncertainty of the measurement is then the square root of the quadratic sum of the uncertainty introduced by box size and background noise. In the case of the 2001 Hokupa'a/QuIRC images, separation and position angle of the BC binary companion with respect to the primary star were measured separately in six PSF subtracted images and then averaged. The standard deviation of these six individual measurements was approximately ten times smaller than the individual measurement errors. Hence the average of the measurement uncertainties was adopted as the total uncertainty.

The analogous procedure was employed for the sixteen images available in the 2002 Hokupa'a/QuIRC observation epoch. The results are listed in Tab. 12.

NIRI - Measurement

In the case of the 2005 NIRI images, it was not possible to measure the position of the primary star directly due to the strong saturation of the PSF core. Instead, the inverse images were used, which show a peak in the area of strongest saturation. The positions of these "saturation peaks" were then measured with the CENTROID algorithm of ESO-MIDAS. The positions of the BC companion were measured in the PSF subtracted images using the same algorithm.

Astrometric measurements were done in a total of six images: two at the beginning, two in the middle and two at the end of the ADI sequence. Separation and position angle of the BC companion with respect to A was calculated for each of these images. The results for all images were then averaged and the standard deviation was computed. Since the standard deviation exceeded the individual measurement errors by a factor of $\sim$10, the standard deviation was adopted as the total uncertainty of this astrometric measurement. The result is listed in Tab. 12 alongside the results of the previous Gemini North measurements.

Table 12: Gemini North astrometric data points for the HD 130948 system

Instrument	Epoch [year]	Separation [arcsec]	PA [°]
Hokupa'a/QuIRC	2001.492	2.627 ± 0.012	105.2 ± 1.1
Hokupa'a/QuIRC	2002.311	2.603 ± 0.032	104.9 ± 1.1
NIRI	2005.295	2.610 ± 0.014	104.6 ± 0.5

4.3.2   HST Data

Calibration

The 2002 and 2005 HST observation epochs of HD 130948 do not require a classical astrometric calibration because the HST calibrates its position by locking onto two guide stars with its Fine Guidance Sensors (Nelan et al. 1998) for each observation. The respective information for pixel scale and detector orientation can be extracted from the image headers. After correction for the (severe) geometric distortions of the instrument by the MultiDrizzle pipeline, the pixel scale in both observation epochs was scaled to 0.025001 arcsec/pixel. The accuracy of this pixel scale was examined by Eisenbeiss (2011), who found that the uncertainty is much smaller than 1 %.

The detector orientation varies between both observation epochs. In the 2002 epoch it was 261.869° and in the 2005 it was 81.000°. These are the orientations as recorded in the ORIENTAT keyword of the HST file header. They have been corrected for the instrument position with respect to the rotation axis of the HST. The typical offset between the commanded and executed roll of the HST (and hence the orientation of the instuments) is only 0.003° (Fruchter and Sosey 2009).

In both cases (pixel scale and orientation), the uncertainties are at least one order of magnitude smaller than the uncertainties inherent in the measuring process of the objects' detector positions. Hence these uncertainties were neglected in the following calculations.

Measurement

The position of the primary star was measured in the pipeline-reduced images using the CENTROID algorithm of ESO-MIDAS. The companion position was measured the same way in the PSF subtracted images. Different measuring box sizes of the respective ESO-MIDAS task were used to research the stability of the computed positions. In the case of the primaries, the standard deviation of these multiple measurements was slightly larger than the average measurement uncertainty (0.31 pixel on average compared to 0.25 pixel), and was hence adopted as the total uncertainty of the measurement. In the case of the companions, the measurement uncertainties were clearly dominant over the standard deviation of multiple measurements (0.22 pixel on average compared to 0.06 pixel), and were therefore adopted as the total positional uncertainty of the companion.

The results for both observation epochs are listed in Tab. 13.

Table 13: HST-ACS astrometric data points for the HD 130948 system

Epoch [year]	Separation [arcsec]	PA [°]
2002.683	2.634 ± 0.012	103.45 ± 0.17
2005.148	2.615 ± 0.012	102.02 ± 0.17

4.3.3   Subaru Data

Calibration

A precise astrometric calibration of the Subaru observation epoch was unfortunately not possible, since no suitable targets for an astrometric calibration were imaged either within the same night or in a timeframe of a few days around the observation date. Thus, the pixel scale and image orientation provided in the image headers were utilized. The extracted pixel scale was 0.022428 arcsec/pixel and the image orientation was $180°$. There were no uncertainties provided and hence the total accuracy of this astrometric measurement is overestimated.

Measurement

The primary star is strongly saturated in the Subaru observation with large negative count values in the PSF core. There was not enough left of the flanks of the PSF to fit a Gaussian to the star position. It was, however, possible to determine the position of the "peak" of the saturation by centeroiding the saturated PSF core in the inverse image with ESO-MIDAS. The uncertainty of this measurement was 0.27 pixel. Since the strongest saturation should occur at the peak position of the star, this measurement should reflect the star position within its uncertainties.

The center of light of the companions was determined in the PSF subtracted image with ESO-MIDAS. The overall result of this astrometric mesurement is given in Tab. 14.

Table 14: Subaru astrometric data points for the HD 130948 system

Epoch [year]	Separation [arcsec]	PA [°]
2003.421	2.611 ± 0.016	104.10 ± 0.21

5 Data Analysis and Results

5.1 Proper Motion Analysis

The astrometric data points compiled in the previous section combined with literature values were used to examine the proper motion of the substellar companions with respect to their host stars.

5.1.1 HD 130948

In addition to the already mentioned observation epochs, three literature data points were adopted for the analysis. On 2006 May 9, HD 130948 was observed by Serabyn et al. (2009) using a small (1.6 m) well-corrected sub-aperture of the Palomar Hale telescope in combination with the Palomar AO system (PALAO, Troy et al. 2000) and the PHARO camera (Palomar High-Angular-Resolution Observer, Brandl et al. 1997). They utilized the K_s-band for a total integration time of 67 s. The BC binary was not resolved. The observations were astrometrically calibrated with images of binary stars. They calculate a pixel scale of 80 ± 2 mas/pixel and a typical uncertainty of the image orientation of $\pm 2°$. Geißler et al. (2008) observed the HD 130948 system on 2006 July 9 with VLT/VISIR, in the mid-infrared. They used the PAH1 filter of the instrument, which has its maximum throughput in the N-band. The target was observed in chop-nod mode to sample the bright infrared sky background. The total effective integration time was 43.1 s split into single exposures of 0.02 s. They detected the BC companion but could not resolve it. They did not observe any astrometric calibrators but used the astrometric solution provided in the image headers. Labadie et al. (2011) observed HD 130948 approximately two years later on 2008 July 25 with the 2.5 m Nordic Telescope (NOT) and the FastCam (Oscoz et al. 2008) instrument in the I-band. They employed the lucky imaging observing technique taking 30000 short exposures of 3 ms. They detected the BC companion, but were also unable to resolve it. They calibrated their images with observations of the globular cluster M 15 taken in the same nights as the science observations. A pixel scale of 0.03117 ± 0.00003 arcsec/pixel is given, but no information about the image orientation is provided.

Since only the photocenter of the BC system was measured, the data points needed to be corrected to the barycenter. The orbital solution of the BC system derived by Dupuy et al. (2009) was utilized, along with the flux ratios of B and C listed in Tab. 17 to calculate the offset between photocenter and barycenter of the system at the times of the measurements. The flux ratios in the J-,H- and K-band, as well as in the HST F850LP filter, were derived from the photometric measurements by Dupuy et al. (2009). Since there are no resolved images of B and C available in the I-band, the masses of both components as computed by Dupuy et al. (2009) were utilized in combination with the DUSTY models (Chabrier

Table 15: Astrometric measurements of the HD 130948 system. The position of the pho-
tocenter of the BC system was measured.

Epoch [yr]	Sep [arcsec]	PA [°]	Reference
2001.492	2.627 ± 0.012	105.2 ± 1.1	this work
2002.311	2.603 ± 0.012	104.9 ± 1.1	this work
2002.320	2.614 ± 0.027	103.37 ± 0.47	this work
2002.683	2.634 ± 0.012	103.45 ± 0.17	this work
2003.421	2.609 ± 0.016	104.05 ± 0.21	this work
2005.148	2.615 ± 0.012	102.02 ± 0.17	this work
2005.295	2.610 ± 0.014	104.6 ± 0.5	this work
2006.290	2.615 ± 0.032	102.1 ± 0.8	this work
2006.355	2.45 ± 0.10	105 ± 2	Serabyn et al. (2009)
2006.522	2.54 ± 0.05	103.9 ± 2.4	Geißler et al. (2008)
2008.566	2.561 ± 0.007	102.70 ± 0.20	Labadie et al. (2011)
2009.506	2.6007 ± 0.0074	102.21 ± 0.25	this work

et al. 2000) for an age of 500 Myr to compute the flux ratio. Since there is no such model information available in the N-band, the K-band flux ratio was used for correction in the case of the mid-infrared observation, with the knowledge that the flux ratio in this case was probably slightly overestimated. The final corrected data points are listed in Tab. 17. The apparent orbit of the C component around the B component is shown in Fig. 22. For each observation epoch in Tab. 17, the position of the C component on the orbit is indicated along with the calculated photocenter and barycenter for this epoch. In addition, images of the BC system from different observing epochs are shown.

Table 16: Orbit solution for the BC binary system by Dupuy et al. (2009)

Semi-major Axis	a [mas]	121 ± 6
Eccentricity	e	$0.167^{+0.020}_{-0.015}$
Period	P [yr]	$9.9^{+0.6}_{-0.7}$
Inclination	i [deg]	$95.7^{+0.3}_{-0.2}$
Angle of Ascending Node	Ω [deg]	$133.15^{+0.15}_{-0.16}$
Argument of Periastron	ω [deg]	71^{+15}_{-14}
Time of Periastron Passage	T_0 [JD]	2454664.0 ± 110

Potter et al. (2002) found that the BC system is co-moving with the primary star within the uncertainties of their astrometric measurements. They stated that they cannot find any significant differential motion between BC and A. However, they only analyzed the system over a time baseline of ~ 1 yr.

In Fig. 23 the barycenter corrected astrometric measurements are shown. The wobbled lines represent the position that a non-moving background object would have in the respective observation epochs. The wobble is introduced by the parallactic motion of the star due to earth's revolution around the sun. The dashed lines represent the maximum expected differential motion in case of a circular orbit with a radius equal to the projected separation.
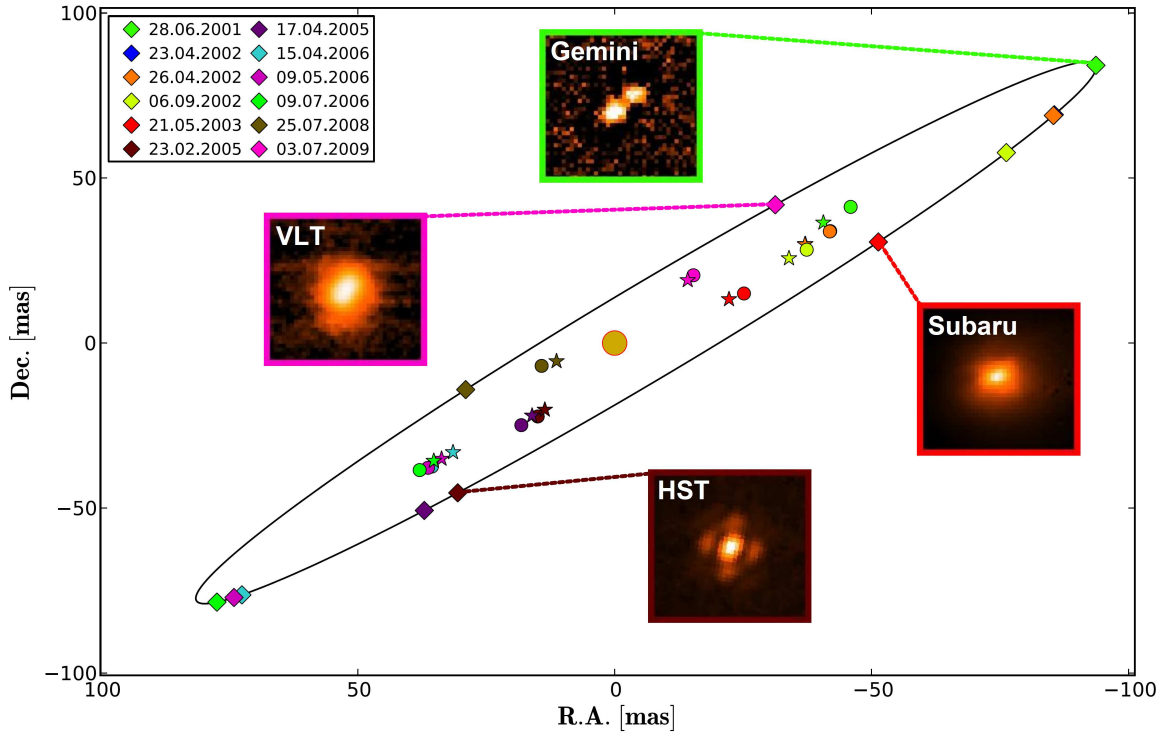
Figure 22: Orbit of the HD 130948 BC system as determined by Dupuy et al. (2009). For each observing epoch of the system (as listed in Tab. 15), the photocenter and barycenter of the HD 130948 BC system are indicated. Photocenters are marked by stars and barycenters are marked by circles. Photocenter and barycenter are coded in the same color as the respective position of the C component, indicated by diamonds. Images of the BC system are given for several observing epochs.

Table 17: Final barycenter corrected astrometric measurements of the HD 130948 system. Listed also are the filters in which the images were taken, and the flux ratio of the B and C component in the respective band. In the column astrometry it is indicated whether or not the astrometric measurements are well calibrated.

Epoch [yr]	Filter	Flux Ratio	Sep [arcsec]	PA [°]	Astrometry
2001.492	H	1.306	2.633 ± 0.012	105.3 ± 1.1	uncalibrated
2002.311	H	1.306	2.609 ± 0.012	105.0 ± 1.1	uncalibrated
2002.320	H	1.306	2.618 ± 0.027	103.45 ± 0.47	calibrated
2002.683	F850LP	1.247	2.638 ± 0.012	103.51 ± 0.17	calibrated
2003.421	H	1.306	2.611 ± 0.016	104.10 ± 0.21	uncalibrated
2005.148	F850LP	1.247	2.613 ± 0.012	102.00 ± 0.17	calibrated
2005.295	CH4 (short)	1.306	2.606 ± 0.014	104.6 ± 0.5	uncalibrated
2006.290	H	1.306	2.610 ± 0.032	102.0 ± 0.8	calibrated
2006.355	K_s	1.199	2.45 ± 0.10	105 ± 2	uncalibrated
2006.522	PAH1	1.199	2.54 ± 0.05	103.9 ± 2.4	uncalibrated
2008.566	I	1.563	2.559 ± 0.007	102.64 ± 0.20	calibrated
2009.506	NB 2.17	1.199	2.6024 ± 0.0074	102.23 ± 0.25	calibrated

In the case of the PA, the maximum differential motion would be expected for a face-on orbit, while in the case of the separation, maximum change would be expected for an edge-on orbit.

In both cases, the background hypothesis can be rejected on a high significance level of $35.2\,\sigma$ and $76.7\,\sigma$ for PA and separation respectively. Furthermore, differential motion between BC and A was detected. If the first Gemini measurement of 2001 is considered, as well as the VLT/NaCo observation of 2009, the differential motion is detected on a significance level of $2.2\,\sigma$ for PA and $2.7\,\sigma$ for separation. If the much more precise HST epoch of 2002 is taken as reference instead of the Gemini epoch, a higher significance of $4.2\,\sigma$ for PA and $2.5\,\sigma$ for separation can be calculated. In Fig. 24 the best fits to the change of PA and separation are shown. Since the uncertainties of the *uncalibrated* data points are underestimated, the *calibrated* data points were fitted separately as well. The data point by Serabyn et al. (2009) was considered *uncalibrated* due to its large uncertainties in comparison with the other data points. The change in PA of the *calibrated* data points is best fit by a linear function, yielding a decrease of $0.14 \pm 0.10\,\mathrm{deg/yr}$. If all data points are considered for fitting, a stronger decrease of $0.20 \pm 0.09\,\mathrm{deg/yr}$ is calculated. Both values are consistent with the value found by Labadie et al. (2011) through comparison of only two data points. In separation, linear fitting of the *calibrated* data points yields a decrease of $0.007 \pm 0.004\,\mathrm{arcsec/yr}$. If all data points are considered, this result changes only marginally to a decrease of $0.006 \pm 0.002\,\mathrm{arcsec/yr}$.

The fact that the separation changes only slightly, namely much less than the maximum expectation for an edge-on circular orbit, shows that the orbit is either far from edge-on (near face-on) and/or highly eccentric. And from the fact that the position angle change is between zero changes and maximum expectation for a face-on circular orbit, it can as well be concluded that the orbital inclination is between face-on and edge-on and/or highly eccentric.
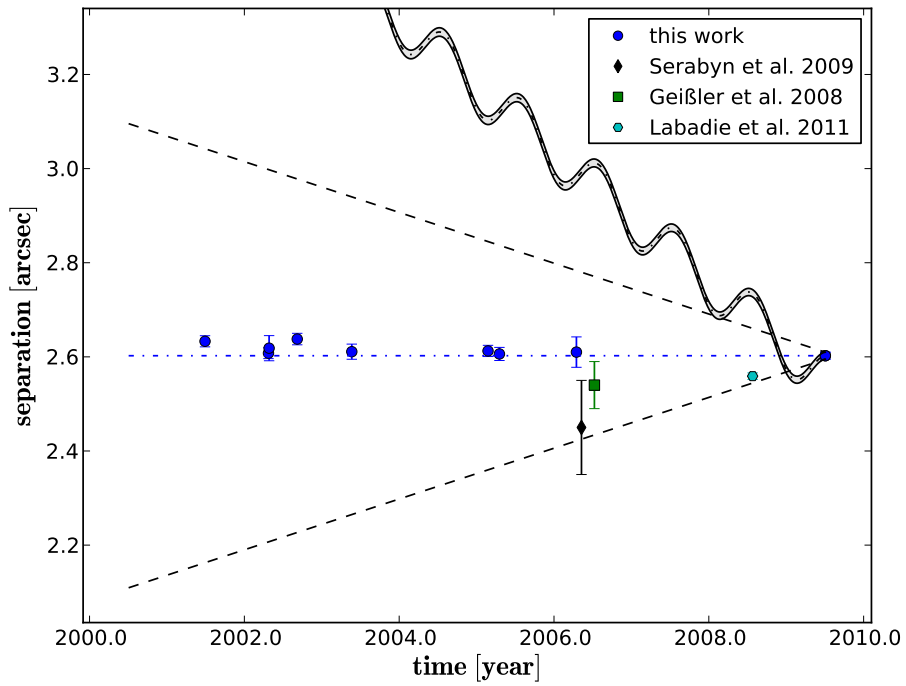
(a) Separation versus time
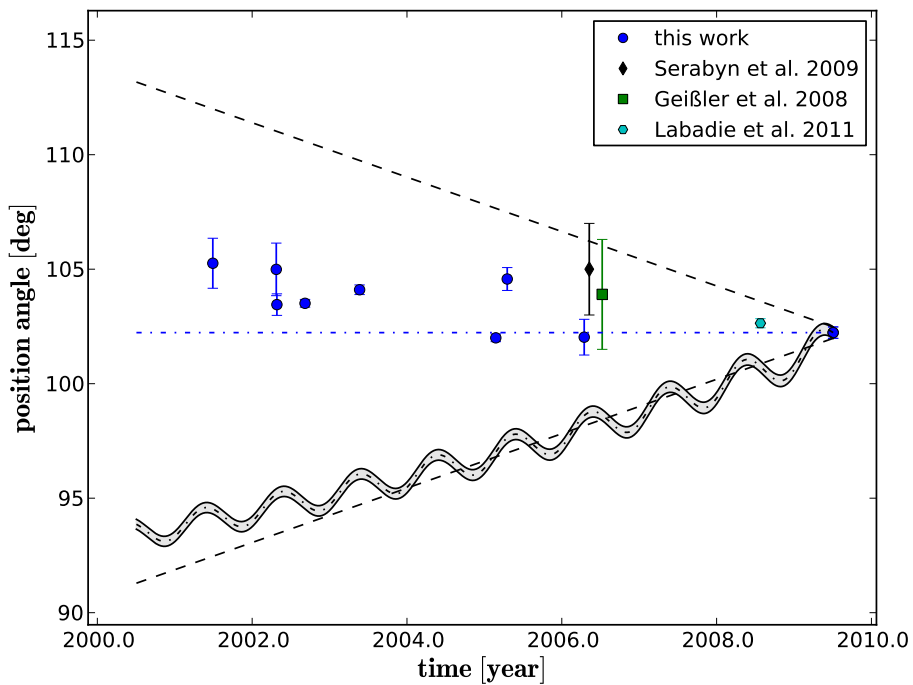
(b) PA versus time

Figure 23: Proper motion diagrams of the HD 130948 system. Origin of the data points is indicated by color and shape.

(a) Separation versus time

(b) PA versus time

Figure 24: Linear fit of the differential motion of HD 130948 A and BC. The red, dash-dotted lines represent the fits for all data points, while the blue, solid lines are the fits for the *calibrated* data points only.

5.1.2   HD 203030

There are four additional literature data points available for the HD 203030 system by Metchev and Hillenbrand (2006). They observed the system three times between 2002 and 2005 with the Hale 200 inch (5 m) telescope at the Palomar observatory, utilizing the PALAO AO system (**Pal**omar **A**daptive **O**ptics, Troy et al. 2000) and the PHARO camera (**P**alomar **H**igh-**A**ngular **R**esolution **O**bserver, Hayward et al. 2001). They took combinations of deep (long time exposed) coronagraphic images and short exposure non-coronagraphic images in J-, H- and K_s-band to measure the positions of the bright primary and the faint companion. The pixel scale of the instrument is 25.09 mas/pixel.

They also observed the system on 2005 July 12 with the Keck 10 m telescope, using the KeckII AO system (Wizinowich et al. 2000) and the NIRC2 instrument (Second Generation **N**ear **I**nfra**R**ed **C**amera, e.g. McLean and Sprayberry 2003). They employed the 20 mas/pixel pixel scale of the instrument for coronagraphic observations in the K_s-band.

All literature epochs were calibrated astrometrically by the authors with images of the visual binary WDS 18055+0230 taken in the same nights as the science observations. For this binary, a high grade astrometric orbit solution is available in the Sixth[6] Catalog of Orbits of Visual Binary Stars. Furthermore, there were distortion solutions available for both instruments by Metchev (2006), which the authors used for geometric distortion correction. They considered the uncertainties of the astrometric calibration and of the individual measurements for calculation of the total astrometric uncertainty of each data point.

Of the mentioned data points, only the first one taken on 2002 August 28 was explicitly given in Metchev and Hillenbrand (2006), but the others could be extracted from a figure therein with a precision of ~ 1.5 mas in separation and $\sim 0.01°$ in PA. All data points are listed in Tab. 18. Given the listed astrometric uncertainties, the additional uncertainties from the extraction of the data points is negligible.

Table 18: Astrometric measurements of the HD 203030 system.

Epoch [yr]	Sep [arcsec]	PA [°]	Reference
2002.658	11.923 ± 0.021	108.76 ± 0.12	Metchev and Hillenbrand (2006)
2003.541	11.918 ± 0.056	108.67 ± 0.19	Metchev and Hillenbrand (2006)
2004.486	11.880 ± 0.056	108.59 ± 0.21	Metchev and Hillenbrand (2006)
2005.533	11.926 ± 0.056	108.82 ± 0.34	Metchev and Hillenbrand (2006)
2009.637	11.976 ± 0.029	109.09 ± 0.25	this work

Considering the first astrometric data point of epoch 2002.658 and the latest VLT/NaCo measurement of epoch 2009.637, the background hypothesis can be rejected with $23.5\,\sigma$ in separation and with $4.5\,\sigma$ in PA. If all data points are taken into account, it is possible to fit a linear increase in separation of 7.9 ± 2.9 mas/yr and a linear increase in PA of

---

[6]See http://ad.usno.navy.mil /wds/orb6.html

$0.045° \pm 0.025°$ /yr. Both fits have a very low χ^2_{red} of 0.34 and 0.42 respectively, due to the large uncertainties of the independent measurements. However, the significance of the detected differential motion is low, with only $1.5\,\sigma$ in separation and $1.2\,\sigma$ in PA. The Keck data point of epoch 2005.533 and the VLT/NaCo data point of epoch 2009.637 would also be consistent with no differential motion. There is also no intrinsic differential motion detected in the data points by Metchev and Hillenbrand (2006). This could be due to the larger uncertainties and the shorter time difference between these measurements, but could also indicate that the fitted differential motion is caused by a systematic offset between the literature dataset and the VLT/NaCo measurement. The later alternative would be supported by the fact that the pixel scale of NaCo with the S27 objective was not calibrated as explained in section 4.1, but was only taken from the image header. Furthermore, it was not corrected for geometric distortions of the NaCo S27 setup, as there is no geometric distortion correction available. Given the large separation of $\sim 11.9\,$arcsec between primary and companion, a change in the pixel scale of $\sim 1\,\%$ could already lead to a change of separation in the order of $\sim 0.1\,$arcsec.

Given the above considerations, it remains doubtful if the detected differential motion between 2002 and 2009 is a real effect. An additional measurement with VLT/NaCo could shed some light on this question. If the fitted differential motion is taken into account as well as the precision of the VLT/NaCo measurement, a significant change in separation should be detectable after a time difference of $\sim 3.6\,$yr. For PA this takes about $\sim 5.5\,$yr. The system should hence be observed in the spring semester of 2013 if possible.

If the detected differential motion is indeed a real effect, then it would be consistent with an inclined and eccentric orbit, since changes in separation and PA are observed which are both smaller than predicted for a circular orbit.
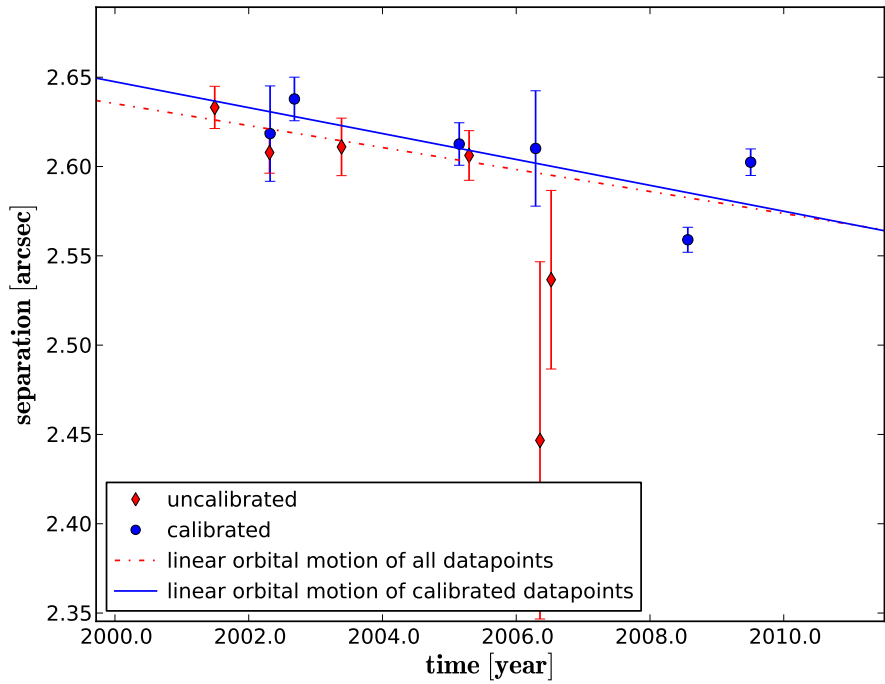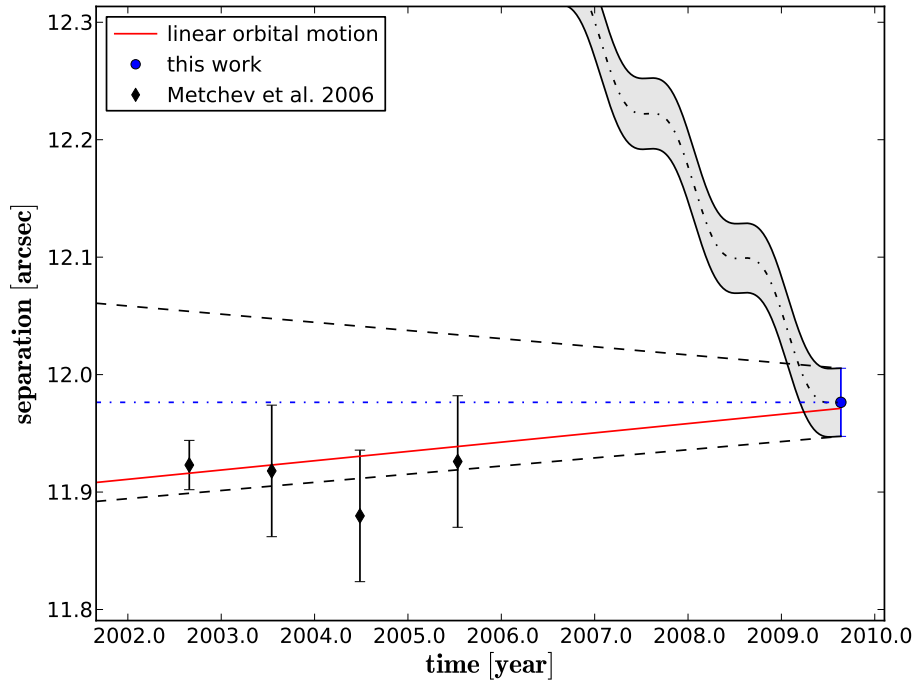
(a) Separation versus time
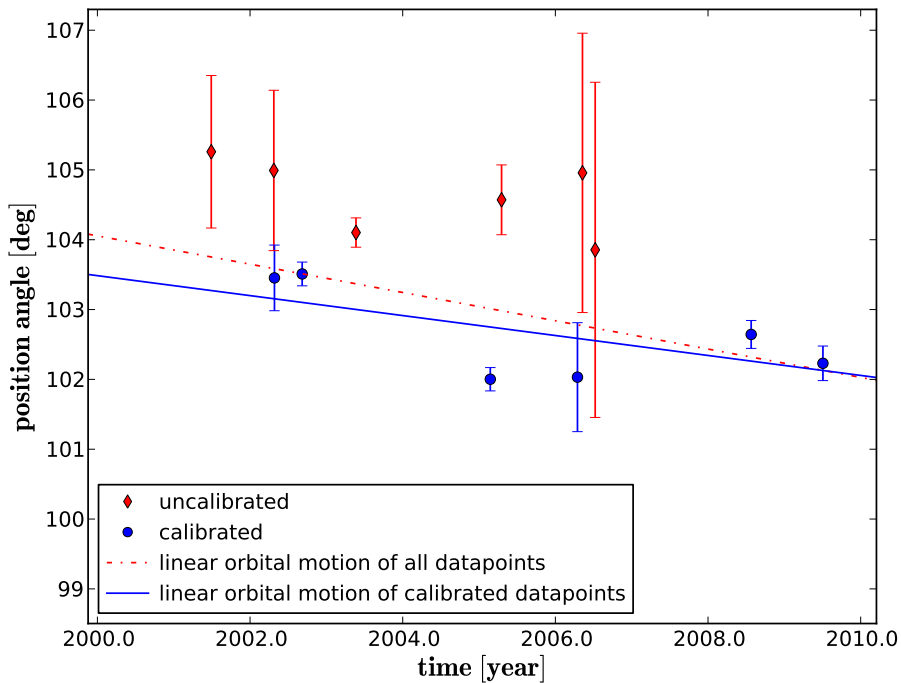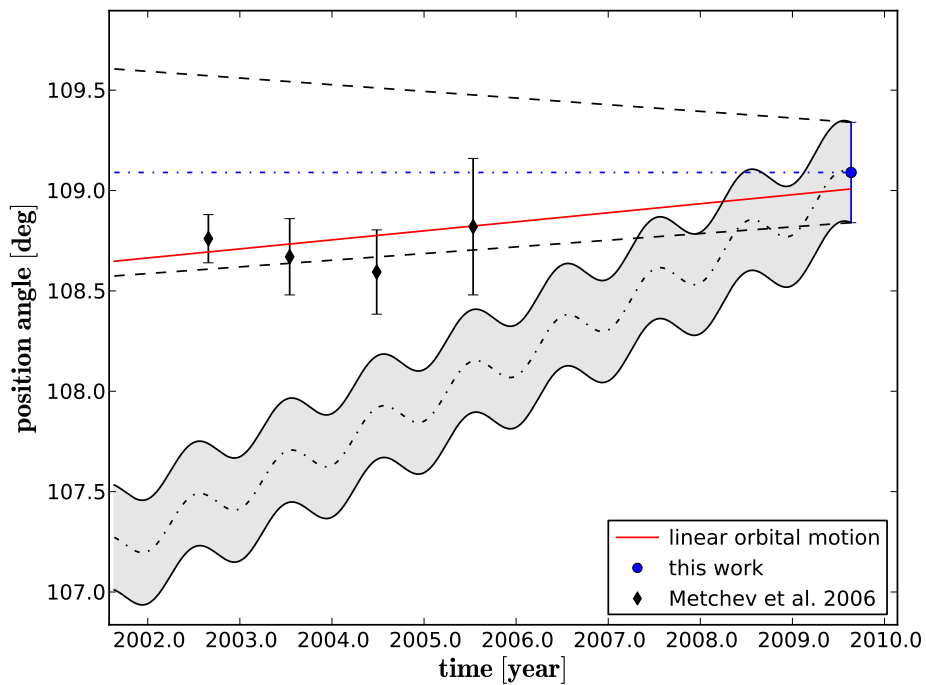

(b) PA versus time

Figure 25: Proper motion diagrams of the HD 203030 system. Origin of the data points is indicated by color and shape.

5.1.3   DH Tau

In addition to the VLT/NaCo observation, three more astrometric data points of the DH Tau system are available in Itoh et al. (2005). The first observation on 1999 January 17 was executed with the HST and the WFPC2 instrument (**W**ide-**F**ield **P**lanetary **C**amera **2**, Trauger et al. 1994). The Planetary Camera of WFPC2 has a pixel scale of 0.046 arcsec/pixel. HST data is astromatricaly calibrated during observation by locking onto two guide stars of known position and proper motion.

Itoh et al. (2005) also present two additional observations carried out with the Subaru telescope and the CIAO instrument. The observations were executed on 2002 November 23 and 2004 January 08. However, in 2003 the detector of the CIAO instrument was replaced with a new infrared array and hence the astrometric solution of the instrument changed slightly. Both CIAO data points should therefore be regarded as systematically uncorrelated measurements.

For the astrometric calibration of the 2002 data point, the authors used the astrometric solution presented in Itoh et al. (2002), wherein observations of the Trapezium cluster with the CIAO instrument are compared with reference observations of Simon et al. (1999). They calculated a pixel scale of 0.02125±0.000025 arcsec/pixel and provide a general uncertainty of the detector orientation of 0.073°. It should be noted that these astrometric calibrations were done in January of 2001, whereas the science observation was executed in November 2002, almost two years later. There is no information about the astrometric stability of the instrument provided in Itoh et al. (2005).

For the 2004 data point, a changed pixel scale of 0.02133±0.00002 arcsec/pixel after the instrument refurbishment is provided. There is, however, no information given as to how this astrometric solution was computed, especially if the Trapezium cluster was used again for calibration and if the astrometric calibration was done in the same night as the science observation. It is therefore possible that there are systematic offsets between these two data points.

For both CIAO data points, the total astrometric uncertainties include the uncertainty of the astrometric solution as well as the standard deviation of multiple measurements of the object positions. They do not include the measurement uncertainty of each single measurement, which can be up to 10 times larger than the standard deviation, e.g. as briefly discussed in section 4.3.1. Hence it could be that the uncertainties of these astrometric measurements are underestimated.

All astrometric measurements are listed in Tab. 19 and the corresponding proper motion diagrams are shown in Fig. 26.

In both proper motion diagrams a distinction is made between the HST and the CIAO data points of Itoh et al. (2005) due to the different instrument characteristics and astrometric calibrations. In separation, all three literature data points are consistent with the VLT/-

Table 19: Astrometric measurements of the DH Tau system

Epoch [yr]	Sep [arcsec]	PA [°]	Reference
1999.046	2.351 ± 0.001	139.36 ± 0.10	Itoh et al. (2005)
2002.896	2.340 ± 0.006	139.56 ± 0.17	Itoh et al. (2005)
2004.022	2.344 ± 0.003	139.83 ± 0.06	Itoh et al. (2005)
2009.751	2.3464 ± 0.0097	138.47 ± 0.24	this work

NaCo measurement of 2009.751, while in PA the data points differ significantly between the HST and the second CIAO measurement, and between the CIAO, HST and VLT/-NaCo measurements. The two CIAO PA measurements are indeed more consistent with a background object than with a co-moving object. There are, however, several indicators that the uncertainties of these measurements are significantly underestimated. Mayama et al. (2006) also used the Trapezium observations by Simon et al. (1999) as an astrometric reference to calibrate their own Subaru/CIAO observations of late 2002 and late 2004. They utilized similar instrument settings to Itoh et al. (2005) for their two observations of DH Tau, and imaged Trapezium in each observing night. They calculated a pixel scale of 0.0213±0.003 arcsec/pixel and a detector orientation of 5.7°±0.8° for their 2002 observations, and 0.0213±0.001 arcsec/pixel and 1.68°±0.27° for their 2004 observations. In both cases, the uncertainty of the pixel scale is approximately one order of magnitude larger than the one used by Itoh et al. (2005). Also, the uncertainty of the detector orientation alone is almost five times as big as the total estimated uncertainty for the PA in the respective CIAO measurement of DH Tau. A similar uncertainty of the detector orientation is also given in Neuhäuser et al. (2007), who used different astrometric calibrators. It seems therefore likely that the uncertainties of the astrometric measurements with CIAO are vastly underestimated, especially so if the uncertainties for each independent position measurement are considered, as already discussed. If the uncertainty of 0.8° for the PA of the 2002 measurement is used, the data point would be consistent with orbital motion as well as with the background hypothesis within $1\,\sigma$. In addition, it should be stressed that no information is provided on the astrometric calibrator used in the 2004 CIAO observation epoch, though it might be implied that Trapezium observations were also used. If a different calibrator was used, then this could have lead to additional systematic offsets between the two CIAO observation epochs.

Given these considerations, the two CIAO observations were not used to estimate a possible orbital motion of DH Tau B around A, and subsequently the linear orbital motion fitted in Fig. 26 only takes the HST and VLT/NaCo measurements into account. Considering these two measurements, the background hypothesis can be rejected with $28.9\,\sigma$ in separation and with $2.9\,\sigma$ in PA. In separation, a small decline of ~5 mas between 1999.046 and 2009.751 is observed, which amounts to a yearly decline of 0.4 mas. However, this is not significant given the uncertainties of the two astrometric measurements. In PA, a decline of 0.89°

was observed between the two observation epochs. This amounts to a yearly decline of 0.083°. This decline is, in fact, highly significant with 3.4 σ. The HST PA measurement lies slightly outside of the area estimated for a circular face-on orbit. Given that there was no significant change in separation in the same timeframe, this could indicate that we are indeed observing the orbit close to face-on and that the orbit is eccentric with the companion close to peri- or apastron. Additional astrometric measurements are needed to confirm the observed trend and to constrain the orbital elements.

As pointed out in section 2.1.3, DH Tau is part of a wide binary system with the second star being DI Tau at a separation of 16 arcsec. The stability of such binary systems with a (sub)stellar companion was investigated by Holman and Wiegert (1999). They found that the orbit is stable if the semi-major axis of the companion orbit is less than one quarter of the binary separation, thus less than 4 arcsec in the case of DH Tau B. The orbit of DH Tau B should hence be stable. This was also pointed out by Itoh et al. (2005).
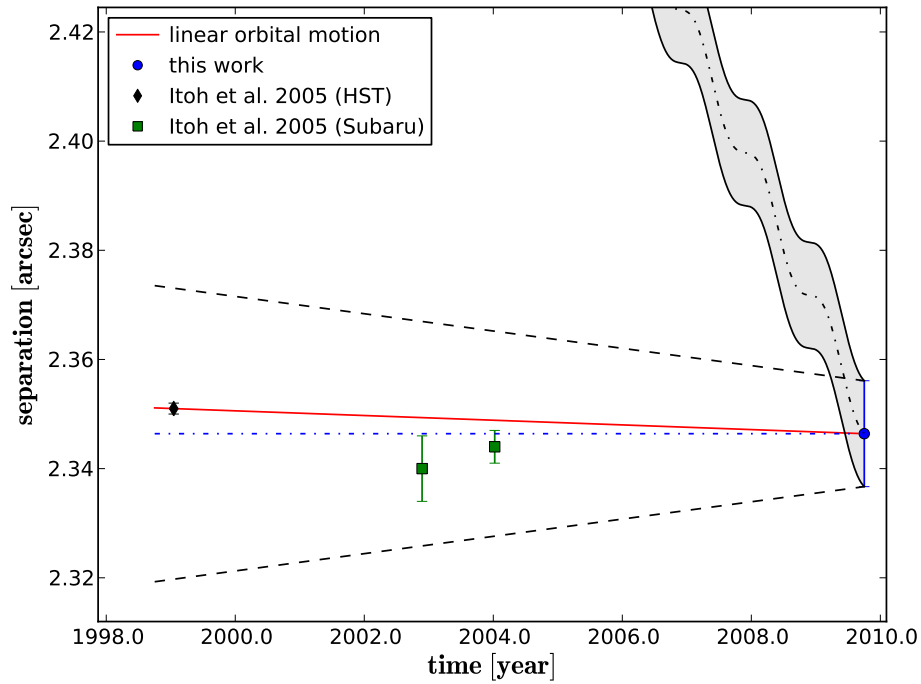
(a) Separation versus time
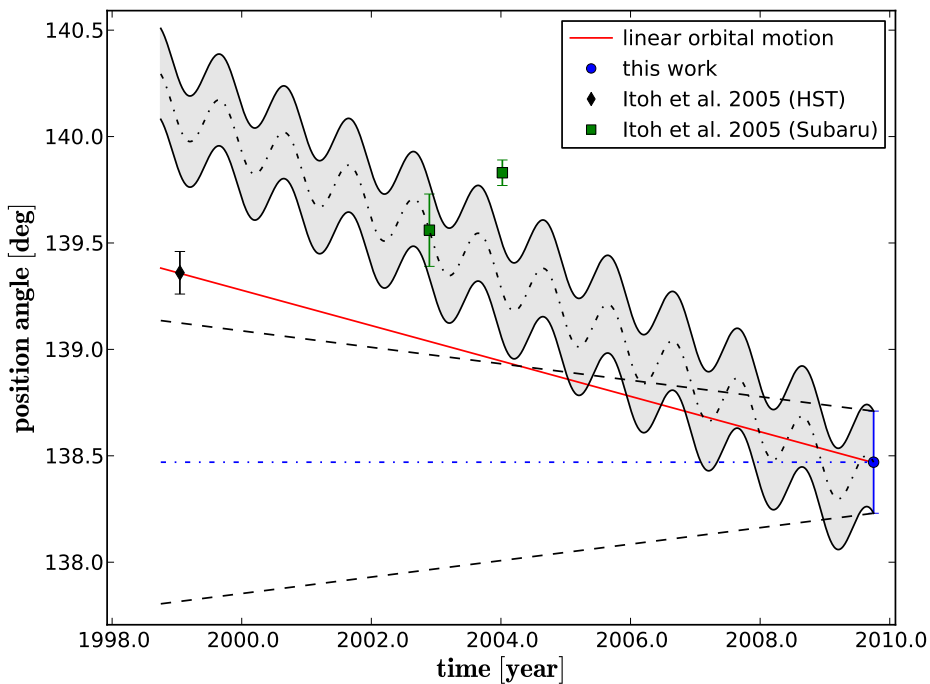
(b) PA versus time

Figure 26: Proper motion diagrams of the DH Tau system. Origin of the data points is indicated by color and shape.

5.1.4 GSC 08047-00232

The GSC 08047-00232 system has been observed several times since the discovery of the substellar companion GSC 08047-00232 B in mid-2001. Astrometric data points are avail-

able in Neuhäuser et al. (2003), Chauvin et al. (2003), Neuhäuser and Guenther (2004) and Chauvin et al. (2005).

Neuhäuser et al. (2003) observed the system on 2001 July 4 with NTT/SHARP I in the K-band. Their discovery image of the substellar companion was already shown in Fig. 8(a). They astrometrically calibrated the instrument with observations of the Galactic center executed in the same night and confirmed their calibration by observations of two wide stellar binaries. The resulting pixel scale of the instrument is given to be 49.1 mas/pixel. For the calculation of the uncertainty of their astrometric measurement, they considered a 10 % uncertainty of the pixel scale and a 15 % uncertainty of the image orientation as well as the uncertainty of the position measurement, which they attained by fitting a Gaussian to the star and companion positions.

The substellar companion was discovered parallel by Chauvin et al. (2003) using the ADO-NIS AO system and the SHARP II instrument at the ESO 3.6 m telescope on 2001 October 28. The discovery image is shown in Fig. 8(b). Astrometric calibration of their observation was achieved by observations of Θ Ori. They give a pixel scale of 49.6 ± 3 mas/pixel and a detector orientation of $0.56° \pm 0.5°$. The primary was located behind an opaque coronagraph during the observations and the companion was located in the diffraction spike of the star, both of which severely hamper the precision level achievable of the position measurements of both objects. Total astrometric uncertainty was calculated considering these measurement uncertainties in addition to the uncertainties of the astrometric solution.

Neuhäuser and Guenther (2004) observed the system again on 2003 July 20, utilizing VLT/ISAAC. They took near infrared spectra of the companion, but used the obtained aquisition image to measure separation and PA of the companion with respect to the primary. They calibrated the pixel scale of the instrument by measuring relative positions of stars visible in other aquisition images during that same night, but could not calibrate the detector orientation as there were no other stars visible in the aquisition image of the GSC 08047-00232 system itself and detector orientation was changing during the observations of different targets in service mode.

Finally, Chauvin et al. (2005) present three observations of the GSC 08047-00232 system, obtained with VLT/NaCo between 2002 November 23 and 2004 March 5. Observations were carried out in J and H-band as well as various narrow band filters with the S 13 objective. They used different astrometric calibrators in each observing epoch. In 2002 and 2004 they used Orion n and Θ Ori respectively, which are both part of the Orion Molecular Cloud Complex (Luhman et al. 2000). For their observation on 2003 September 7, they used the visual binary HD 211742. Between these three observations they calculated an average pixel scale of 13.24 ± 0.05 mas/pixel, which is in agreement with the pixel scale of 13.282 ± 0.054 as calculated in section 4.1 of this work for the VLT/NaCo observation epoch. Additionally, they calculated the detector orientation in each observing epoch. The results are chronologically: -0.05°, +0.05°, +0.04°, all with an uncertainty of 0.1°. Positions of primary and companion were measured by fitting a Gaussian to the respective

objects. Uncertainties of astrometric calibration and individual position measurements were considered for calculation of the total uncertainty of each data point.

All disscused literature data points, as well as the new VLT/NaCo measurement conducted in this work, are listed in Tab. 20. In addition, the proper motion diagrams for the system are shown in Fig. 27.

Table 20: Astrometric measurements of the GSC 08047-00232 system

Epoch [yr]	Sep [arcsec]	PA [°]	Reference
2001.508	3.238 ± 0.022	357.65 ± 0.18	Neuhäuser et al. (2003)
2001.828	3.210 ± 0.118	359.2 ± 2.3	Chauvin et al. (2003)
2002.896	3.274 ± 0.012	358.85 ± 0.23	Chauvin et al. (2005)
2003.552	3.138 ± 0.048	~ 358	Neuhäuser and Guenther (2004)
2003.686	3.266 ± 0.011	358.89 ± 0.23	Chauvin et al. (2005)
2004.178	3.260 ± 0.012	358.82 ± 0.22	Chauvin et al. (2005)
2009.702	3.232 ± 0.014	358.53 ± 0.24	this work

In general it can be assumed that the data points by Chauvin et al. (2005) should show only a small or no systematic offset towards the VLT/NaCo measurement of 2009.702, since the observations were taken with the same instrument and similar instrument settings and each epoch was calibrated astrometrically. As can be seen in Fig. 27(a), the separation is decreasing constantly between each of these measurements and also between these measurements and the VLT/NaCo measurement of 2009.702. The red line shown in this figure represents the linear fit of these four data points and shows a decline of 5.9 ± 0.7 mas/yr. However, this is currently only significant with $2.3\,\sigma$. The PA shown in Fig. 27(b) is consistent with a very small decline of $0.052° \pm 0.008°$, but only on the $1\,\sigma$ level, hence the PA is also consistent with no change. Given the low significance, it is in principle possible that the effect is caused by small systematic offsets between the four VLT/NaCo epochs, due to the fact that a different astrometric calibrator was used in each observing epoch. Different calibrators can lead to different astrometric solutions depending on how well the calibration source is understood, especially in the case of visual binaries. This was, among other things, demonstrated in section 4.1. It seems, however, unlikely that such uncorrelated offsets would produce the constant decline in separation that is observed.

The measurement by Chauvin et al. (2003) does not add further information due to its large uncertainties. It is in fact consistent with common proper motion, differential motion and background hypothesis in separation and only inconsistent with the background hypothesis on the $2\,\sigma$ level in PA. The data points by Neuhäuser et al. (2003) and Neuhäuser and Guenther (2004), however, are peculiar, as they seem to suggest a different behavior of the system.

The measurement of 2001.508 shows in separation no significant differential motion in comparison to the 2009.702 VLT/NaCo epoch. Furthermore, it clearly ($2.9\,\sigma$) shows dif-

ferential motion in PA with an increase of $0.88°$ ($0.11°$ per year). The measurement was carefully calibrated as explained above. It is nevertheless possible that the uncertainties of this measurement are underestimated. As can be seen in Fig. 8(a) the companion is very faint and lies within a faint diffraction spike of the primary. The diffraction spike contains more flux closer to the primary and fades out with growing distance. The primary PSF was not subtracted before the measurement of the companion position. In such a case, it would be expected that the separation measurement would yield a smaller separation than expected due to the flux contamination from the primary. Given the pixel scale of the instrument, a change in position of the companion by 0.5 pixel would already mean a change of separation of ~ 25 mas, i.e. the separation would then be consistent with the observed decline between the VLT/NaCo measurements. For the same reasons, the uncertainty of the PA measurement could be underestimated. Due to these concerns, the measurement by Neuhäuser et al. (2003) was not considered when calculating the possible differential motion.

The separation measurement by Neuhäuser and Guenther (2004) is neither consistent with the VLT/NaCo measurements nor with the measurement by Neuhäuser et al. (2003). It is not clear what causes this discrepancy. It was, however, decided that the NaCo measurements seem more trustworthy and hence this measurement was also not considered for any further calculations.

Considering only the VLT/NaCo measurements, the background hypothesis can be rejected with $1.9\,\sigma$ in separation and $10.8\,\sigma$ in PA. The measured differential motion would be consistent with either an edge-on circular orbit or with an eccentric orbit. In section 5.2.3 these measurements are used to further constrain the orbit of the system.
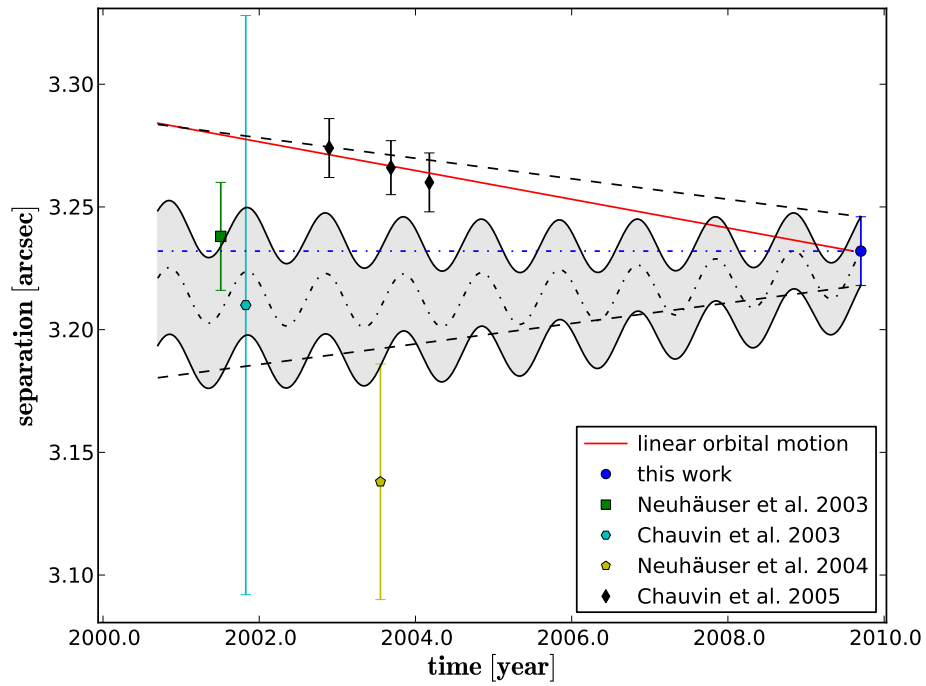
(a) Separation versus time
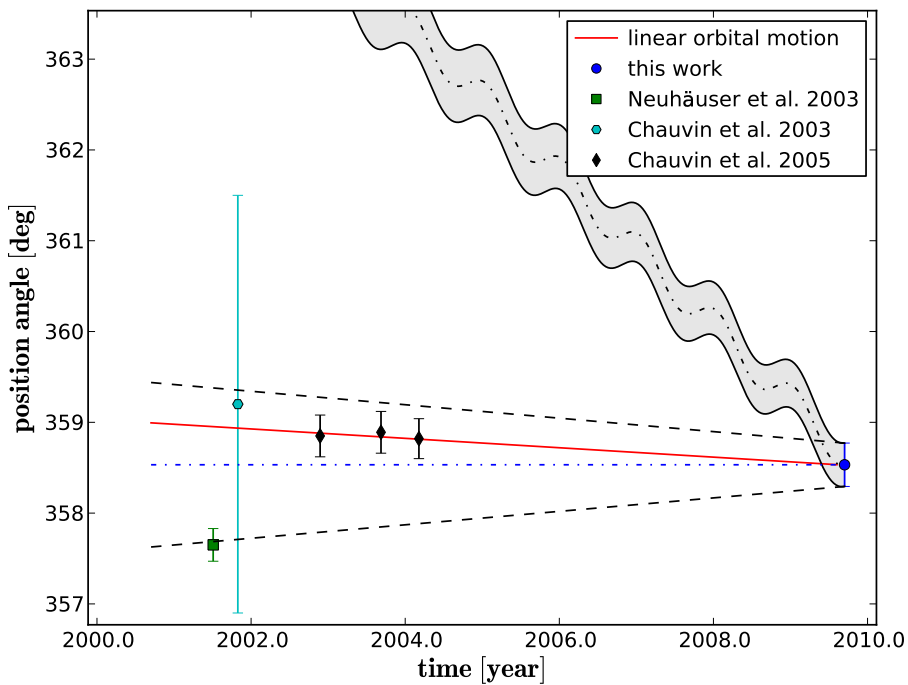
(b) PA versus time

Figure 27: Proper motion diagrams of the GSC 08047-00232 system. Origin of the data points is indicated by color and shape.

5.1.5 1RXS J160929.1-210524

In addition to the VLT/NaCo observation presented in section 4.1, there were astrometric data points of the 1RXS J160929.1-210524 system available in publications by Lafrenière et al. (2010) and Ireland et al. (2011).

Lafrenière et al. (2010) present astrometric measurements obtained with the Gemini-North Telescope and the NIRI instrument in combination with the ALTAIR AO system. The observations were executed between early 2008 and mid-2009. All data points are listed in Tab. 21. They did not observe any astrometric calibrators and could hence only use the stored header information for pixel scale and detector orientation. They also note that the pixel scale of 21.4 mas/pixel that they used is not well calibrated in their choosen observation mode with the ALTAIR field lens in place (see also the ALTAIR instrument webpage[7]). However, in all of the Gemini-North observations, six background stars were present in the field of view. Separation and PA of these background stars with respect to 1RXS J160929.1-210524 A were monitored throughout the different observation epochs and compared with the predicted values, given the proper motion of 1RXS J160929.1-210524 A. While the pixel scale and orientation can not be absolutely calibrated this way, its is possible to monitor changes between the observing epochs. The maximum changes that were measured by Lafrenière et al. (2010) correspond to 6 mas in separation and 0.1° in PA, hence these values were adopted by the authors as the maximum uncertainties of their astrometric measurements.

Ireland et al. (2011) observed the 1RXS J160929.1-210524 system with the Keck 10 m telescope and the NIRC2 instrument. Their two data points taken mid-2008 and mid-2009 are listed in Tab. 21. They do not report any astrometric calibrators imaged, but rather use the astrometric solution of the instrument as provided by Ghez et al. (2008). They therein report a pixel scale of 9.963 ± 0.005 mas/pixel and a detector orientation of $0.13° \pm 0.02°$ as calculated by their high precision observations of the galactic center. These calibration observations were conducted between mid-2005 and late 2007. The astrometric solution was, in this timeframe, stable within the given uncertainties. The total uncertainties of the astrometric measurements by Ireland et al. (2011) include the uncertainties of the astrometric solution and the standard deviation of multiple position measurements, both added in quadrature. However, they neglected the actual uncertainty of each individual position measurement, which was most likely significantly larger than the standard deviation of multiple measurements.

The corresponding proper motion diagrams to the data points listed in Tab. 21 are shown in Fig. 28. In both separation and PA there is a significant offset between between the datasets of Lafrenière et al. (2010) and Ireland et al. (2011). Given the observations of 2008.460 and 2008.462, which were conducted on consecutive nights where one can assume

---

[7]http://www.gemini.edu/sciops/instruments/altair/field-lens-option

Table 21: Astrometric measurements of the 1RXS J160929.1-210524 system

Epoch [yr]	Sep [arcsec]	PA [°]	Reference
2008.321	2.215 ± 0.006	27.75 ± 0.10	Lafrenière et al. (2010)
2008.460	2.221 ± 0.006	27.76 ± 0.10	Lafrenière et al. (2010)
2008.462	2.2101 ± 0.001	27.62 ± 0.04	Ireland et al. (2011)
2009.262	2.222 ± 0.006	27.65 ± 0.10	Lafrenière et al. (2010)
2009.415	2.2113 ± 0.0009	27.61 ± 0.05	Ireland et al. (2011)
2009.497	2.219 ± 0.006	27.74 ± 0.10	Lafrenière et al. (2010)
2009.623	2.2062 ± 0.0056	27.25 ± 0.22	this work

that separation and PA of the companion with respect to the primary have not changed, the systematic offset in separation is in the order of $\sim$11 mas and the offset in PA is in the order of $\sim$0.14°. Furthermore, both datasets seem to show a systematic offset towards the 2009.623 VLT/NaCo measurement presented in this work. The significant differences, especially in PA, when comparing this measurement to the 2009.497 measurement of Lafrenière et al. (2010) and the 2009.415 measurement of Ireland et al. (2011) (0.49° and 0.36° respectively), are most likely caused by systematic offsets rather than differential proper motion, given the very short time difference of only a few months.

Systematic offsets between the two literature datasets could be caused by the essentially uncalibrated astrometric solution used by Lafrenière et al. (2010) as already discussed. In addition, the astrometric solution used by Ireland et al. (2011) was computed more than one year before the science epochs. Although this solution was stable over a timeframe of several years beforehand, there is always the possibility of a glitch in the system causing the solution to change, even more so if there was some maintenance work done on the detector or the AO system between 2007 and mid-2008. Furthermore, given the experiences briefly discussed in section 4.3.1, the individual measurement errors in one image frame can be as much as ten times as large as the standard deviation of measurements in multiple image frames as considered by Ireland et al. (2011) for the total astrometric uncertainty of their measurements. Hence it seems likely that these uncertainties are underestimated. Larger uncertainties of these data points would put them in better agreement with the data points by Lafrenière et al. (2010) and the VLT/NaCo measurement.

Given the discussed difficulties, it is not applicable to compare the two literature datasets, or each of the literature datasets individually with the VLT/NaCo measurement to derive a potential differential motion between primary and companion. It is, however, possible to compare the data points within each literature dataset independently since there should be neglegible systematic effects between measurements done with the same instrument settings and astrometric calibrations. The result shows for neither of the two datasets a significant ($>1\,\sigma$) differential motion in the covered timeframe. The largest change can be observed between the two measurements of Ireland et al. (2011) in separation, with an increase of 0.012 arcsec and a corresponding significance of $0.92\,\sigma$. This significance decreases drasti-

cally if the measurement uncertainties are underestimated as suspected. Hence it is very questionable whether or not this is a real effect.

Given the proper motion of the primary, which is generally in the direction of the companion, the separation between the two objects should decrease while the PA should stay approximately the same (save parallactic changes), if the companion would be a background object (as indicated by the grey area in Fig. 28). Considering the discussed systematic offsets between the different datasets, a prediction of the significance level on which the background hypothesis can be rejected would be very unreliable in PA, with only minimal differences between real companions and background objects. In separation, the effect of the primary's proper motion on a background object is, however, much stronger. If the VLT/NaCo measurement and the first measurement of 2008.321 are taken into account, the background hypothesis can be rejected with $4.28\,\sigma$. Even given the discussed systematic offsets, this should place the significance level with which the background hypothesis can be rejected well above $3\,\sigma$. Hence, it can be confirmed that primary and companion share a common proper motion and are thus most likely orbiting each other, although no orbital motion can be detected yet.
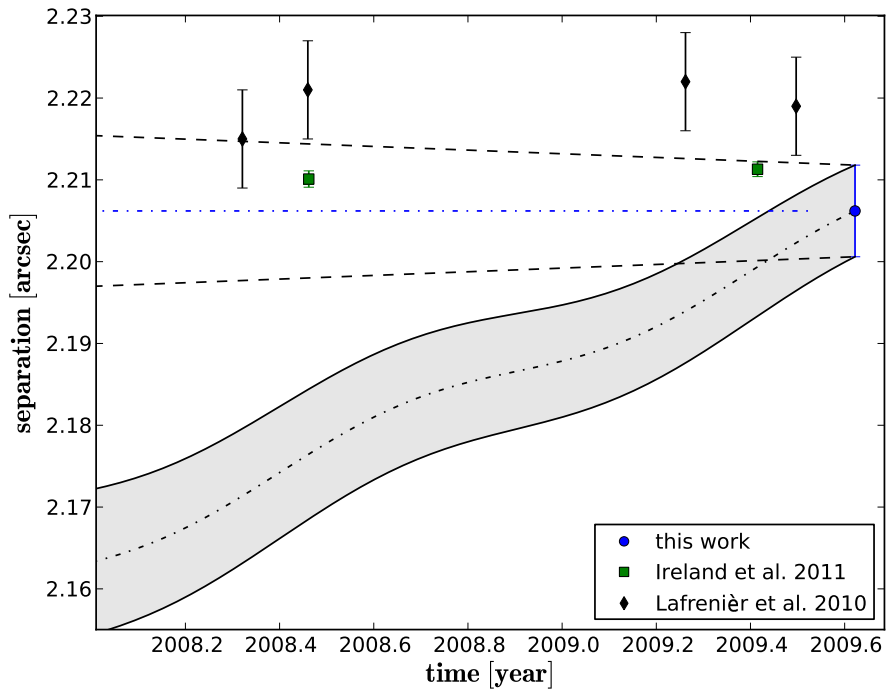
(a) Separation versus time
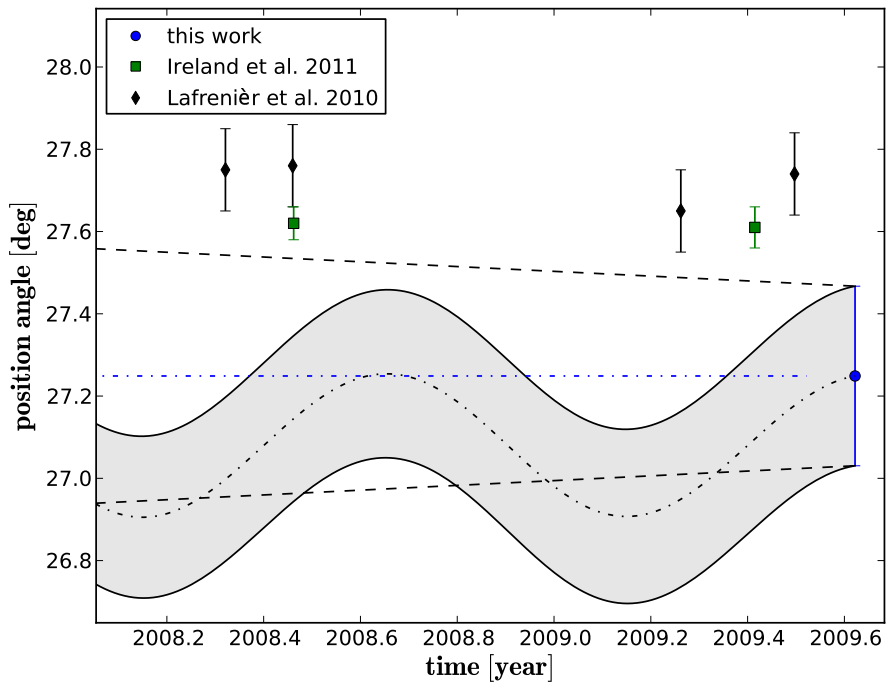
(b) PA versus time

Figure 28: Proper motion diagrams of the 1RXS J160929.1-210524 system. Origin of data points is indicated by color and shape.

5.1.6 UScoCTIO 108

There is only one astrometric data point of UScoCTIO 108 A and B available in the literature. Béjar et al. (2008) measured the separation and PA in their observations with the IAC (**I**nstituto de **A**strofísica de **C**anarias) 80 cm telescope in the I-band on 2007 July 05. They used a pixel scale of 0.305 arcsec/pixel, but did not provide any information on the astrometric calibration of their observations. Their result is listed in Tab. 22 alongside the VLT/NaCo measurement as discussed in section 4.1.

Table 22: Astrometric measurements of the UScoCTIO 108 system

Epoch [yr]	Sep [arcsec]	PA [°]	Reference
2007.511	4.6 ± 0.1	177 ± 1	Béjar et al. (2008)
2009.623	4.579 ± 0.015	176.96 ± 0.27	this work

In Fig. 29 both data points are plotted in proper motion diagrams. The VLT/NaCo measurement is approximately ten times more precise in separation and 4 times more precise in PA, and is hence the most precise astrometric measurement of these two objects to date. Due to the large uncertainty of the first astrometric measurement, and the proper motion of the primary (-8±14 mas/yr and -17±13 in R.A. and Dec repectively, see section 2.1.6), the background hypothesis can not yet be rejected with any significance. Given the precision level of the VLT/NaCo measurement, a similar measurement would be needed in ~ 9 yr to reject the background hypothesis in separation with $>1\,\sigma$. Another possibility would be to refine the proper motion of the primary star. This could be done by taking a wide field image of the primary with e.g. NTT/SofI (Moorwood et al. 1998) and comparing separations and PAs of the stars in the field with respect to the primary with e.g. 2MASS. It is not possible to detect any orbital motion of UScoCTIO 108 B around A, for the same reason that the background hypothesis can not yet be rejected. Furthermore, Béjar et al. (2008) calculated that the escape velocity of this alleged wide low-mass binary would only be 0.4 km/s. Given the projected separation of $\sim$670 AU, and assuming a face-on orbit, this means that the orbital motion in PA should be smaller than 10^{-5} °/yr. Considering the uncertainties of the VLT/NaCo measurement, it would take $\sim$47000 yr to detect orbital motion on the $1\,\sigma$ level. Similar considerations for an edge-on orbit yield a time baseline of $\sim$35000 yr for an analog detection in separation.

(a) Separation versus time
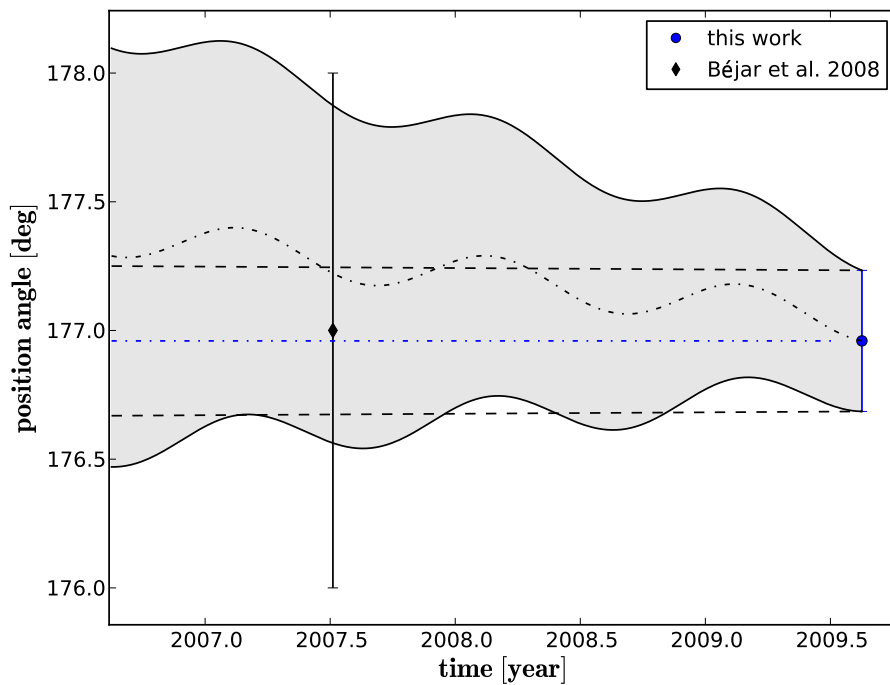
(b) PA versus time

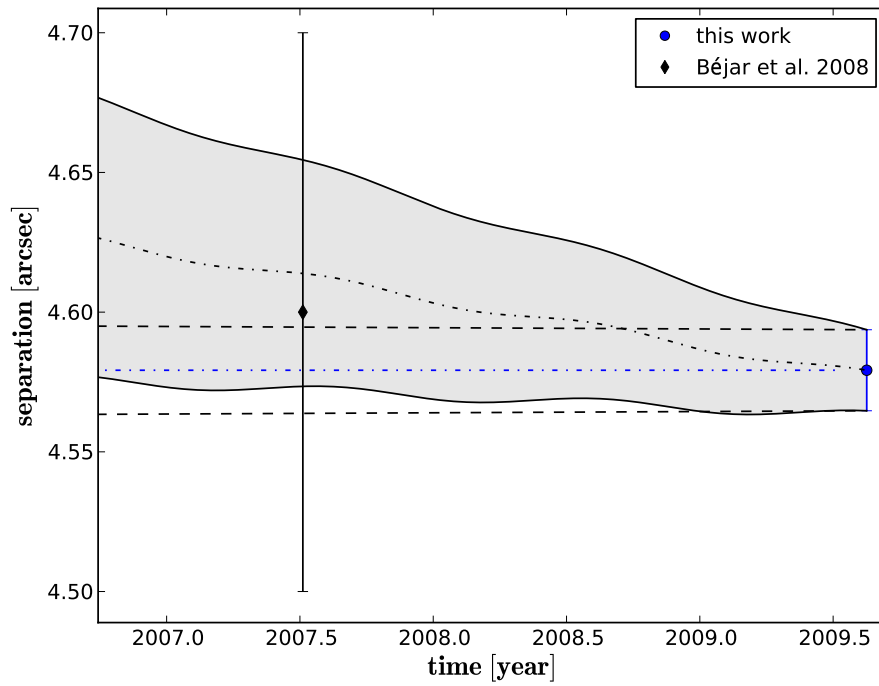Figure 29: Proper motion diagrams of the UScoCTIO 108 system. Origin of data points is indicated by color and shape.

5.2   Orbit fitting

5.2.1   Least Squares Monte Carlo Approach

Every attempt to determine the orbit of directly imaged substellar companions faces the major problem that the coverage of the orbit with astrometric data points is typically in the order of a few percent or less. Additionally, the seven Keplerian orbit elements span a large parameter space. This must be considered when attempting to find good orbit solutions.

A combined Least Squares Monte Carlo (LSMC) approach was developed to deal with these problems. The Monte Carlo method has the advantage of sampling large areas of the parameter space, while the least squares method is a good choice to find local minima. As a result, a set of possible solutions is derived that provide a statistical global overview over the minima of the parameter space. This is especially useful if there is a multitude of equally good minima due to the poor coverage of the orbit with astrometric data points. Even if there is no single best orbit solution, the resulting distribution of solutions enables us to put constraints on the orbital elements.

The SciPy Python library (Jones et al. 2001) was used to create the LSMC fitting algorithm. SciPy is a general purpose library for scientific computations and engineering. Within SciPy the `leastsq` function is provided, which minimizes the sum of squares of a given set of equations, using a modified Levenberg-Marquardt (Levenberg 1944) algorithm. A function was written as input for `leastsq` that computes the weighted difference between an input model orbit and the astrometric data points. The uncertainties of the astrometric measurements were used for weighting, so that more precise data points have a higher influence on the resulting difference than less precise ones. Boundary conditions were implemented, to ensure that no non-physical solutions (e.g. a negative semi-major axis) are persued.

The "first guess" orbital elements for the least squares fit are drawn from a random uniform distribution. A uniform distribution was choosen because we usually do not have knowledge of the distribution of the individual orbital elements. To constrain the parameter space, reasonable boundary conditions were set, e.g. the semi-major axis should not be larger than the largest separation between primary and companion for which the system is still stable. Furthermore, we fixed the total mass of the system to the mass of the primary star plus the estimated mass for the substellar companion, and thereby tied the orbit period to the semi-major axis by Kepler's third law, thus reducing the number of free parameters to 6.

To calculate the orbit from the orbital elements, first the orbital period P is calculated from the total system mass M_{total} and the semi-major axis a:

$$P = 2\pi \sqrt{\frac{a^3}{GM_{total}}} \ ,$$

wherein G is the gravitational[8] constant. In the next step, the Thiele-Innes elements of the orbit $(A, B, F, G$, see e.g. Alzner 2004) are calculated from the semi-major axis, the argument of the periastron ω, the longitude of the ascending node Ω and the inclination of the orbit i:

$$
\begin{aligned}
A &= a(\cos\omega \cos\Omega - \sin\omega \sin\Omega \cos i) \\
B &= a(\cos\omega \sin\Omega + \sin\omega \cos\Omega \cos i) \\
F &= a(-\sin\omega \cos\Omega - \cos\omega \sin\Omega \cos i) \\
G &= a(-\sin\omega \sin\Omega + \cos\omega \cos\Omega \cos i) \ .
\end{aligned}
$$

Subsequently, the mean anomaly $\mathcal{M}$ of the orbit is calculated for all points in time t for which astrometric measurements are available. The mean anomaly connects time and place in Keplerian orbits and increases linearly from 0 to 2π starting at the periastron of the orbit. It is calculated from the time of the last periastron passage T_0 and the orbital period:

$$
\mathcal{M} = \frac{(t - T_0)2\pi}{P} \ .
$$

With the mean anomaly the eccentric anomaly $\mathcal{E}$ is calculated by means of the Kepler equation:

$$
\mathcal{M} = \mathcal{E} - e\sin\mathcal{E} \ .
$$

The Kepler equation is a transcendental equation, which means it can only be solved numerically. A geometric description of the eccentric anomaly is given in Fig. 30. To solve the Kepler equation Newton's method was used as given e.g. in Montenbruck (2005):

$$
\mathcal{E}_{n+1} = \mathcal{E}_n + \frac{\mathcal{M} - \mathcal{E}_n + e\sin\mathcal{E}_n}{1 - e\cos\mathcal{E}_n} \ .
$$

Figure 30: The eccentric anomaly $\mathcal{E}$ is an angular value that relates the position of an orbiting body on an elliptical orbit to the positions on two auxilliary circles with the radii a and b, which are equivalent to the semi-major and semi-minor axis of the orbit ellipse. $\mathcal{E}$ is measured from the center of the ellipse C. If $\mathcal{E}$ is known at a given time, the place of an object on an orbit of known properties can be calculated.

The first approximation was taken from Alzner (2004):

$$
\mathcal{E}_0 = \mathcal{M} + e\sin\mathcal{M} + \frac{e^2 \sin 2\mathcal{M}}{\mathcal{M}} \ .
$$

---

[8]$G = 6.67384(80) \cdot 10^{-11} \, m^3 kg^{-1} s^{-2}$

Iterations continue until the change between two subsequent iteration steps is neglible $|\mathcal{E}_n - \mathcal{E}_{n+1}| < 10^{-5}$, or for a maximum of 50 iterations. Finally, the Kartesian coordinates of the companion with respect to the primary are computed by utilizing the eccentric anomaly, the eccentricity of the orbit and the Thiele-Innes elements (see, e.g. Alzner 2004):

$$
\begin{aligned}
x &= A(\cos \mathcal{E} - e) + F(\sqrt{1 - e^2} - \sin \mathcal{E}) \\
y &= B(\cos \mathcal{E} - e) + G(\sqrt{1 - e^2} - \sin \mathcal{E}) \ .
\end{aligned}
$$

Each LSMC run in this work consits of 1,000,000 individual least square fits with random starting conditions as described. One run takes approximatly 18 hours to complete. All orbit solutions and the associated χ^2 values are saved for later evaluation and the orbit with the lowest χ^2 is returned. The source code for all essential functions for the LSMC orbit fit is provided in appendix A.3.

For evaluation of the resulting distributions of orbital elements, histograms and cross-correlation diagrams are plotted using the MATPLOTLIB PYTHON library (Hunter 2007).

For future optimizations, the PYTHON threading capabilities can be utilized to parallelize the LSMC fitting routine, resulting in significantly shorter computation times.

5.2.2   Orbital Parameters of HD 130948 ABC

To fit the orbit of the BC binary around HD 130948 A, the previously discussed Least Squares Monte Carlo (LSMC) approach was used. Only the *calibrated* data points were considered for the orbit fit and a total of 1,000,000 runs were performed.

To narrow the parameter space, some constraints were made to the starting distribution. The total system mass was set to $1 \, M_\odot$ for the A component (G1V) plus $0.11 \, M_\odot$ for the B and C component as determined by Dupuy et al. (2009). The orbit period was then tied to the semi-major axis by Kepler's third law. The semi-major axis was also constrained to an upper limit of 61.1 arcsec. This upper limit corresponds, at the distance of the system, to a projected separation of ~ 1110 AU, which according to Close et al. (2003) ($a_{max}[AU] = 1000 \cdot M_{total}/M_\odot$) corresponds to the maximum semi-major axis at which the system is still long-term stable against disruption in the galactic disk. In addition, the longitude of the ascending node was constrained to values smaller than $180°$, since no precise radial velocity measurements of the system are available.

In Fig. 31 semi-major axis versus eccentricity is shown for the best $\sim 7\%$ orbit solutions corresponding to χ^2_{red} between 5.6 and 6.2. These relatively high values are most likely introduced by small systematic offsets between the astrometric measurements due to the usage of different instruments and astrometric calibrators. The solutions can be further constrained with considerations about the system dynamics. Since even the largest possible
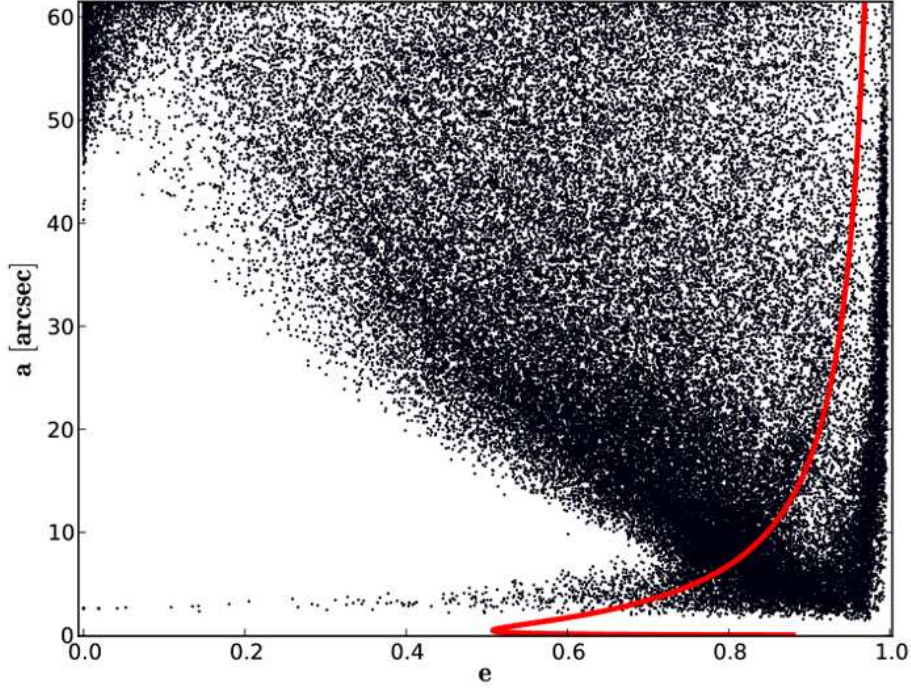
Figure 31: Semi-major axis as function of eccentricity for the top ten percent best fitting solutions out of 1,000,000 LSMC runs. The solid line marks the critical eccentricity for each semi-major axis at which the BC system becomes not Hill stable due to close encounters with the primary star. All solutions to the right are unstable and can therefore be ruled out. The critical eccentricity was calculated by the formula given in Donnison (2010).

orbital periods of several thousand years are much smaller than the system age, it can be concluded that the BC binary system is Hill stable. Donnison (2010) gives the critical stable eccentricity e_{crit} of such binary systems around their central star as a function of the binary eccentricity e_{bin}, the semi-major axis a_1 of the BC and the BC around A system a_2, as well as the binary mass ratio λ and the inclination of the binary orbit i relative to the orbit of the binary around the central star.

$$e_{crit} = \left\{ 1 - \left[\left(\left\{ \frac{3\lambda^2 \frac{a_1}{a_2}(1 - e_{bin}^2)x^3 \cos^2 i}{\left\{(1+\lambda)^2(1-3x^3) + 3\lambda\frac{a_2}{a_1}x^3\right\}^2} - \frac{\frac{3\lambda^2}{(1+\lambda)}\frac{a_1}{a_2}(1 - e_{bin}^2) - (1+\lambda)^3}{(1+\lambda)\left\{(1+\lambda)^2(1-3x^3) + 3\lambda\frac{a_2}{a_1}x^3\right\}} \right. \right. \right. \right.$$
$$- \frac{9\lambda(\lambda+1)x^2 + (2\lambda(\lambda-1) - 3(1+\lambda)^3)x^3 + \left(\lambda(2+5\lambda) + \frac{12\lambda^2}{(1+\lambda)} + \frac{9\lambda(1+\lambda^2)}{(1+\lambda)^2}\right)x^4}{(1+\lambda)\left\{(1+\lambda)^2(1-3x^3) + 3\lambda\frac{a_2}{a_1}x^3\right\}}$$
$$\left. \left. \left. \left. - \frac{\sqrt{3}\lambda\frac{a_1}{a_2}^{1/2}(1 - e_{bin}^2)^{1/2}x^{3/2}\cos i}{\left\{(1+\lambda)^2(1-3x^3) + 3\lambda\frac{a_2}{a_1}x^3\right\}} \right)^{1/2} \right)^2 \right]^{1/2} \right\}$$

With $x = ((M_1 + M_2)/3M_{star})^{1/3}$. In this case a mass ratio of 1 (Dupuy et al. 2009), and a relative inclination of 0 was applied, since the average inclination of the shown LSMC

fitting results in Fig. 31 for the orbit of BC around A ($99.2° \pm 8.2°$) is, within its uncertainties, consistent with the inclination of $i = 95.7°^{+0.3}_{-0.2}$ computed by Dupuy et al. (2009) for the BC system. In addition, small changes in relative inclination in the order of a few degrees do not influence the computation result significantly. The solid line in Fig. 31 marks the critical eccentricity at which the BC system would become unstable and the B and C component would split up to follow individual orbits around HD 130948 A. Through these considerations, all extremely eccentric orbits with $e > 0.96$, as well as most solutions with a semi-major axis of $a < 10$ arcsec can be excluded.

The results of the constrained LSMC run are listed in Fig. 32. Shown are the top five percent best-fitting Hill-stable solutions out of 1,000,000 runs. As can be seen in Fig. 32(a), the semi-major axis cannot be constrained with an LSMC run, but good solutions are obtained between 2.18 arcsec and 61.1 arcsec, which corresponds to orbital periods from a few hundred years up to ~ 35100 yr. It should, however, be noted that 99.1 % of the solutions have a semi-major axis larger than 5 arcsec and 93.6 % have a semi-major axis larger than 10 arcsec. It is therefore probable that the semi-major axis of the orbit is above these values. The majority (57.2 %) of the best-fitting orbit solutions are also highly eccentric ($e > 0.6$), as shown in Fig. 32(b). The angular elements of the orbit can be constrained more precisely. For the best runs, an inclination between 90.7° and 100.7° and a longitude of the ascending node between 95.8° and 172.3° are obtained, with a peak at 140.3°. For the argument of the periastron, in 91.3 % of the cases, solutions between 200° and 325° are calculated.

The time of the periastron passage shows a large spread and thus cannot be constrained, with the one exception that there exist only very few Hill-stable solutions that put the time of the periastron passage in the timeframe of the astrometric measurements.

The top five percent of Hill-stable solutions are shown in Fig. 33 as functions of eccentricity. Fig. 33(a) shows that nearly all solutions with a semi-major axis smaller than 10 arcsec have an eccentricity larger than 0.6, with a strong peak at ~ 8.4 arcsec and an eccentricity of ~ 0.8. This is no longer true for larger semi-major axes whose spread in eccentricity generally increases. Above a semi-major axis of ~ 45 arcsec, the solutions are distributed relatively evenly between 0.1 and 0.96. For an even larger semi-major axis between ~ 50 arcsec and ~ 60 arcsec, most of the solutions have a small eccentricity close to zero. At the same time these solutions show an inclination between $\sim 91°$ and $\sim 92°$.

Fig. 33(b) shows inclination versus eccentricity. The spread in inclination is increasing towards higher eccentricities. For eccentricities between 0 and 0.6, the orbit is seen almost edge-on with inclinations between 90.7° and 94°. Fig. 33(e) and Fig. 33(c) show the longitude of the ascending node Ω and the argument of the periastron ω versus eccentricity, repectively. While Ω follows the general trend of a higher scatter towards higher eccentricities, the soultions for ω have a large range at low eccentricities of up to 0.2, and a high density of solutions between 260° and 295° for high eccentricities between 0.69 and 0.81. Solutions with eccentricities above ~ 0.84 and up to 0.96 are split between two ranges for

Figure 32: Results of the LSMC fits to the astrometric data points. Shown are the distributions of the orbital elements of HD 130948 BC around A for the top five percent best fitting Hill-stable solutions out of 1,000,000 runs. The data has been sorted in 200 bins in each diagram.

ω. There are good solutions between $\sim 215°$ and $\sim 260°$ and $\sim 285°$ and $\sim 325°$.

A summary of the probable values of all orbital elements is shown in Tab. 23. In addition, the three best-fitting orbits are shown in Fig. 34 and the corresponding orbital elements are shown in Tab. 24.

Table 23: Most probable range and peak of orbital elements of the best fit Hill stable orbits

Parameter		Range	Peak
Semi-major Axis	a [arcsec]	2.2 - 61.1	-
	a [AU]	40 - 1110	-
Eccentricity	e	0 - 0.97	0 / 0.74
Orbital Period	P [yr]	237.4 - 35107.5	-
Inclination	i [deg]	90.7 - 100.7	91.8
Long. of Asc. Node	Ω [deg]	95.8 - 172.3	140.3
Arg. of Periastron	ω [deg]	1.1 - 359.5	233.2
Periastron Passage	T_0 [yr]	-19120 - 19120	5994
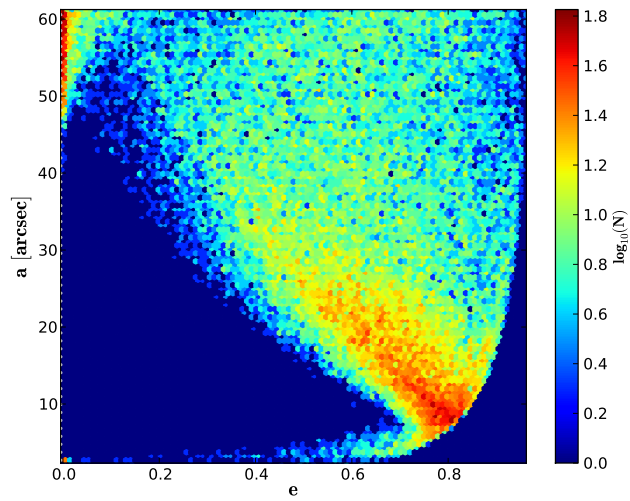
(a)
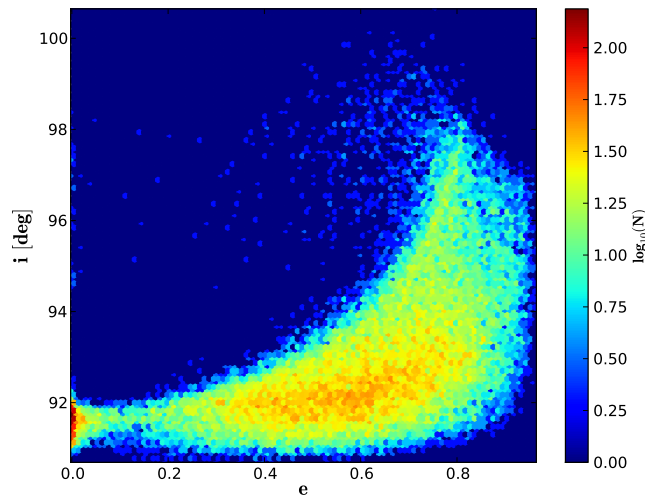
(b)
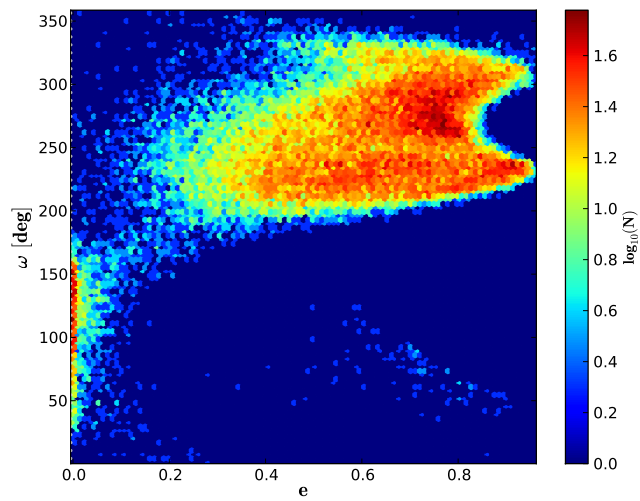
(c)
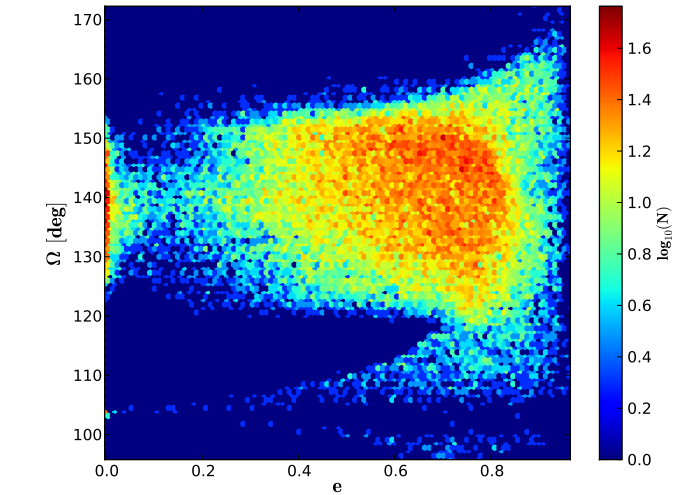
(e)
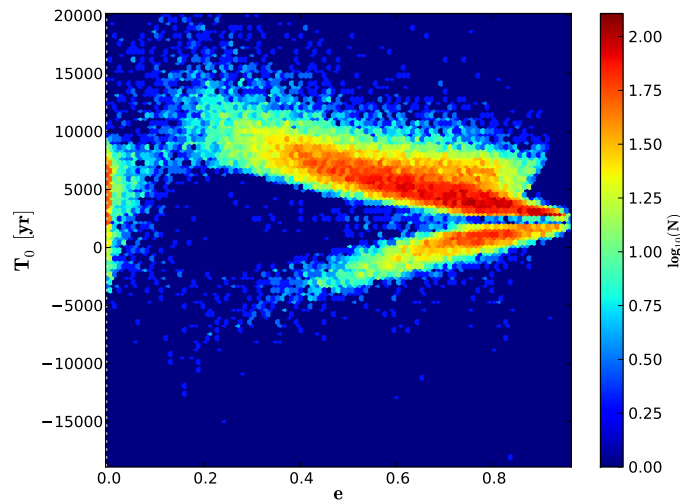
(f)

Figure 33: Orbital elements of HD 130948 BC around A as function of eccentricity for the top five percent best fitting Hill-stable solutions out of 1,000,000 runs of the LSMC fit. Logarithmic density of solutions is indicated by color.

(a)   (b)
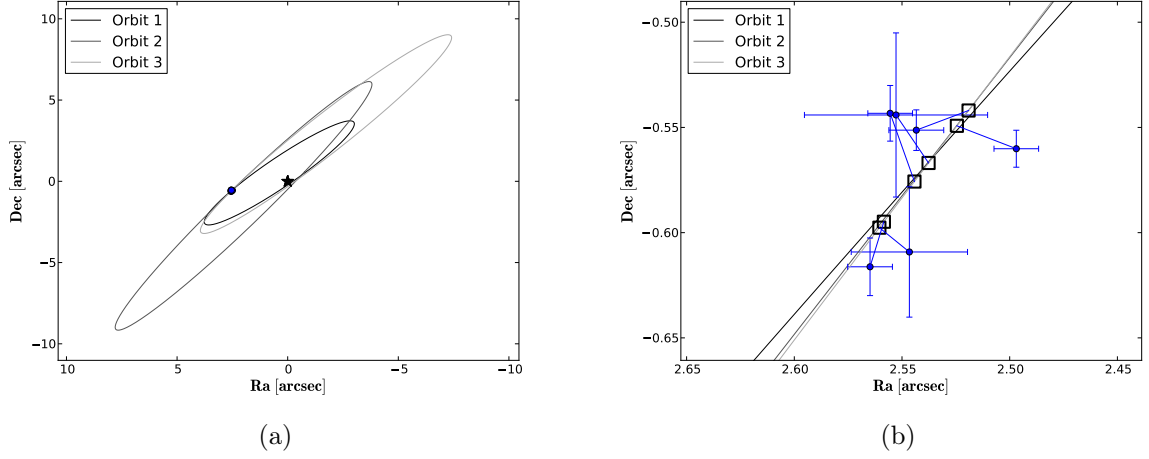
Figure 34: Top 3 best fitting Hill-stable orbits out of 1,000,000 runs of the LSMC fit.
Solid lines represent the apparent orbits. 34(b) is zoomed in on the data points. The
corresponding orbital elements are listed in Tab. 24

Table 24: Orbital elements and χ^2_{red} of the best fit orbits shown in Fig. 34

Nr.	1	2	3
a [arcsec]	7.6	13.4	12.5
e	0.80	0.73	0.79
P [yr]	1539.7	3622.3	3254.4
i [deg]	96.0	94.4	95.1
Ω [deg]	133.1	144.1	134.9
ω [deg]	270.7	255.8	289.2
T_0 [JD]	3383909.8	8264140.9	3425987.5
χ^2_{red}	5.6	5.6	5.6

5.2.3   Orbital Parameters of GSC 08047-00232 AB

The VLT/NaCo data point of this work as well as the data points by Chauvin et al. (2005) were utilized as input for the LSMC fitting algorithm. The total system mass was set to 0.88 $M_\odot$ (0.85 $M_\odot$ for the primary and 0.03 $M_\odot$ for the companion, see the mean values as given by Chauvin et al. 2003 in section 2.1.4). As was done in the case of HD 130948 BC around A, the upper limit of the semi-major axis was constrained by the long-term stability of the system against disruption in the galactic disk ($a_{max}[AU] = 1000 \cdot M_{total}/M_\odot$, Close et al. 2003). In the case of GSC 08047-00232 B around A this gives a maximum semi-major axis of 880 AU, which corresponds to 10.3 arcsec at 85 pc. The longitude of the ascending node was also constrained to values smaller than 180°, since there are again no precise radial velocity measurements of the system available.

The results of the LSMC fitting are shown in Fig. 35. All solutions with a $\chi^2_{red} < 2$ are included. The semi-major axis of the system could not be restrained in a meaningful way by the LSMC fitting program, due to the small coverage of the orbit. Good solutions are found between 2.36 arcsec and 10.3 arcsec, corresponding to 200 AU and 880 AU at the distance of the system. Subsequently, orbital periods between 3031.8 yr and 27629.8 yr are found. In the best case scenario of the shortest orbit found in the LSMC fitting, the total coverage of the orbit is only 0.2 %. The situation is better in the case of the eccentricity and the angular orbital elements. Good solutions were only found for eccentricities larger than 0.26, with an increasing number of solutions towards higher eccentricities. This is not entirely surprising, since there is only a linear change of separation observed at this point, which can be more easily fitted by highly eccentric orbits rather than circular orbits. For the inclination, only very few good solutions are found below a value of $\sim 100°$. In fact, 97.5 % of all good solutions lie above this value, with a strong and narrow peak at 180° and weaker and broader peak at 113°. The longitude of the ascending node can take all values between 0° and 180°, but has a strong peak at 10.4°. A total of 71.9 % of all good solutions for this parameter are between the values of 0° and 30°. The argument of the periastron can also in principle take almost all possible values between 0.3° and 359.6°, but 72.7 % of all included solutions lie between values of 100° and 200°, with a strong peak at 146.7°. The time of the periastron passage shows a large range of possible solutions, but has a strong peak as well. Many solutions show a periastron passage around the year 2511. The range and peak values of all orbital parameters are summarized in Tab. 25.

In Fig. 36 the derived orbital parameters are shown as functions of the eccentricity. In general, the spread in semi-major axis is increasing with eccentricity, as can be seen in Fig. 36(a). For small semi-major axis up to ~ 3 arcsec, only orbits with large eccentricities above ~ 0.65 are viable. For smaller eccentricities of 0.3 and 0.4, the semi-major axis can only take values between 5 arcsec and 6 arcsec, and 4 arcsec and 8 arcsec respectively. For an eccentricity of 0.9, good solutions were found for the full reported range of semi-major axes between 2.36 arcsec and 10.3 arcsec.
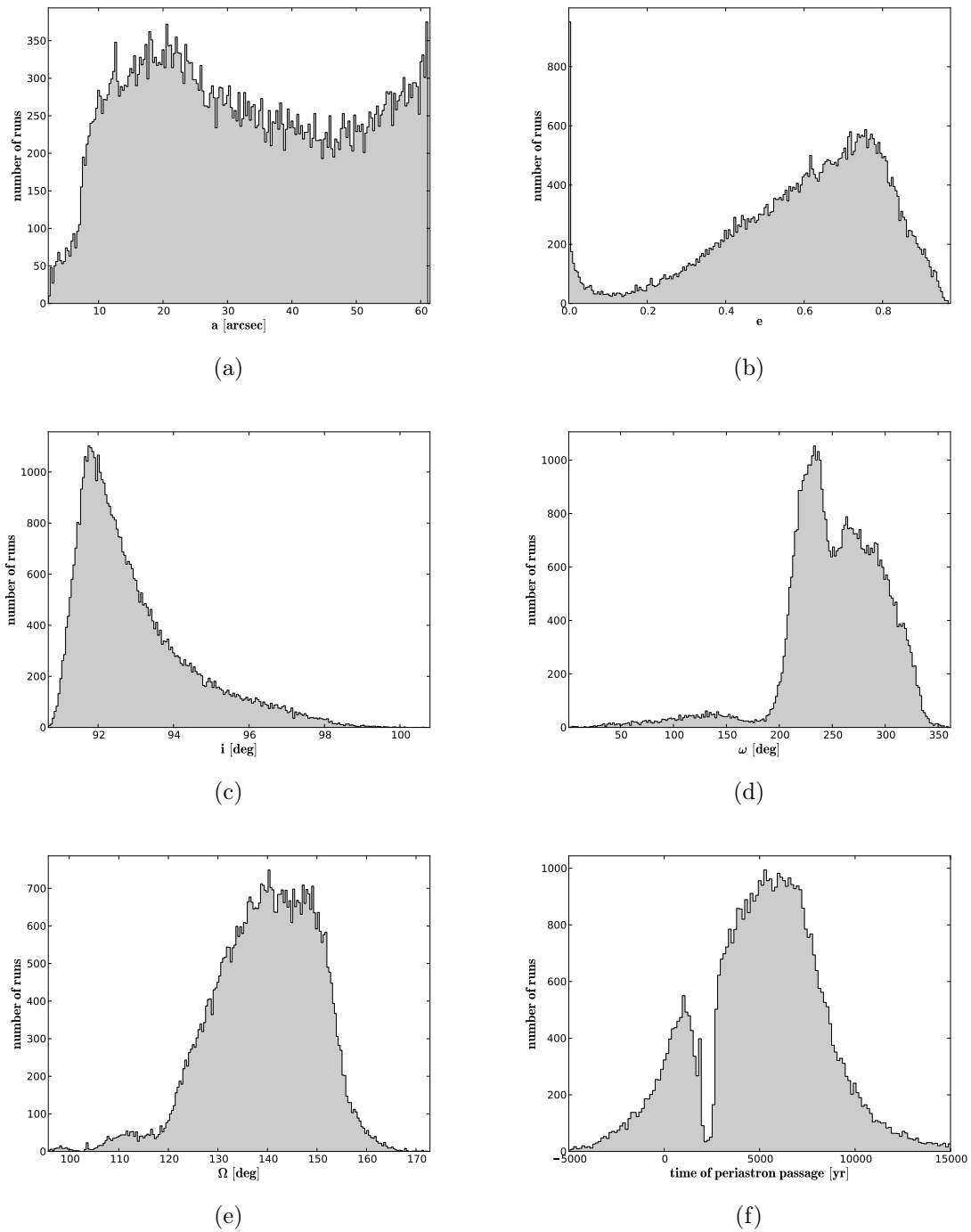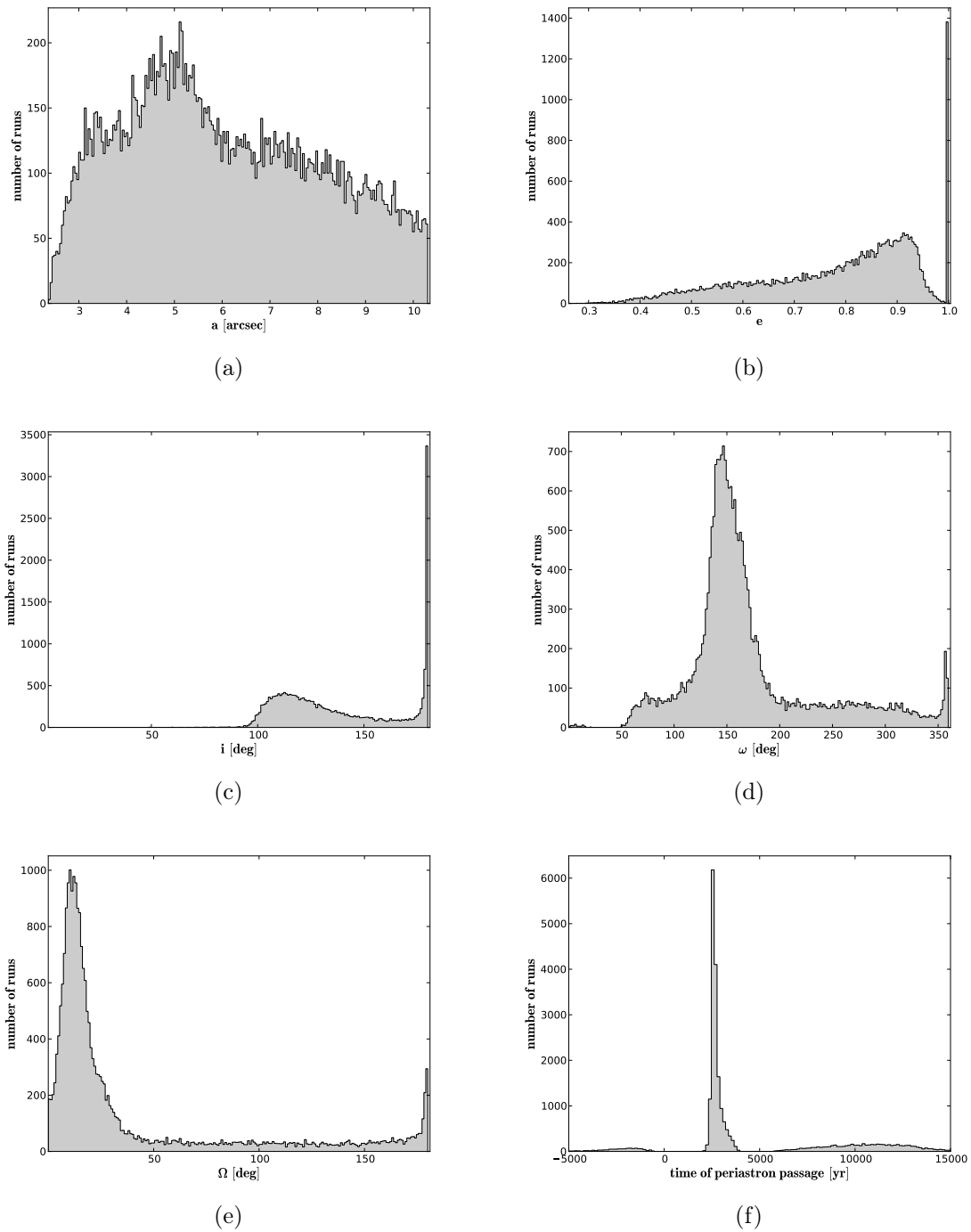
Figure 35: Results of the LSMC fits to the astrometric data points. Shown are the distributions of the orbital elements of GSC 08047-00232 B around A for all solutions out of 1,000,000 runs with $\chi^2_{red} < 2$. The data has been sorted in 200 bins in each diagram.

In Fig. 36(b) the inclination is shown as function of eccentricity. Inclinations of $\sim 180°$ are only existing for eccentricities larger than ~ 0.7, i.e. all face-on orbit solutions have very high eccentricities. For smaller eccentricities the inclination is also smaller with values down to $\sim 100°$, i.e. closer to an edge-on orbit. This is understandable given the linear change of the separation in the observed time period.

The observed peaks in the distributions of the longitude of the ascending node and the

Table 25: Most probable range and peak of orbital elements of the GSC 08047-00232 system

Parameter		Range	Peak
Semi-major Axis	a [arcsec]	2.36 - 10.3	-
Eccentricity	e	0.26 - 0.999	0.999 / 0.91
Orbital Period	P [yr]	3031.8 - 27629.8	-
Inclination	i [deg]	1.5 - 180	180 / 112.5
Long. of Asc. Node	Ω [deg]	0 - 180	10.4
Arg. of Periastron	ω [deg]	0.3 - 359.6	146.7
Periastron Passage	T_0 [yr]	-14824 - 14993	2511

Table 26: Orbital elements and χ^2_{red} of the best fit orbits shown in Fig. 37 and the best fit orbits with low eccentricity shown in Fig. 38

	Best Fit			Low Eccentricity		
Nr.	1	2	3	1	2	3
a [arcsec]	10.3	10.0	10.2	5.4	6.3	5.4
e	0.95	0.94	0.95	0.28	0.28	0.26
P [yr]	27458.9	26324.6	27429.8	10378.2	13092.9	10442.7
i [deg]	179.5	180.0	180.0	112.4	111.7	107.7
Ω [deg]	132.8	89.2	169.4	18.4	24.6	18.7
ω [deg]	271.4	224.9	308.1	95.3	98.5	128.4
T_0 [JD]	2626029.1	2629998.0	2625894.9	6557027.4	2798587.0	2987884.4
χ^2_{red}	0.43	0.43	0.43	2.0	2.0	2.0

argument of the periastron correspond in both cases to values for which good solutions are available over the full range of observed eccentricities. In the case of the longitude of the ascending node, no good solutions were found for values larger than $\sim 50°$ and eccentricities smaller than ~ 0.65. The same is the case for values of the argument of the periastron above $\sim 200°$.

The time of the periastron passage in Fig. 36(f) shows a smaller spread towards higher eccentricities and a somewhat higher spread below eccentricities of ~ 0.65. However, most of the discussed solutions put the time of the periastron passage in the region of the observed peak of the distribution, which is approximately the year 2511. It should be noted though, that the spread is still in the order of a few hundred years. There are only very few solutions that put the time of the periastron passage close to the observation epochs.

In Fig. 37 the three best fitting orbits are shown out of 1,000,000 LSMC runs. The corresponding orbital elements are listed in Tab. 26. In addition, the three orbits with the lowest eccentricities and $\chi^2_{red} <= 2$ are shown in Fig. 38. The corresponding orbital elements are also listed in Tab. 26. In general, orbits with lower eccentricities fit not as well to the data points as orbits with higher eccentricities.
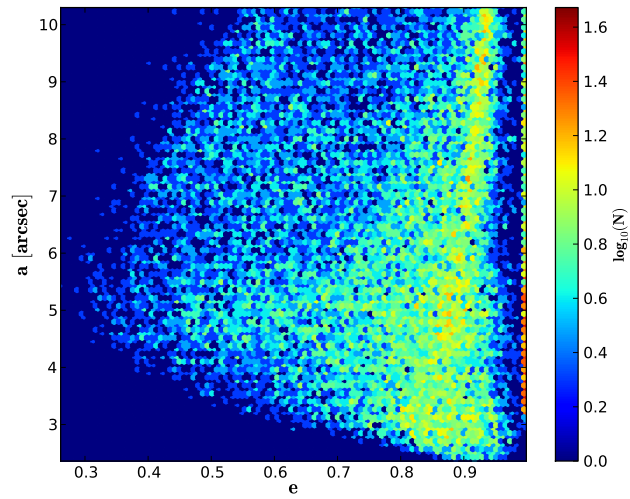
(a)
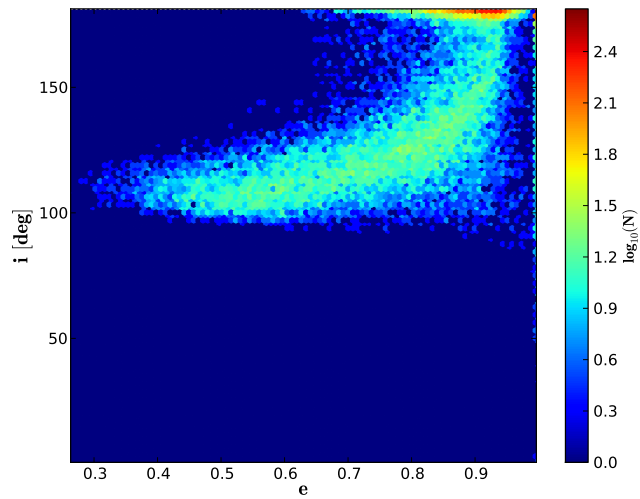
(b)
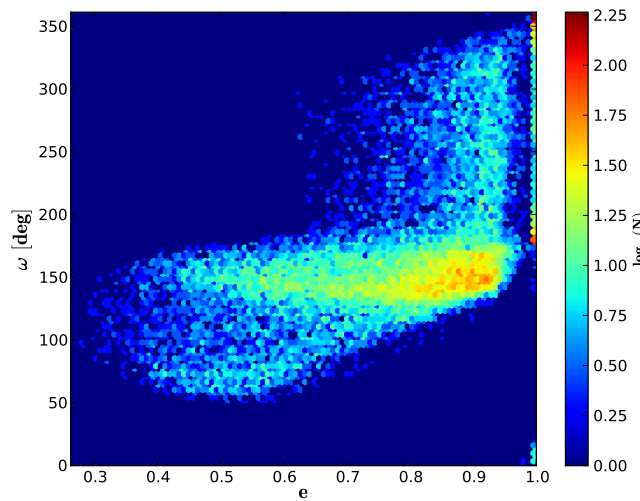
(c)
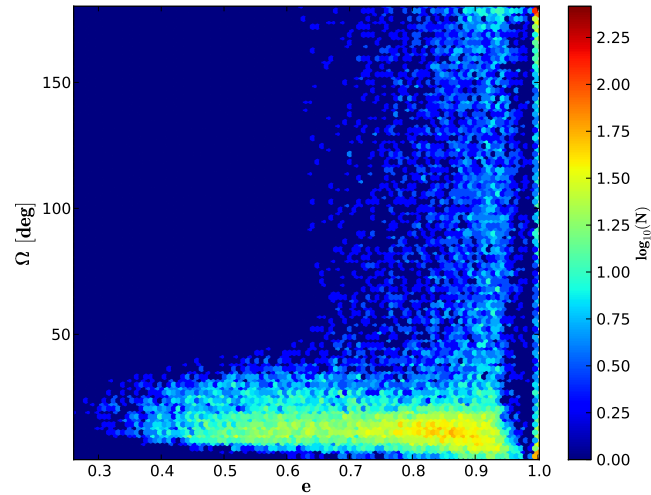
(e)
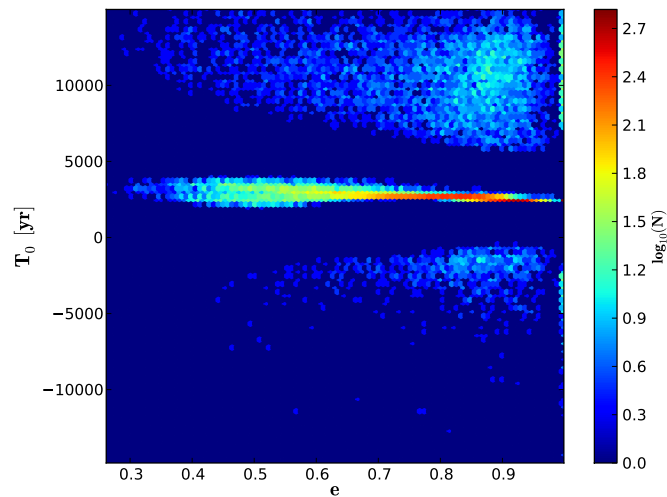
(f)

Figure 36: Orbital elements of GSC 08047-00232 B around A as function of eccentricity for all solutions out of 1,000,000 runs with $\chi^2_{red} < 2$. Logarithmic density of solutions is indicated by color.

(a)

(b)
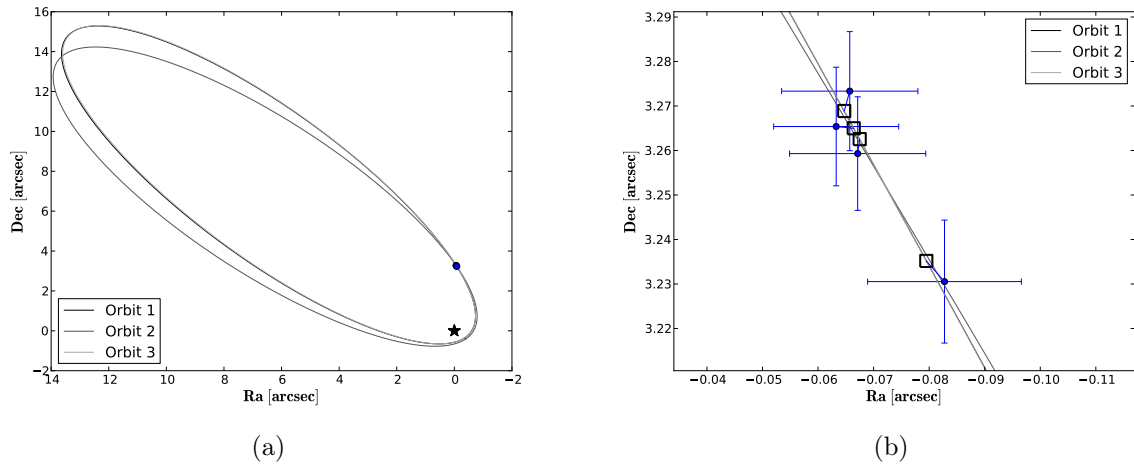
Figure 37: Top 3 best fitting orbits of the GSC 08047-00232 system out of 1,000,000 runs of the LSMC fit. Solid lines represent the apparent orbits. 37(b) is zoomed in on the data points. The corresponding orbital elements are listed in Tab. 26

(a)

(b)
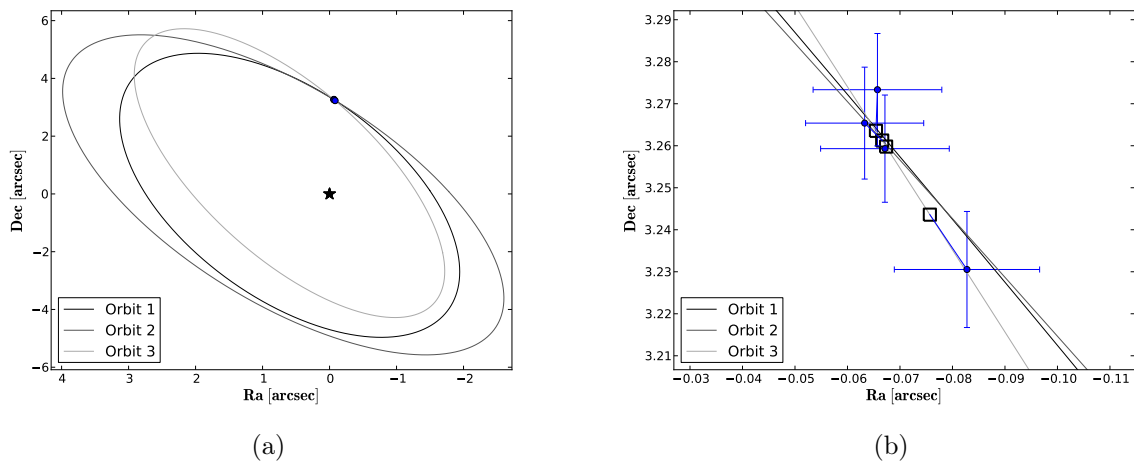
Figure 38: Best fitting orbits of the GSC 08047-00232 system out of 1,000,000 runs of the LSMC fit with low eccentricity. Solid lines represent the apparent orbits. 38(b) is zoomed in on the data points. The corresponding orbit elements are listed in Tab. 26

5.3   Dynamic Range and Detection Limits

For an analysis of the orbital motion of the discussed substellar companions, it is important to determine if there could be other substellar objects present in the respective systems. The deep VLT/NaCo images as well as the Calar Alto images were used to calculate the dynamic range and detection limits of these observations. For this purpose, a PYTHON program was written within the frame of this work, the source code[9] of which is shown in appendix A.4. As input, the program takes the science image, the pixel scale of this image, the coordinates of the peak of the reference source, the distance of the reference source, the absolute magnitude of the reference source in the same band as the science image, and a luminosity-mass model file. The program determines the peak count of the reference source (in most cases the primary star) and measures the background noise by determining the standard deviation in measuring boxes. The user must also specify the size of the measuring box and the desired signal-to-noise ratio. The separation of the central pixel of the measuring box from the reference source is saved along with the noise measurement. The achievable magnitude difference Δm is then calculated for each of these measurements by:

$$\Delta m \,=\, 2.5\,log_{10}\left(\frac{peak}{noise}\right) - 2.5\,log_{10}(S/N)\;,$$

wherein S/N is the specified signal-to-noise ratio. This calculation is done with the measuring box centered on each pixel of the input image. Results that have the same separation from the reference source are then averaged, so that there is one resulting achievable magnitude difference for a given separation. Separations are originally measured in pixels. The provided pixel scale is then used to convert the separation to angular values. The angular separations are in turn used to calculate projected separations, given the provided distance of the reference source. Angular and projected separations are both indicated in the resulting plot.

With the absolute magnitude of the reference source, the achievable magnitude difference can be translated into limiting magnitudes at the given separations. With these limiting magnitudes, and the provided luminosity-mass model, the program determines the limiting mass at a given separation. Mass limits for 0.25 arcsec, 0.5 arcsec, 1 arcsec and 2 arcsec were calculated for each target system.

For all mass calculations in this section, the DUSTY models by Chabrier et al. (2000) were used. The DUSTY models include condensed dust particles of various species in the equation of state and the radiative transfer equations. They hence include the dust opacity, which is believed to have a major influence on the IR colors below an effective temperature of 2000 K (see also Chabrier et al. 2000). It was shown in the reference publication that these models reproduce the infrared colors and flux of late M and L dwarfs accurately, i.e.

---

[9]Several versions of the program have been written for specific tasks. The source code which is shown is the general purpose version of the program.

they are well suited to predict the major physical parameters of all companions discussed in this work. There are meanwhile more accurate models to describe T (methane) dwarfs and giant extrasolar planets (especially hot Jupiters), as discussed in Baraffe et al. (2003). However, the predicted photometry of the DUSTY models does not vary much (~ 0.1 mag) from these models and hence the calculated mass limits should be fairly accurate even towards lower masses. The predicted absolute magnitudes in K as function of the mass and the age of the presumed object are shown in Fig.39.

Photometry and separation from the respective discovery publications were used to indicate
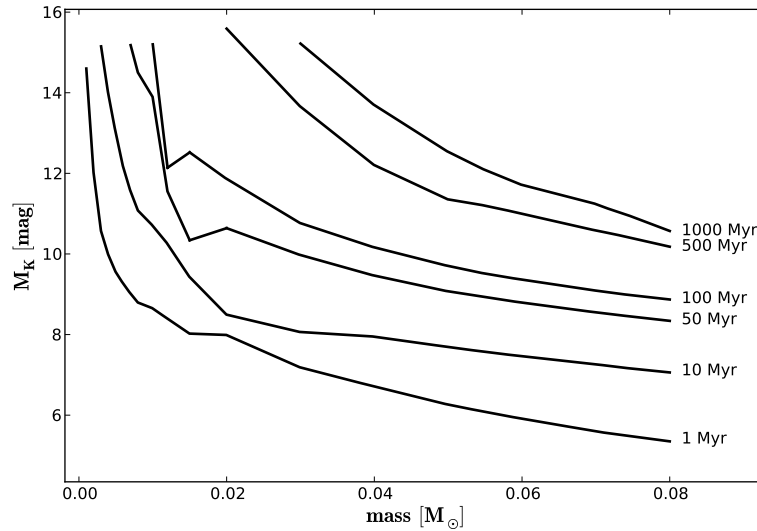
Figure 39: Absolute K-band magnitude versus object mass for substellar objetcs. The data was taken from the DUSTY models by Chabrier et al. (2000). The object age for each track is indicated on the right site of the diagram.

the position of the known companion in all dynamic range diagrams. Relative photometry of companions and host stars could be done in the VLT/NaCo images, but was not the main focus of this work. Furthermore, the infrared magnitudes of all discussed companions are already well known.

5.3.1   HD 130948

The Calar Alto and VLT epochs were used to determine detection limits. Since there is a general agreement that HD 130948 is younger than 1 Gyr (see Dupuy et al. 2009), the model tracks for an age of 0.5 Gyr were used. The resulting dynamic range plots are shown in Fig. 40.

In the case of the VLT/NaCo observing epoch, the apparent K magnitude of the primary (4.458 ± 0.020 mag, Cutri et al. 2003) was used as flux reference, since the NB 2.17 filter has its maximum throughput in this band. Also, there are no model tracks available for such narrow band filters. Given the distance of 18.17 ± 0.11 pc, the primary exhibits an

absolute magnitude in the K-band of 3.22 ± 0.02 mag. Considering this, all companions with masses similar to HD 130948 B and C would have been detected in the VLT/NaCo image, down to ~ 0.25 arcsec or ~ 5 AU of projected separation. In the mostly background-limited region outside ~ 1 arcsec (18 AU) and up to ~ 6.5 arcsec (118 AU), masses down to 0.0287 ± 0.0002 M$_\odot$ could have been detected.

The Calar Alto epoch of 2002 April 26 had a better Strehl ratio than the later 2006 epoch and was therefore used to determine detection limits. Since the primary was saturated in this image, the combined flux of the unresolved binary companion was used as the flux reference. Utilizing the measurements of Dupuy et al. (2009), the unresolved companion has a combined absolute magnitude in H of 11.1 ± 0.2 mag. As expected, the Calar Alto images are not as sensitive close to the primary. Additionally, substellar companions with an age of ~ 0.5 Gyr are much fainter in the H-band than in the K-band. However, companions with masses down to 0.0300 ± 0.0001 M$_\odot$ would still have been detected in the mostly background-limited region outside of ~ 5 arcsec (91 AU) and up to ~ 28 arcsec (509 AU).
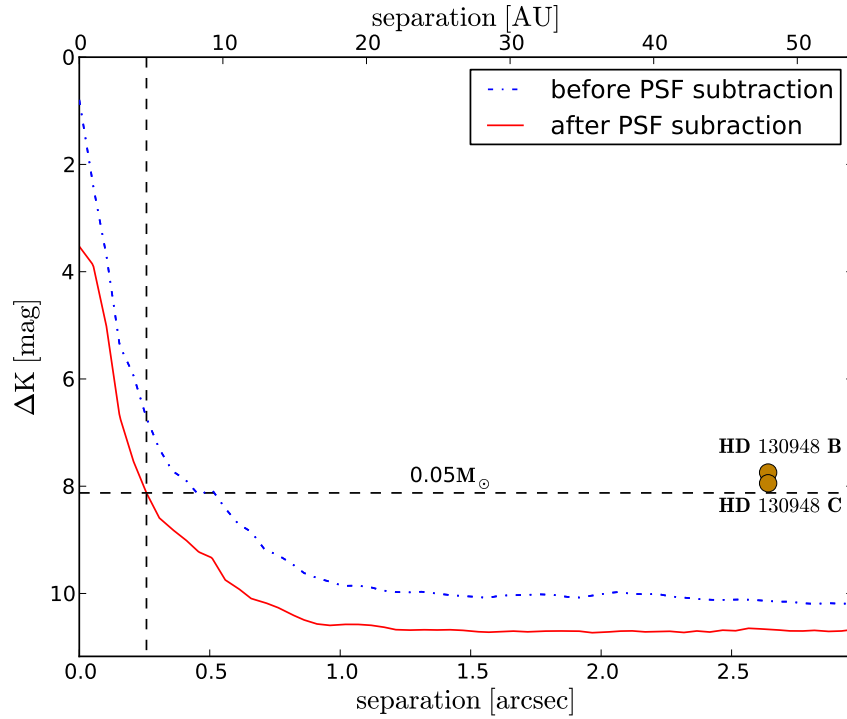
(a) VLT/NaCo epoch of 2009-07-03
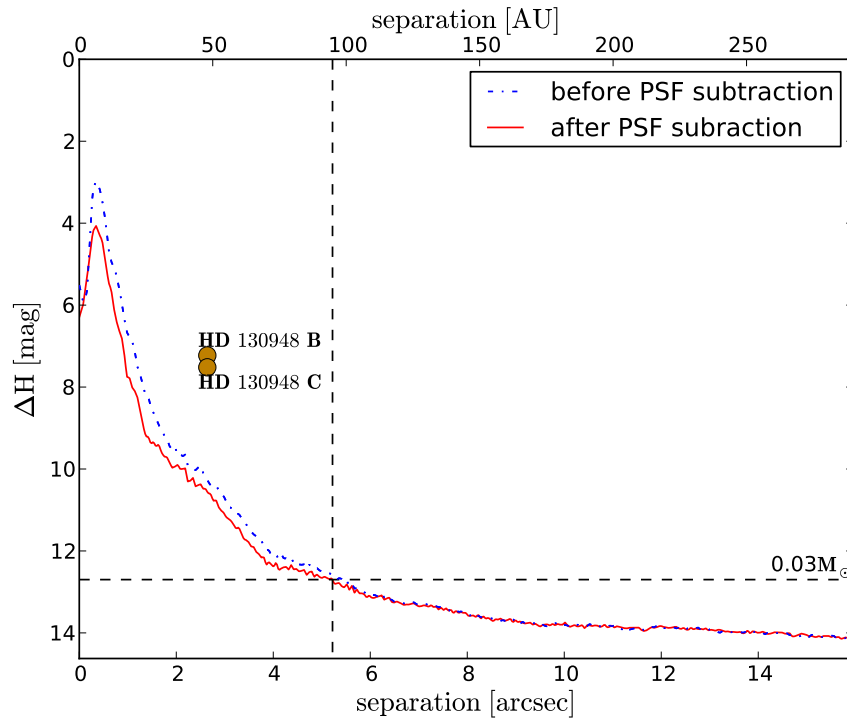
(b) Calar Alto epoch of 2002-04-26

Figure 40: Dynamic range plots for the NaCo and Calar Alto images of HD 130948 before and after PSF subtraction. All objects above the solid (red) or dash-dotted (blue) lines are detectable. These lines mark the detection limit for a signal-to-noise of 5. The filled circles mark the position of HD 130948 B and C. The mass limit was calculated using the DUSTY models by Chabrier et al. (2000)

5.3.2   HD 203030

The dynamic range plot for HD 203030 is shown in Fig. 41. The VLT/NaCo image of HD 203030 was taken in the NB 2.17 filter. As in the case of HD 130948 in the previous section, the model tracks for the K-band were utilized to calculate detection limits. Since the age range of HD 203030 is between 130 Myr and 400 Myr (Metchev and Hillenbrand 2006), an interpolation was made between the model tracks for 100 Myr and 500 Myr to calculate the magnitudes for 300 Myr.

Considering the Hipparcos parallax of 24.48 ± 1.05 mas (40.85 pc), the primary star exhibits an absolute magnitude in the K-band of 3.59 ± 0.068 mag (Cutri et al. 2003). Given the model tracks and the calculated dynamic range, objects with masses[10] down to $0.047 \pm 0.001 \, M_\odot$ would have been detected down to an angular separation of 0.25 arcsec (10 AU). Less massive objects of $0.032 \pm 0.001 \, M_\odot$ could have been detected outside of 0.5 arcsec (20 AU). In the background-limited region outside of 2 arcsec (82 AU) and up to 6.6 arcsec (270 AU), objects with masses down to $0.0191 \pm 0.0004 \, M_\odot$ would have been detected. Objects outside of 6.6 arcsec could only be detected to the north and south up to a separation of 13.2 arcsec (539 AU), and to the east up to a separation of 22 arcsec (899 AU), due to the placement of HD 203030 in the field of view of the NaCo S 27 detector.

---

[10]The uncertainty of the minimum detection mass includes the uncertainty of the photometry of the primary and of the distance.

Figure 41: Dynamic range plot for the NaCo image of HD 203030 before and after PSF subtraction. All objects above the solid (red) or dash-dotted (blue) lines are detectable. These lines mark the detection limit for a signal-to-noise of 5. The position of the companion ($\Delta K_s = 9.56$ at a separation of 11.9 arcsec, Metchev and Hillenbrand 2006) is indicated with the black arrow.

5.3.3   DH Tau

The dynamic range plot for DH Tau is shown in Fig. 42. The age of the DH Tau system is still a matter of discussion. As pointed out in section 2.1.3, the age of the primary is believed to be between 0.1 Myr and 4.4 Myr, while the age of the companion measured by spectroscopy is estimated to be between 3 Myr and 10 Myr. Subsequently, model tracks for an age of 1 Myr and 10 Myr were used to calculate the detection limits.

Considering the distance of DH Tau of 140 ± 10 pc, and the apparent magnitude in the K-band of 8.178 ± 0.026 mag (Cutri et al. 2003), the absolute magnitude of DH Tau in the K-band is 2.446 ± 0.157 mag. Utilizing this magnitude and the model plots for 1 Myr, the minimum detectable mass down to a separation of 0.25 arcsec (35 AU) is 0.0034 ± 0.0003 $M_\odot$. This changes to a larger mass of 0.0116 ± 0.0007 $M_\odot$ if the model tracks for older objects with an age of 10 Myr are used. At a separation of 0.5 arcsec (70 AU), masses down to 0.0022 ± 0.0001 $M_\odot$ and 0.0067 ± 0.0003 $M_\odot$ are detectable for young and old objects respectively. In the background-limited region outside of 2 arcsec (280 AU) and up to 6.5 arcsec (910 AU), minimum mass objects of 0.00181 ± 0.00006 $M_\odot$ and 0.0056 ± 0.0002 $M_\odot$ would have been detected.

Figure 42: Dynamic range plot for the NaCo image of DH Tau before and after PSF subtraction. All objects above the solid (red) or dash-dotted (blue) lines are detectable. These lines mark the detection limit for a signal-to-noise of 5. The position of the companion ($\Delta K = 6.01$ at a separation of 2.34 arcsec, Itoh et al. 2005) is indicated with the filled circle.

5.3.4 GSC 08047-00232

The dynamic range plot for GSC 08047-00232 is shown in Fig. 43. The age of GSC 08047-00232 A was discussed in section 2.1.4. It lies within 10 Myr to 40 Myr, as this is the general age range of the TucHor association. DUSTY model tracks are available for ages of 10 Myr and 50 Myr. Conservatively, the model tracks for older objects were choosen to calculate detection limits. If GSC 08047-00232 A were indeed as young as 10 Myr, the minimum detectable mass would be approximately 0.005 $M_\odot$ smaller at all separations.

The distance of GSC 08047-00232 was not measured directly, but is only inferred from infrared colors and magnitudes and kinematic considerations, as was also discussed in section 2.1.4. There is a general consensus that the system should be ~ 85 pc away if the primary is coeval with the rest of the TucHor stars, hence 85 pc was adopted for calculation of the absolute magnitude of the primary. Considering this and the primary's apparent magnitude in the K-band of 8.405 ± 0.027 mag (Cutri et al. 2003), the absolute magnitude in the K-band is 3.758 ± 0.027 mag. The uncertainty is the one from the apparent magnitude. If an additional uncertainty in distance of ~ 20 pc was to be considered, the uncertainty of the absolute magnitude of the primary would be larger by ~ 0.5 mag. This would lead to an increase of the uncertainties of the calculated minimum masses by a factor of ~ 4.

Given the absoulte magnitude of the primary and the DUSTY model tracks for an age of

50 Myr, masses down to $0.0129 \pm 0.0001 \, M_\odot$ would have been detected down to a separation of 0.25 arcsec (21 AU). This is close to the planetary mass limit of $0.0124 \, M_\odot$, and significantly below it if the system is indeed younger than 50 Myr. At a separation of 0.5 arcsec (43 AU), lower mass objects down to $0.0115 \pm 0.00002 \, M_\odot$ were detectable. In the background-limited region outside of 2 arcsec (170 AU) and up to 6.5 arcsec (553 AU), this goes down further to masses of $0.0109 \pm 0.00002 \, M_\odot$.
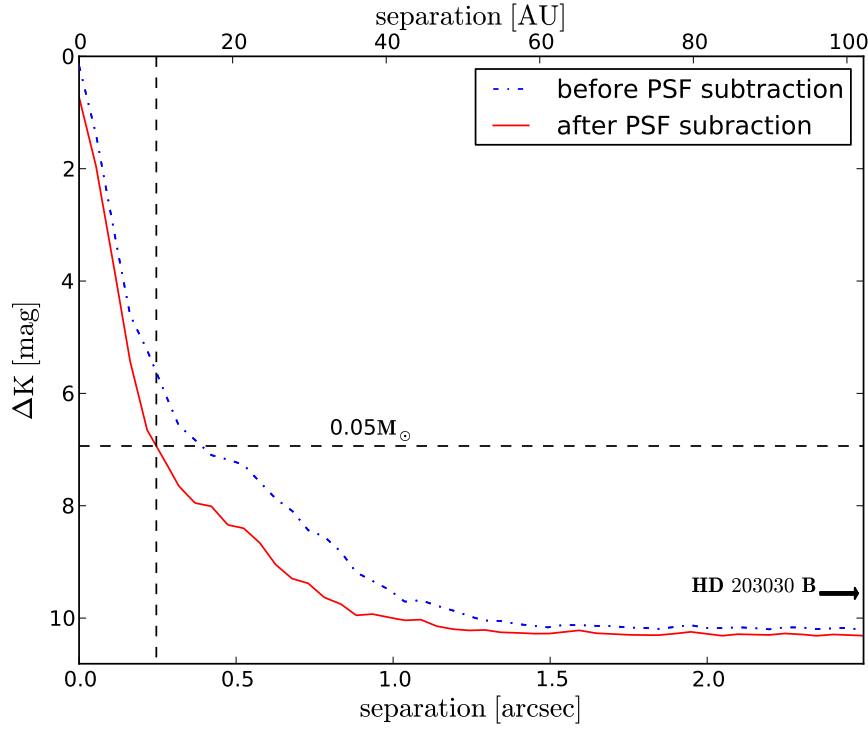

Figure 43: Dynamic range plot for the NaCo image of GSC 08047-00232 before and after PSF subtraction. All objects above the solid (red) or dash-dotted (blue) lines are detectable. These lines mark the detection limit for a signal-to-noise of 5. The position of the companion ($\Delta K = 6.50$ at a separation of 3.21 arcsec, Chauvin et al. 2005) is indicated with the filled circle.

5.3.5   1RXS J160929.1-210524

The dynamic range plot for 1RXS J160929.1-210524 is shown in Fig. 44. As discussed in section 2.1.5, the age of US is believed to be between 5 Myr and 6 Myr, but was recently re-evaluated and could be up to 13 Myr (11 ± 2 Myr , Pecaut et al. 2012). Consequently, model tracks for an age of 5 Myr and 10 Myr were used to calculate detection limits. Considering the distance of US of 145 ± 20 pc and the apparent magnitude of the primary star in the K-band of 8.916 ± 0.021 mag (Cutri et al. 2003), the absolute magnitude of the primary in the K-band is 3.11 ± 0.30 mag. Utilizing this magnitude and the model tracks for a younger age, objects down to $0.0059 \pm 0.0006 \, M_\odot$ would have been detected down to an angular separation of 0.25 arcsec (36 AU). If US is indeed older, this changes towards slightly higher masses of $0.0086 \pm 0.0013 \, M_\odot$. At an angular separation of 0.5 arcsec

(73 AU), lower mass objects down to $0.0036 \pm 0.0003\,M_\odot$ and $0.0051 \pm 0.0003\,M_\odot$ for the two different ages respectively would have been detected. In the background-limited region outside of 2 arcsec (290 AU) and up to 6.5 arcsec (943 AU), the minimum detectable mass is $0.0029 \pm 0.0002\,M_\odot$ for an age of 5 Myr and $0.0041 \pm 0.0003\,M_\odot$ for an age of 10 Myr.
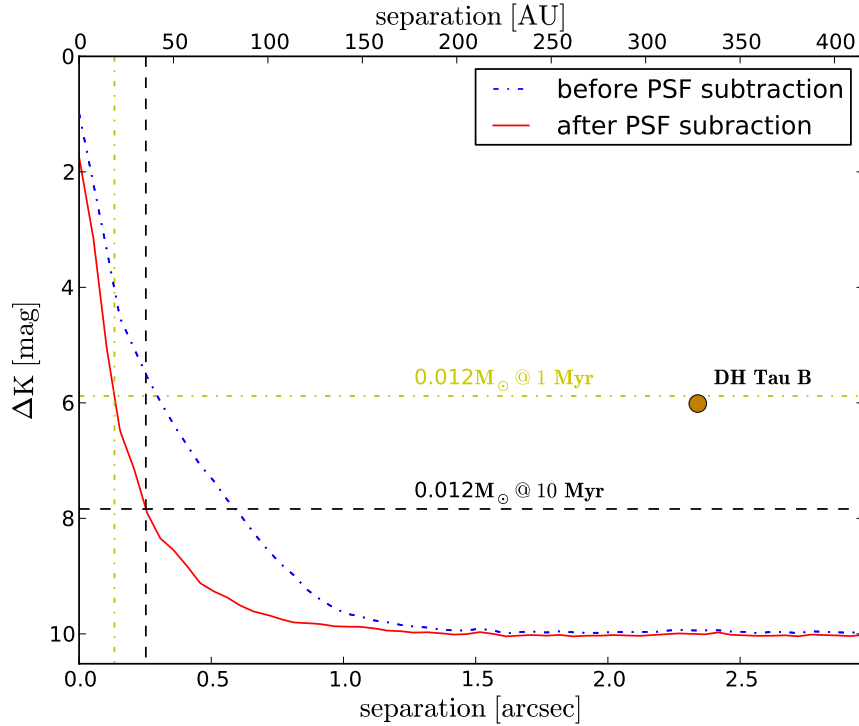

Figure 44: Dynamic range plot for the NaCo image of 1RXS J160929.1-210524 before and after PSF subtraction. All objects above the solid (red) or dash-dotted (blue) lines are detectable. These lines mark the detection limit for a signal-to-noise of 5. The position of the companion ($\Delta K = 7.25$ at a separation of 2.22 arcsec, Lafrenière et al. 2008) is indicated with the filled circle.

5.3.6   UScoCTIO 108

The dynamic range plot for UScoCTIO 108 is shown in Fig. 45. UScoCTIO 108 is a member of US like 1RXS J160929.1-210524, and hence is located at approximately the same distance of 145 ± 20 pc, and has a similar age. Consequently, detection limits were again computed for ages of 5 Myr and 10 Myr.

Given the distance of US, and the apparent magnitude of UScoCTIO 108 A in the K-band of 12.51 ± 0.13 mag (Béjar et al. 2008), it exhibits an absolute magnitude in the K-band of 6.70 ± 0.33 mag. Since UScoCTIO 108 A is very faint there is no significant difference in detection limits between 0.25 arcsec (36 AU) and 2 arcsec (290 AU). For an age of 10 Myr, all objects down to masses of $0.015 \pm 0.001\,M_\odot$ would have been detected in the field of view of the detector up to an angular seperation of 6.5 arcsec (943 AU). For a younger age of 5 Myr, this limit is slightly lower with $0.013 \pm 0.002\,M_\odot$. In general, the detection limits are not as low as in the other VLT/NaCo images given the young age of the system.

This is because the very faint primary was used for AO corrections, which were hence less optimal than the AO corrections for the other discussed targets with brighter primary stars as reference sources. This can also be seen in Fig. 15(h), where the companion is considerably blurred in comparison with the other observed targets.
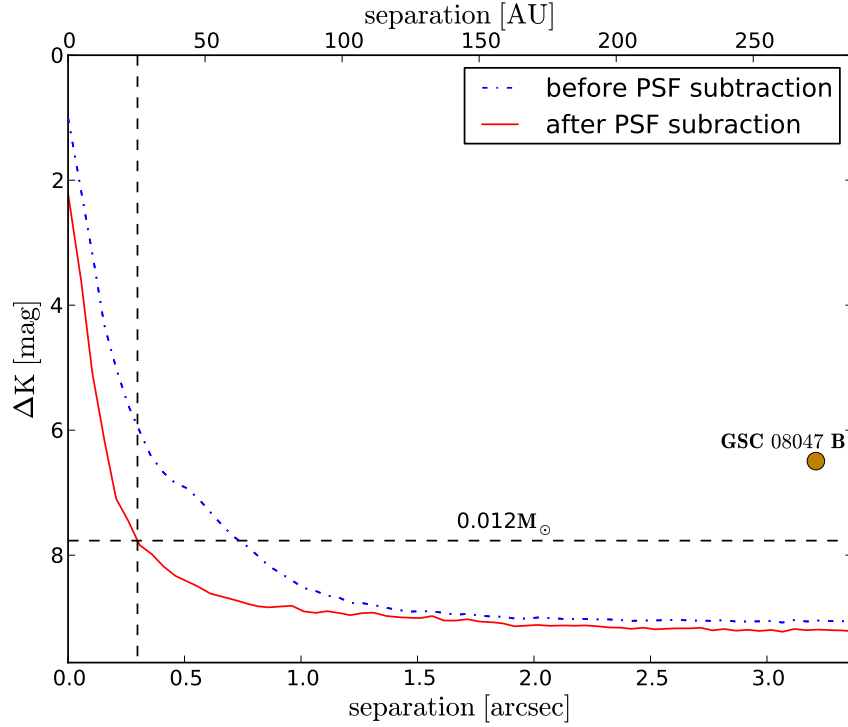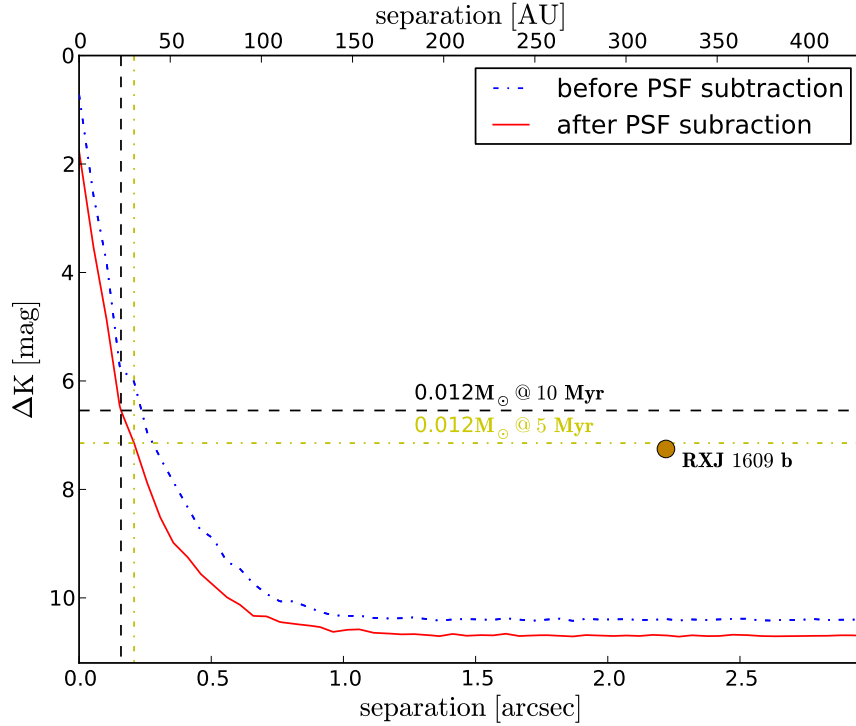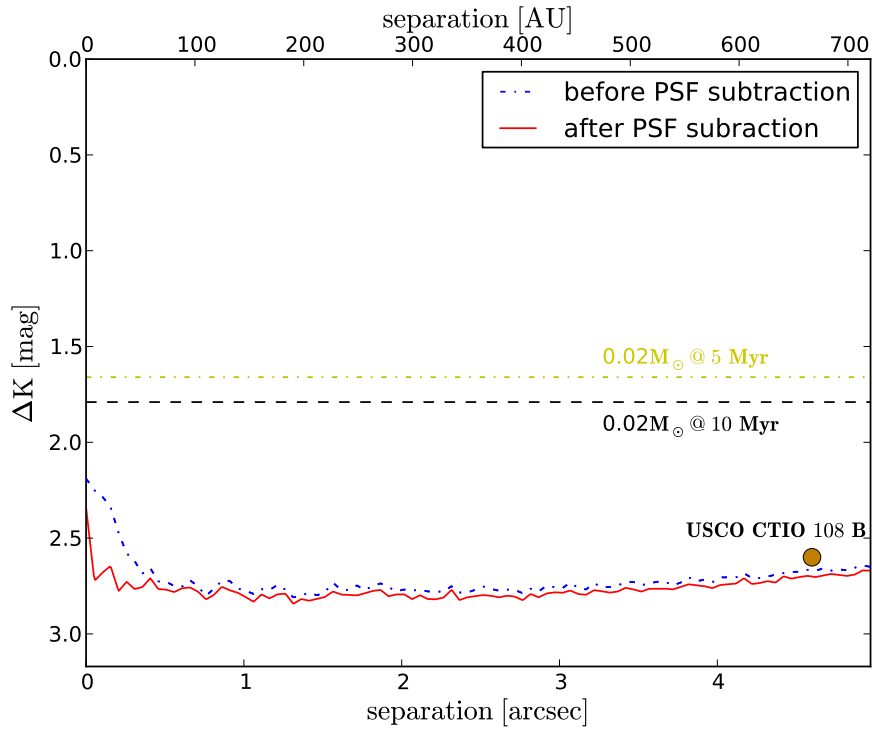

Figure 45: Dynamic range plot for the NaCo image of UScoCTIO 108 before and after PSF subtraction. All objects above the solid (red) or dash-dotted (blue) lines are detectable. These lines mark the detection limit for a signal-to-noise of 5. The position of the companion ($\triangle K = 2.6$ at a separation of 4.6 arcsec, Béjar et al. 2008) is indicated with the filled circle.

6 Summary and Conclusions

This work explored whether orbital motion of wide directly imaged substellar companions is detectable with currently available astrometric accuracy and time baselines. For this purpose, a group of six previously known systems with substellar companions was observed with the Calar Alto 3.6 m telescope and the ESO VLT, to obtain well-calibrated astrometric measurements. In addition, science archive and literature data was evaluated. As a result of this analysis, differential motion between primary stars and substellar companions could be clearly detected in three of the six discussed systems, namely HD 130948, DH Tau and GSC 08047-00232. In addition, there was marginal differential motion detected in the HD 203030 system. This differential motion is in all cases consistent with slow orbital motion, although no curvature of the orbits could yet be detected. In Fig. 46 the projected orbital motion of the discussed systems is compared with the orbital motion of T Tauri binary star systems as measured by Woitas et al. (2001). They examined a sample of 34 T Tauri binaries with a projected separation smaller than 100 AU. Of the four systems with detected differential motion discussed in this work, only HD 130948 BC have a smaller separation than 100 AU from their primary star. As would be expected for less massive objects, the projected velocity of the HD 130948 BC system around HD 130948 A is smaller than the velocities measured for binary star systems with similar projected separations by Woitas et al. (2001). The substellar companions to DH Tau, GSC 08047-00232 and HD 203030 are located at larger projected separations. Their projected orbit velocities are slightly larger than the one of HD 130948 BC, but still smaller than the majority of the binary orbit velocities. The few T Tauri binaries that exhibit a smaller orbit velocity than these companions could be inclined in a way that most of the orbital motion happens in radial direction. The slightly larger orbital motion of the substellar companions could also be an indication for eccentric orbits and orbit positions close to periastron or apastron. It should, however, be noted that there was no uncertainty calculated for the DH Tau data point, because the differential motion was only fitted linearly between two data points. In general, the small projected orbital motion of the companions is consistent with a lower mass and a larger projected separation than the binary stars.

In all but one of the discussed systems (UScoCTIO 108), it could be ruled out with higher significance than was known before that the companions are chance-projected background objects.

A method to constrain the orbital elements of the discussed systems was developed. The Least Squares Monte Carlo (LSMC) approach covers large areas of the parameter space by combining the random Monte Carlo approach with the ability of the Levenberg-Marquardt algorithm to find local minima. The LSMC fit was implemented with the PYTHON programming language. With this fitting program, the orbital parameters of the HD 130948 system and the GSC 08047-00232 system were successfully constrained. In the case of HD 130948 BC around A, it is particularly interesting that the average of the fitted inclina-

tion of $i = 93.0° \pm 1.5°$ lies within $2\,\sigma$ of the inclination derived for the BC binary by Dupuy et al. (2009). A similar inclination would be expected if BC has formed in a disk around A. Furthermore, it can already be concluded that the orbit is either highly eccentric with e>0.6 and a semi-major axis larger than 10 arcsec ($>\,180$ AU), or nearly circular with a semi-major axis between ~ 50 arcsec and ~ 61 arcsec (909 to 1110 AU). A semi-major axis of $a > 10$ arcsec corresponds to orbital periods longer than 5000 yr. In general, the orbit solutions for HD 130948 BC around A are nearly edge-on in case of low eccentricities, or very eccentric in case of higher inclinations, fitting with the linear differential motion of primary and companions detected so far.

The orbit of GSC 08047-00232 B around A is either seen face-on with a high eccentricity e>0.65 or in between face-on and edge-on with lower eccentricities down to e = 0.26. For highly eccentric orbits with e>0.85, solutions were found for a range of semi-major axes from 2.36 arcsec to 10.3 arcsec (200 AU to 880 AU). In case of smaller eccentricities, the range of semi-major axes is smaller. For e = 0.4 they range from 4 arcsec to 8 arcsec (340 AU to 680 AU) and for e = 0.3 they range from 5 arcsec to 6 arcsec (425 AU to 510 AU). This is all very consistent with the observed differential motion in separation which can be fitted well with a linear function.

Given the wide range of possible orbits in the systems where differential motion was detected, it is not yet possible to constrain their system mass. Significant curvature of the orbit needs to be detected to constrain the orbital elements more precisely if such an undertaking ought to be successful.

Other than the physical challenges of long orbital periods and hence very small orbital motion, the biggest problems for the detection of orbital motion are the differences in astrometric calibrations. As demonstrated in section 4.1, two different astrometric calibrators can lead to significantly different astrometric solutions, and hence systematic offsets between different astrometric measurements. Thus, care needs to be taken when comparing data points taken with different instruments or in different observing epochs. Ideally observations should be executed with the same instrument setup and the same astrometric calibrators in each observing epoch. In general, open or globular clusters with known astrometric references are better suited as astrometric calibrators than wide binary stars. This is because slow, uncorellated differential motion of various cluster members will typically average out and will hence not influence the result of the astrometric calibration significantly. Wide binary stars, on the other hand, show slow orbital motion, which is unknown in most cases.
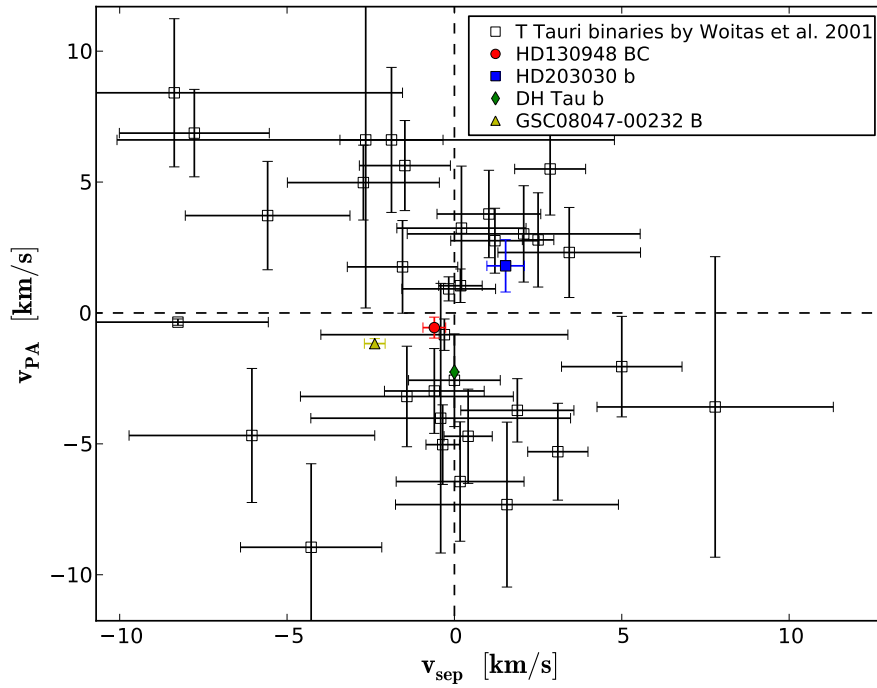
(a) Angular velocity versus radial velocity
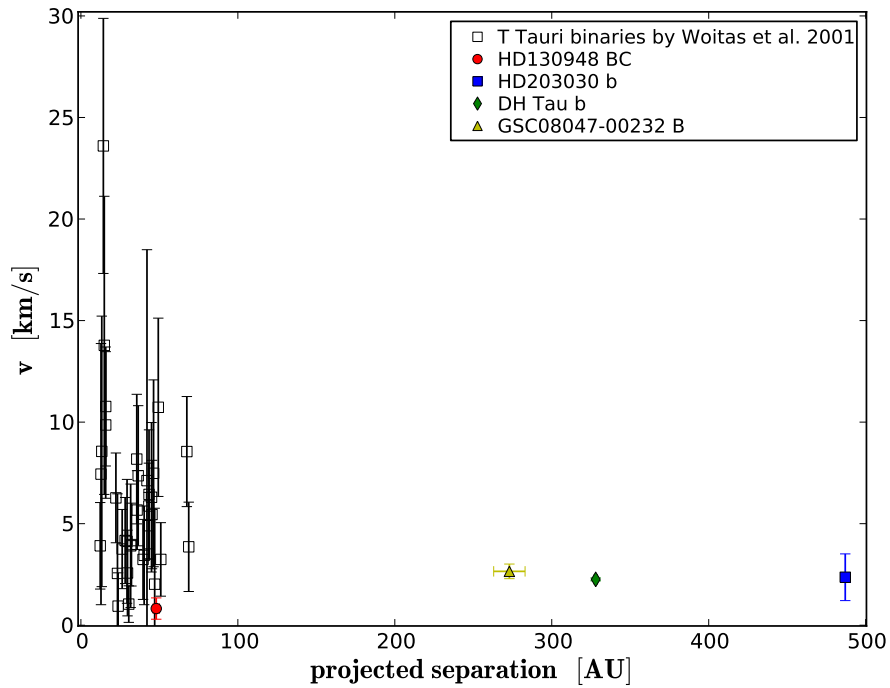
(b) Absolute velocity versus projected separation

Figure 46: Comparison of projected orbit velocities and projected separations of the companions discussed in this work and binary T Tauri systems discussed in Woitas et al. (2001). Shown are the angular and radial velocity of the companions with respect to the primary stars in Fig. 46(a) as well as the absolute projected velocities and projected separations in Fig. 46(b).

References

Allende Prieto, C. and Lambert, D. L. (1999). Fundamental parameters of nearby stars from the comparison with evolutionary calculations: masses, radii and effective temperatures. *A&A*, 352:555–562.

Alonso, R., Brown, T. M., Torres, G., Latham, D. W., Sozzetti, A., Mandushev, G., Belmonte, J. A., Charbonneau, D., Deeg, H. J., Dunham, E. W., O'Donovan, F. T., and Stefanik, R. P. (2004). TrES-1: The Transiting Planet of a Bright K0 V Star. *ApJ*, 613:L153–L156.

Alzner, A. (2004). *The Orbital Elements of a Visual Binary Star*, page 53.

Ardila, D., Martín, E., and Basri, G. (2000). A Survey for Low-Mass Stars and Brown Dwarfs in the Upper Scorpius OB Association. *AJ*, 120:479–487.

Baraffe, I., Chabrier, G., Allard, F., and Hauschildt, P. H. (1998). Evolutionary models for solar metallicity low-mass stars: mass-magnitude relationships and color-magnitude diagrams. *A&A*, 337:403–412.

Baraffe, I., Chabrier, G., Allard, F., and Hauschildt, P. H. (2002). Evolutionary models for low-mass stars and brown dwarfs: Uncertainties and limits at very young ages. *A&A*, 382:563–572.

Baraffe, I., Chabrier, G., Barman, T. S., Allard, F., and Hauschildt, P. H. (2003). Evolutionary models for cool brown dwarfs and extrasolar giant planets. The case of HD 209458. *A&A*, 402:701–712.

Barnes, S. A. (2003). On the Rotational Evolution of Solar- and Late-Type Stars, Its Magnetic Origins, and the Possibility of Stellar Gyrochronology. *ApJ*, 586:464–479.

Barnes, S. A. (2007). Ages for Illustrative Field Stars Using Gyrochronology: Viability, Limitations, and Errors. *ApJ*, 669:1167–1189.

Béjar, V. J. S., Zapatero Osorio, M. R., Pérez-Garrido, A., Álvarez, C., Martín, E. L., Rebolo, R., Villó-Pérez, I., and Díaz-Sánchez, A. (2008). Discovery of a Wide Companion near the Deuterium-burning Mass Limit in the Upper Scorpius Association. *ApJ*, 673:L185–L189.

Bertin, E. and Arnouts, S. (1996). SExtractor: Software for source extraction. *A&AS*, 117:393–404.

Beuzit, J.-L., Demailly, L., Gendron, E., Gigan, P., Lacombe, F., Rouan, D., Hubin, N., Bonaccini, D., Prieto, E., Chazallet, F., Rabaud, D., Madec, P.-Y., Rousset, G., Hofmann, R., and Eisenhauer, F. (1997). Adaptive Optics on a 3.6-Meter Telescope. The ADONIS System. *Experimental Astronomy*, 7:285–292.

Biller, B. A., Liu, M. C., Wahhaj, Z., Nielsen, E. L., Close, L. M., Dupuy, T. J., Hayward, T. L., Burrows, A., Chun, M., Ftaclas, C., Clarke, F., Hartung, M., Males, J., Reid, I. N., Shkolnik, E. L., Skemer, A., Tecza, M., Thatte, N., Alencar, S. H. P., Artymowicz, P., Boss, A., de Gouveia Dal Pino, E., Gregorio-Hetem, J., Ida, S., Kuchner, M. J., Lin, D., and Toomey, D. (2010). The Gemini NICI Planet-finding Campaign: Discovery of a Close Substellar Companion to the Young Debris Disk Star PZ Tel. *ApJ*, 720:L82–L87.

Bird, J. and Metchev, S. (2010). Brown Dwarf Companions Database. In *American Astronomical Society Meeting Abstracts #215*, volume 36 of *Bulletin of the American Astronomical Society*, page #606.05.

Borucki, W. J., Koch, D., Basri, G., Batalha, N., Brown, T., Caldwell, D., Caldwell, J., Christensen-Dalsgaard, J., Cochran, W. D., DeVore, E., Dunham, E. W., Dupree, A. K., Gautier, T. N., Geary, J. C., Gilliland, R., Gould, A., Howell, S. B., Jenkins, J. M., Kondo, Y., Latham, D. W., Marcy, G. W., Meibom, S., Kjeldsen, H., Lissauer, J. J., Monet, D. G., Morrison, D., Sasselov, D., Tarter, J., Boss, A., Brownlee, D., Owen, T., Buzasi, D., Charbonneau, D., Doyle, L., Fortney, J., Ford, E. B., Holman, M. J., Seager, S., Steffen, J. H., Welsh, W. F., Rowe, J., Anderson, H., Buchhave, L., Ciardi, D., Walkowicz, L., Sherry, W., Horch, E., Isaacson, H., Everett, M. E., Fischer, D., Torres, G., Johnson, J. A., Endl, M., MacQueen, P., Bryson, S. T., Dotson, J., Haas, M., Kolodziejczak, J., Van Cleve, J., Chandrasekaran, H., Twicken, J. D., Quintana, E. V., Clarke, B. D., Allen, C., Li, J., Wu, H., Tenenbaum, P., Verner, E., Bruhweiler, F., Barnes, J., and Prsa, A. (2010). Kepler Planet-Detection Mission: Introduction and First Results. *Science*, 327:977–.

Boss, A. P. (1997). Giant planet formation by gravitational instability. *Science*, 276:1836–1839.

Boss, A. P. (2002). Evolution of the Solar Nebula. V. Disk Instabilities with Varied Thermodynamics. *ApJ*, 576:462–472.

Brandl, B., Smith, J. T., Wilson, J., Eisenhauer, F., and Houck, J. R. (1997). Adaptive optics high-spectral-resolution imaging of the planetary nebula IC 418 [3126-74]. In Tyson, R. K. and Fugate, R. Q., editors, *Society of Photo-Optical Instrumentation Engineers (SPIE) Conference Series*, volume 3126 of *Society of Photo-Optical Instrumentation Engineers (SPIE) Conference Series*, page 561.

Burrows, A., Marley, M., Hubbard, W. B., Lunine, J. I., Guillot, T., Saumon, D., Freedman, R., Sudarsky, D., and Sharp, C. (1997). A Nongray Theory of Extrasolar Giant Planets and Brown Dwarfs. *ApJ*, 491:856.

Carpenter, J. M., Mamajek, E. E., Hillenbrand, L. A., and Meyer, M. R. (2009). Debris Disks in the Upper Scorpius OB Association. *ApJ*, 705:1646–1671.

Casagrande, L., Schönrich, R., Asplund, M., Cassisi, S., Ramírez, I., Meléndez, J., Bensby, T., and Feltzing, S. (2011). New constraints on the chemical evolution of the solar neighbourhood and Galactic disc(s). Improved astrophysical parameters for the Geneva-Copenhagen Survey. *A&A*, 530:A138.

Chabrier, G., Baraffe, I., Allard, F., and Hauschildt, P. (2000). Evolutionary Models for Very Low-Mass Stars and Brown Dwarfs with Dusty Atmospheres. *ApJ*, 542:464–472.

Chauvin, G., Lagrange, A.-M., Bonavita, M., Zuckerman, B., Dumas, C., Bessell, M. S., Beuzit, J.-L., Bonnefoy, M., Desidera, S., Farihi, J., Lowrance, P., Mouillet, D., and Song, I. (2010). Deep imaging survey of young, nearby austral stars . VLT/NACO near-infrared Lyot-coronographic observations. *A&A*, 509:A52.

Chauvin, G., Lagrange, A.-M., Lacombe, F., Dumas, C., Mouillet, D., Zuckerman, B., Gendron, E., Song, I., Beuzit, J.-L., Lowrance, P., and Fusco, T. (2005). Astrometric and spectroscopic confirmation of a brown dwarf companion to GSC 08047-00232. VLT/NACO deep imaging and spectroscopic observations. *A&A*, 430:1027–1033.

Chauvin, G., Thomson, M., Dumas, C., Beuzit, J.-L., Lowrance, P., Fusco, T., Lagrange, A.-M., Zuckerman, B., and Mouillet, D. (2003). Adaptive optics imaging survey of the Tucana-Horologium association. *A&A*, 404:157–162.

Chen, W. P., Simon, M., Longmore, A. J., Howell, R. R., and Benson, J. A. (1990). Discovery of five pre-main-sequence binaries in Taurus. *ApJ*, 357:224–230.

Chen, Y. Q., Nissen, P. E., Zhao, G., Zhang, H. W., and Benoni, T. (2000). Chemical composition of 90 F and G disk dwarfs. *A&AS*, 141:491–506.

Clampin, M., Ford, H. C., Bartko, F., Bely, P. Y., Broadhurst, T., Burrows, C. J., Cheng, E. S., Crocker, J. H., Franx, M., Feldman, P. D., Golimowski, D. A., Hartig, G. F., Illingworth, G., Kimble, R. A., Lesser, M. P., Miley, G. H., Postman, M., Rafal, M. D., Rosati, P., Sparks, W. B., Tsvetanov, Z., White, R. L., Sullivan, P., Volmer, P., and LaJeunesse, T. (2000). Advanced camera for surveys. In J. B. Breckinridge & P. Jakobsen, editor, *Society of Photo-Optical Instrumentation Engineers (SPIE) Conference Series*, volume 4013 of *Society of Photo-Optical Instrumentation Engineers (SPIE) Conference Series*, pages 344–351.

Close, L. M., Siegler, N., Freed, M., and Biller, B. (2003). Detection of Nine M8.0-L0.5 Binaries: The Very Low Mass Binary Population and Its Implications for Brown Dwarf and Very Low Mass Star Formation. *ApJ*, 587:407–422.

Cutri, R. M., Skrutskie, M. F., van Dyk, S., Beichman, C. A., Carpenter, J. M., Chester, T., Cambresy, L., Evans, T., Fowler, J., Gizis, J., Howard, E., Huchra, J., Jarrett, T., Kopan, E. L., Kirkpatrick, J. D., Light, R. M., Marsh, K. A., McCallon, H., Schneider,

S., Stiening, R., Sykes, M., Weinberg, M., Wheaton, W. A., Wheelock, S., and Zacarias, N. (2003). 2MASS All-Sky Catalog of Point Sources (Cutri+ 2003). *VizieR Online Data Catalog*, 2246:0.

D'Antona, F. and Mazzitelli, I. (1994). New pre-main-sequence tracks for M less than or equal to 2.5 solar mass as tests of opacities and convection model. *ApJS*, 90:467–500.

D'Antona, F. and Mazzitelli, I. (1997). Evolution of low mass stars. *Mem. Soc. Astron. Italiana*, 68:807.

Davies, R. I., Hackenberg, W., Ott, T., Eckart, A., Rabien, S., Anders, S., Hippler, S., Kasper, M., Kalas, P., Quirrenbach, A., and Glindemann, A. (1999). The science potential of ALFA: Adaptive optics with natural and laser guide stars. *A&AS*, 138:345–353.

de Geus, E. J., de Zeeuw, P. T., and Lub, J. (1989). Physical parameters of stars in the Scorpio-Centaurus OB association. *A&A*, 216:44–61.

de Zeeuw, P. T., Hoogerwerf, R., de Bruijne, J. H. J., Brown, A. G. A., and Blaauw, A. (1999). A HIPPARCOS Census of the Nearby OB Associations. *AJ*, 117:354–399.

de Zeeuw, T. and Brand, J. (1985). Photometric age determination of OB-association. In W. Boland & H. van Woerden, editor, *Birth and Evolution of Massive Stars and Stellar Groups*, volume 120 of *Astrophysics and Space Science Library*, pages 95–101.

Devillard, N. (2001). ESO C Library for an Image Processing Software Environment (eclipse). In F. R. Harnden Jr., F. A. Primini, & H. E. Payne, editor, *Astronomical Data Analysis Software and Systems X*, volume 238 of *Astronomical Society of the Pacific Conference Series*, page 525.

Donnison, J. R. (2010). The Hill stability of inclined small mass binary systems in three-body systems with special application to triple star systems, extrasolar planetary systems and Binary Kuiper Belt systems. *Planet. Space Sci.*, 58:1169–1179.

Draper, P. W. (2000). GAIA: Recent Developments. In N. Manset, C. Veillet, & D. Crabtree, editor, *Astronomical Data Analysis Software and Systems IX*, volume 216 of *Astronomical Society of the Pacific Conference Series*, page 615.

Dupuy, T. J., Liu, M. C., and Ireland, M. J. (2009). Dynamical Mass of the Substellar Benchmark Binary HD 130948BC. *ApJ*, 692:729–752.

Eggen, O. J. (1991). The IC 2391 supercluster. *AJ*, 102:2028–2040.

Eisenbeiss, T. (2011). *Optische Beobachtungen naher Isolierter Neutronensterne*. PhD thesis, University Jena.

Fruchter, A. and Sosey, M. (2009).

Furlan, E., Hartmann, L., Calvet, N., D'Alessio, P., Franco-Hernández, R., Forrest, W. J., Watson, D. M., Uchida, K. I., Sargent, B., Green, J. D., Keller, L. D., and Herter, T. L. (2006). A Survey and Analysis of Spitzer Infrared Spectrograph Spectra of T Tauri Stars in Taurus. *ApJS*, 165:568–605.

Geißler, K., Chauvin, G., and Sterzik, M. F. (2008). Mid-infrared imaging of brown dwarfs in binary systems. *A&A*, 480:193–198.

Ghez, A. M., Salim, S., Weinberg, N. N., Lu, J. R., Do, T., Dunn, J. K., Matthews, K., Morris, M. R., Yelda, S., Becklin, E. E., Kremenek, T., Milosavljevic, M., and Naiman, J. (2008). Measuring Distance and Properties of the Milky Way's Central Supermassive Black Hole with Stellar Orbits. *ApJ*, 689:1044–1062.

Girard, J. e. a. (2012).

Gizis, J. E., Kirkpatrick, J. D., Burgasser, A., Reid, I. N., Monet, D. G., Liebert, J., and Wilson, J. C. (2001). Substellar Companions to Main-Sequence Stars: No Brown Dwarf Desert at Wide Separations. *ApJ*, 551:L163–L166.

Gräfe, C., Wolf, S., Roccatagliata, V., Sauter, J., and Ertel, S. (2011). Mid-infrared observations of the transitional disks around DH Tauri, DM Tauri, and GM Aurigae. *A&A*, 533:A89.

Graves, J. E., Northcott, M. J., Roddier, F. J., Roddier, C. A., and Close, L. M. (1998). First light for Hokupa'a: 36-element curvature AO system at UH. In D. Bonaccini & R. K. Tyson, editor, *Society of Photo-Optical Instrumentation Engineers (SPIE) Conference Series*, volume 3353 of *Society of Photo-Optical Instrumentation Engineers (SPIE) Conference Series*, pages 34–43.

Grether, D. and Lineweaver, C. H. (2006). How Dry is the Brown Dwarf Desert? Quantifying the Relative Number of Planets, Brown Dwarfs, and Stellar Companions around Nearby Sun-like Stars. *ApJ*, 640:1051–1062.

Hanson, R. B., Klemola, A. R., Jones, B. F., and Monet, D. G. (2003). Lick NPM2 Catalog (Hanson+ 2003). *VizieR Online Data Catalog*, 1283:0.

Hartigan, P., Strom, K. M., and Strom, S. E. (1994). Are wide pre-main-sequence binaries coeval? *ApJ*, 427:961–977.

Hayward, T. L., Brandl, B., Pirger, B., Blacken, C., Gull, G. E., Schoenwald, J., and Houck, J. R. (2001). PHARO: A Near-Infrared Camera for the Palomar Adaptive Optics System. *PASP*, 113:105–118.

Heacox, W. D. (1999). On the Nature of Low-Mass Companions to Solar-like Stars. *ApJ*, 526:928–936.

Helling, C., Dehn, M., Woitke, P., and Hauschildt, P. H. (2008). Consistent Simulations of Substellar Atmospheres and Nonequilibrium Dust Cloud Formation. *ApJ*, 675:L105–L108.

Hodapp, K.-W., Hora, J. L., Hall, D. N. B., Cowie, L. L., Metzger, M., Irwin, E., Vural, K., Kozlowski, L. J., Cabelli, S. A., Chen, C. Y., Cooper, D. E., Bostrup, G. L., Bailey, R. B., and Kleinhans, W. E. (1996). The HAWAII Infrared Detector Arrays: testing and astronomical characterization of prototype and science-grade devices. *New A*, 1:177–196.

Hodapp, K. W., Jensen, J. B., Irwin, E. M., Yamada, H., Chung, R., Fletcher, K., Robertson, L., Hora, J. L., Simons, D. A., Mays, W., Nolan, R., Bec, M., Merrill, M., and Fowler, A. M. (2003). The Gemini Near-Infrared Imager (NIRI). *PASP*, 115:1388–1406.

Hofmann, R., Blietz, M., Duhoux, P., Eckart, A., Krabbe, A., and Rotaciuc, V. (1992). SHARP and FAST: NIR Speckle and Spectroscopy at MPE. In Ulrich, M.-H., editor, *European Southern Observatory Conference and Workshop Proceedings*, volume 42 of *European Southern Observatory Conference and Workshop Proceedings*, page 617.

Hog, E., Kuzmin, A., Bastian, U., Fabricius, C., Kuimov, K., Lindegren, L., Makarov, V. V., and Roeser, S. (1998). The TYCHO Reference Catalogue. *A&A*, 335:L65–L68.

Holman, M. J. and Wiegert, P. A. (1999). Long-Term Stability of Planets in Binary Systems. *AJ*, 117:621–628.

Hunter, J. D. (2007). Matplotlib: A 2d graphics environment. *Computing In Science & Engineering*, 9(3):90–95.

Ireland, M. J., Kraus, A., Martinache, F., Law, N., and Hillenbrand, L. A. (2011). Two Wide Planetary-mass Companions to Solar-type Stars in Upper Scorpius. *ApJ*, 726:113.

Itoh, Y., Hayashi, M., Tamura, M., Tsuji, T., Oasa, Y., Fukagawa, M., Hayashi, S. S., Naoi, T., Ishii, M., Mayama, S., Morino, J.-i., Yamashita, T., Pyo, T.-S., Nishikawa, T., Usuda, T., Murakawa, K., Suto, H., Oya, S., Takato, N., Ando, H., Miyama, S. M., Kobayashi, N., and Kaifu, N. (2005). A Young Brown Dwarf Companion to DH Tauri. *ApJ*, 620:984–993.

Itoh, Y., Tamura, M., Hayashi, S. S., Oasa, Y., Fukagawa, M., Kaifu, N., Suto, H., Murakawa, K., Doi, Y., Ebizuka, N., Naoi, T., Takami, H., Takato, N., Gaessler, W., Kanzawa, T., Hayano, Y., Kamata, Y., Saint-Jacques, D., and Iye, M. (2002). Near-Infrared Coronagraphy of the GG Tauri A Binary System. *PASJ*, 54:963–967.

Jaschek, M. (1978). Catalogue of selected spectral types in the MK system. *Bulletin d'Information du Centre de Donnees Stellaires*, 15:121.

Jones, E., Oliphant, T., Peterson, P., et al. (2001). SciPy: Open source scientific tools for Python.

Kasper, M., Looze, D. P., Hippler, S., Herbst, T., Glindemann, A., Ott, T., and Wirth, A. (2000). ALFA: Adaptive Optics for the Calar Alto Observatory Optics, Control Systems, and Performance. *Experimental Astronomy*, 10:49–73.

Kenyon, S. J., Dobrzycka, D., and Hartmann, L. (1994). A new optical extinction law and distance estimate for the Taurus-Auriga molecular cloud. *AJ*, 108:1872–1880.

Kirkpatrick, J. D. (2000). The L and T Dwarf Spectral Sequences: First Steps in Bridging the Gap Between Planets and Stars. In Griffith, C. A. and Marley, M. S., editors, *From Giant Planets to Cool Stars*, volume 212 of *Astronomical Society of the Pacific Conference Series*, page 20.

Kobayashi, N., Tokunaga, A. T., Terada, H., Goto, M., Weber, M., Potter, R., Onaka, P. M., Ching, G. K., Young, T. T., Fletcher, K., Neil, D., Robertson, L., Cook, D., Imanishi, M., and Warren, D. W. (2000). IRCS: infrared camera and spectrograph for the Subaru Telescope. In M. Iye & A. F. Moorwood, editor, *Society of Photo-Optical Instrumentation Engineers (SPIE) Conference Series*, volume 4008 of *Society of Photo-Optical Instrumentation Engineers (SPIE) Conference Series*, pages 1056–1066.

Koekemoer, A. M., Fruchter, A. S., Hook, R. N., and Hack, W. (2002). MultiDrizzle: An Integrated Pyraf Script for Registering, Cleaning and Combining Images. In S. Arribas, A. Koekemoer, & B. Whitmore, editor, *The 2002 HST Calibration Workshop : Hubble after the Installation of the ACS and the NICMOS Cooling System*, page 337.

Labadie, L., Rebolo, R., Villó, I., Pérez-Prieto, J. A., Pérez-Garrido, A., Hildebrandt, S. R., Femenía, B., Díaz-Sanchez, A., Béjar, V. J. S., Oscoz, A., López, R., Piqueras, J., and Rodríguez, L. F. (2011). High-contrast optical imaging of companions: the case of the brown dwarf binary HD 130948 BC. *A&A*, 526:A144.

Lafrenière, D., Jayawardhana, R., and van Kerkwijk, M. H. (2008). Direct Imaging and Spectroscopy of a Planetary-Mass Candidate Companion to a Young Solar Analog. *ApJ*, 689:L153–L156.

Lafrenière, D., Jayawardhana, R., and van Kerkwijk, M. H. (2010). The Directly Imaged Planet Around the Young Solar Analog 1RXS J160929.1 - 210524: Confirmation of Common Proper Motion, Temperature, and Mass. *ApJ*, 719:497–504.

Lagage, P. O., Pel, J. W., Authier, M., Belorgey, J., Claret, A., Doucet, C., Dubreuil, D., Durand, G., Elswijk, E., Girardot, P., Käufl, H. U., Kroes, G., Lortholary, M., Lussignol, Y., Marchesi, M., Pantin, E., Peletier, R., Pirard, J.-F., Pragt, J., Rio, Y., Schoenmaker, T., Siebenmorgen, R., Silber, A., Smette, A., Sterzik, M., and Veyssiere, C. (2004).

Successful Commissioning of VISIR: The Mid-Infrared VLT Instrument. *The Messenger*, 117:12–16.

Lenzen, R., Bizenberger, P., Salm, N., and Storz, C. (1998). Omega Cass: a new multimode NIR-imager/spectrometer for the Calar Alto Observatory. In A. M. Fowler, editor, *Society of Photo-Optical Instrumentation Engineers (SPIE) Conference Series*, volume 3354 of *Society of Photo-Optical Instrumentation Engineers (SPIE) Conference Series*, pages 493–499.

Lenzen, R., Hartung, M., Brandner, W., Finger, G., Hubin, N. N., Lacombe, F., Lagrange, A.-M., Lehnert, M. D., Moorwood, A. F. M., and Mouillet, D. (2003). NAOS-CONICA first on sky results in a variety of observing modes. In M. Iye & A. F. M. Moorwood, editor, *Society of Photo-Optical Instrumentation Engineers (SPIE) Conference Series*, volume 4841 of *Society of Photo-Optical Instrumentation Engineers (SPIE) Conference Series*, pages 944–952.

Levenberg, K. (1944). A Method for the Solution of Certain Non-Linear Problems in Least Squares. *Quarterly of Applied Mathematics*, 2:164–168.

Lucas, P. W. and Roche, P. F. (2000). A population of very young brown dwarfs and free-floating planets in Orion. *MNRAS*, 314:858–864.

Luhman, K. L., Rieke, G. H., Young, E. T., Cotera, A. S., Chen, H., Rieke, M. J., Schneider, G., and Thompson, R. I. (2000). The Initial Mass Function of Low-Mass Stars and Brown Dwarfs in Young Clusters. *ApJ*, 540:1016–1040.

Marois, C., Lafrenière, D., Doyon, R., Macintosh, B., and Nadeau, D. (2006). Angular Differential Imaging: A Powerful High-Contrast Imaging Technique. *ApJ*, 641:556–564.

Martin, E. L., Basri, G., Delfosse, X., and Forveille, T. (1997). Keck HIRES spectra of the brown dwarf DENIS-P J1228.2-1547. *A&A*, 327:L29–L32.

Mason, B. D., Wycoff, G. L., Hartkopf, W. I., Douglass, G. G., and Worley, C. E. (2001). The 2001 US Naval Observatory Double Star CD-ROM. I. The Washington Double Star Catalog. *AJ*, 122:3466–3471.

Mayama, S., Tamura, M., Hayashi, M., Itoh, Y., Fukagawa, M., Suto, H., Ishii, M., Murakawa, K., Oasa, Y., Hayashi, S. S., Yamashita, T., Morino, J., Oya, S., Naoi, T., Pyo, T.-S., Nishikawa, T., Kudo, T., Usuda, T., Ando, H., Miyama, S. M., and Kaifu, N. (2006). Subaru Near Infrared Coronagraphic Images of T Tauri. *PASJ*, 58:375–382.

Mayor, M. and Queloz, D. (1995). A Jupiter-mass companion to a solar-type star. *Nature*, 378:355–359.

McLean, I. S., Becklin, E. E., Bendiksen, O., Brims, G., Canfield, J., Figer, D. F., Graham, J. R., Hare, J., Lacayanga, F., Larkin, J. E., Larson, S. B., Levenson, N., Magnone, N., Teplitz, H., and Wong, W. (1998). Design and development of NIRSPEC: a near-infrared echelle spectrograph for the Keck II telescope. In Fowler, A. M., editor, *Society of Photo-Optical Instrumentation Engineers (SPIE) Conference Series*, volume 3354 of *Society of Photo-Optical Instrumentation Engineers (SPIE) Conference Series*, pages 566–578.

McLean, I. S. and Sprayberry, D. (2003). Instrumentation at the Keck observatory. In Iye, M. and Moorwood, A. F. M., editors, *Society of Photo-Optical Instrumentation Engineers (SPIE) Conference Series*, volume 4841 of *Society of Photo-Optical Instrumentation Engineers (SPIE) Conference Series*, pages 1–6.

Metchev, S. A. (2006). *Brown dwarf companions to young solar analogs: An adaptive optics survey using Palomar and Keck*. PhD thesis, California Institute of Technology, California, USA.

Metchev, S. A. and Hillenbrand, L. A. (2006). HD 203030B: An Unusually Cool Young Substellar Companion near the L/T Transition. *ApJ*, 651:1166–1176.

Metchev, S. A. and Hillenbrand, L. A. (2009). Survey of young solar analogs (Metchev+, 2009). *VizieR Online Data Catalog*, 218:10062.

Monet, D. G., Levine, S. E., Canzian, B., Ables, H. D., Bird, A. R., Dahn, C. C., Guetter, H. H., Harris, H. C., Henden, A. A., Leggett, S. K., Levison, H. F., Luginbuhl, C. B., Martini, J., Monet, A. K. B., Munn, J. A., Pier, J. R., Rhodes, A. R., Riepe, B., Sell, S., Stone, R. C., Vrba, F. J., Walker, R. L., Westerhout, G., Brucato, R. J., Reid, I. N., Schoening, W., Hartley, M., Read, M. A., and Tritton, S. B. (2003). The USNO-B Catalog. *AJ*, 125:984–993.

Montenbruck, O. (2005). *Grundlagen der Ephemeridenrechnung*.

Montes, D., López-Santiago, J., Gálvez, M. C., Fernández-Figueroa, M. J., De Castro, E., and Cornide, M. (2001). Late-type members of young stellar kinematic groups - I. Single stars. *MNRAS*, 328:45–63.

Moorwood, A., Cuby, J.-G., and Lidman, C. (1998). SOFI sees first light at the NTT. *The Messenger*, 91:9–13.

Motohara, K., Iwamuro, F., Maihara, T., Oya, S., Tsukamoto, H., Imanishi, M., Terada, H., Goto, M., Iwai, J., Tanabe, H., Hata, R., Taguchi, T., and Harashima, T. (2002). CISCO: Cooled Infrared Spectrograph and Camera for OHS on the Subaru Telescope. *PASJ*, 54:315–325.

Mugrauer, M., Neuhäuser, R., Guenther, E. W., Hatzes, A. P., Huélamo, N., Fernández, M., Ammler, M., Retzlaff, J., König, B., Charbonneau, D., Jayawardhana, R., and Brandner,

W. (2004). HD 77407 and GJ 577: Two new young stellar binaries. Detected with the Calar Alto Adaptive Optics system ALFA. *A&A*, 417:1031–1038.

Mugrauer, M., Vogt, N., Neuhäuser, R., and Schmidt, T. O. B. (2010). Direct detection of a substellar companion to the young nearby star PZ Telescopii. *A&A*, 523:L1.

Murakawa, K., Suto, H., Tamura, M., Kaifu, N., Takami, H., Takato, N., Oya, S., Hayano, Y., Gaessler, W., and Kamata, Y. (2004). CIAO: Coronagraphic Imager with Adaptive Optics on the Subaru Telescope. *PASJ*, 56:509–519.

Nelan, E. P., Lupie, O. L., McArthur, B., Benedict, G. F., Franz, O. G., Wasserman, L. H., Abramowicz-Reed, L., Makidon, R. B., and Nagel, L. (1998). Fine guidance sensors aboard the Hubble Space Telescope: the scientific capabilities of these interferometers. In Reasenberg, R. D., editor, *Society of Photo-Optical Instrumentation Engineers (SPIE) Conference Series*, volume 3350 of *Society of Photo-Optical Instrumentation Engineers (SPIE) Conference Series*, pages 237–247.

Neuhäuser, R., Errmann, R., Berndt, A., Maciejewski, G., Takahashi, H., Chen, W. P., Dimitrov, D. P., Pribulla, T., Nikogossian, E. H., Jensen, E. L. N., Marschall, L., Wu, Z.-Y., Kellerer, A., Walter, F. M., Briceño, C., Chini, R., Fernandez, M., Raetz, S., Torres, G., Latham, D. W., Quinn, S. N., Niedzielski, A., Bukowiecki, Ł., Nowak, G., Tomov, T., Tachihara, K., Hu, S. C.-L., Hung, L. W., Kjurkchieva, D. P., Radeva, V. S., Mihov, B. M., Slavcheva-Mihova, L., Bozhinova, I. N., Budaj, J., Vaňko, M., Kundra, E., Hambálek, Ľ., Krushevska, V., Movsessian, T., Harutyunyan, H., Downes, J. J., Hernandez, J., Hoffmeister, V. H., Cohen, D. H., Abel, I., Ahmad, R., Chapman, S., Eckert, S., Goodman, J., Guerard, A., Kim, H. M., Koontharana, A., Sokol, J., Trinh, J., Wang, Y., Zhou, X., Redmer, R., Kramm, U., Nettelmann, N., Mugrauer, M., Schmidt, J., Moualla, M., Ginski, C., Marka, C., Adam, C., Seeliger, M., Baar, S., Roell, T., Schmidt, T. O. B., Trepl, L., Eisenbeiß, T., Fiedler, S., Tetzlaff, N., Schmidt, E., Hohle, M. M., Kitze, M., Chakrova, N., Gräfe, C., Schreyer, K., Hambaryan, V. V., Broeg, C. H., Koppenhoefer, J., and Pandey, A. K. (2011a). The Young Exoplanet Transit Initiative (YETI). *Astronomische Nachrichten*, 332:547.

Neuhäuser, R., Ginski, C., Schmidt, T. O. B., and Mugrauer, M. (2011b). Further deep imaging of HR 7329 A (η Tel A) and its brown dwarf companion B. *MNRAS*, 416:1430–1435.

Neuhäuser, R. and Guenther, E. W. (2004). Infrared spectroscopy of a brown dwarf companion candidate near the young star GSC 08047-00232 in Horologium. *A&A*, 420:647–653.

Neuhäuser, R., Guenther, E. W., Alves, J., Huélamo, N., Ott, T., and Eckart, A. (2003). An infrared imaging search for low-mass companions to members of the young nearby β Pic and Tucana/Horologium associations. *Astronomische Nachrichten*, 324:535–542.

Neuhäuser, R., Guenther, E. W., Wuchterl, G., Mugrauer, M., Bedalov, A., and Hauschildt, P. H. (2005). Evidence for a co-moving sub-stellar companion of GQ Lup. *A&A*, 435:L13–L16.

Neuhäuser, R., Mugrauer, M., Fukagawa, M., Torres, G., and Schmidt, T. (2007). Direct detection of exoplanet host star companion γ Cep B and revised masses for both stars and the sub-stellar object. *A&A*, 462:777–780.

Neuhäuser, R., Mugrauer, M., Seifahrt, A., Schmidt, T. O. B., and Vogt, N. (2008). Astrometric and photometric monitoring of GQ Lupi and its sub-stellar companion. *A&A*, 484:281–291.

Neuhäuser, R., Schmidt, T. O. B., Hambaryan, V. V., and Vogt, N. (2010). Orbital motion of the young brown dwarf companion TWA 5 B. *A&A*, 516:A112.

Oscoz, A., Rebolo, R., López, R., Pérez-Garrido, A., Pérez, J. A., Hildebrandt, S., Rodríguez, L. F., Piqueras, J. J., Villó, I., González, J. M., Barrena, R., Gómez, G., García, A., Montañés, P., Rosenberg, A., Cadavid, E., Calcines, A., Díaz-Sánchez, A., Kohley, R., Martín, Y., Peñate, J., and Sánchez, V. (2008). FastCam: a new lucky imaging instrument for medium-sized telescopes. In *Society of Photo-Optical Instrumentation Engineers (SPIE) Conference Series*, volume 7014 of *Society of Photo-Optical Instrumentation Engineers (SPIE) Conference Series*.

Pecaut, M. J., Mamajek, E. E., and Bubar, E. J. (2012). A Revised Age for Upper Scorpius and the Star Formation History among the F-type Members of the Scorpius-Centaurus OB Association. *ApJ*, 746:154.

Pollacco, D. L., Skillen, I., Collier Cameron, A., Christian, D. J., Hellier, C., Irwin, J., Lister, T. A., Street, R. A., West, R. G., Anderson, D., Clarkson, W. I., Deeg, H., Enoch, B., Evans, A., Fitzsimmons, A., Haswell, C. A., Hodgkin, S., Horne, K., Kane, S. R., Keenan, F. P., Maxted, P. F. L., Norton, A. J., Osborne, J., Parley, N. R., Ryans, R. S. I., Smalley, B., Wheatley, P. J., and Wilson, D. M. (2006). The WASP Project and the SuperWASP Cameras. *PASP*, 118:1407–1418.

Potter, D., Martín, E. L., Cushing, M. C., Baudoz, P., Brandner, W., Guyon, O., and Neuhäuser, R. (2002). Hokupa'a-Gemini Discovery of Two Ultracool Companions to the Young Star HD 130948. *ApJ*, 567:L133–L136.

Preibisch, T., Brown, A. G. A., Bridges, T., Guenther, E., and Zinnecker, H. (2002). Exploring the Full Stellar Population of the Upper Scorpius OB Association. *AJ*, 124:404–416.

Preibisch, T. and Zinnecker, H. (1999). The History of Low-Mass Star Formation in the Upper Scorpius OB Association. *AJ*, 117:2381–2397.

Ribas, I. and Miralda-Escudé, J. (2007). The eccentricity-mass distribution of exoplanets: signatures of different formation mechanisms? *A&A*, 464:779–785.

Richardson, E. H., Fletcher, J. M., Morbey, C. L., Oschmann, J. M., and Pazder, J. S. (1998). Optical design of Gemini ALTAIR. In D. Bonaccini & R. K. Tyson, editor, *Society of Photo-Optical Instrumentation Engineers (SPIE) Conference Series*, volume 3353 of *Society of Photo-Optical Instrumentation Engineers (SPIE) Conference Series*, pages 600–610.

Rieke, G. H., Young, E. T., Engelbracht, C. W., Kelly, D. M., Low, F. J., Haller, E. E., Beeman, J. W., Gordon, K. D., Stansberry, J. A., Misselt, K. A., Cadien, J., Morrison, J. E., Rivlis, G., Latter, W. B., Noriega-Crespo, A., Padgett, D. L., Stapelfeldt, K. R., Hines, D. C., Egami, E., Muzerolle, J., Alonso-Herrero, A., Blaylock, M., Dole, H., Hinz, J. L., Le Floc'h, E., Papovich, C., Pérez-González, P. G., Smith, P. S., Su, K. Y. L., Bennett, L., Frayer, D. T., Henderson, D., Lu, N., Masci, F., Pesenson, M., Rebull, L., Rho, J., Keene, J., Stolovy, S., Wachter, S., Wheaton, W., Werner, M. W., and Richards, P. L. (2004). The Multiband Imaging Photometer for Spitzer (MIPS). *ApJS*, 154:25–29.

Rigaut, F. (2000). Astrometry with hokupa'a/quirc. http://www.gemini.edu/sciops/instruments/uhaos/uhaosDPAstrom.html.

Rousset, G., Lacombe, F., Puget, P., Hubin, N. N., Gendron, E., Fusco, T., Arsenault, R., Charton, J., Feautrier, P., Gigan, P., Kern, P. Y., Lagrange, A.-M., Madec, P.-Y., Mouillet, D., Rabaud, D., Rabou, P., Stadler, E., and Zins, G. (2003). NAOS, the first AO system of the VLT: on-sky performance. In P. L. Wizinowich & D. Bonaccini, editor, *Society of Photo-Optical Instrumentation Engineers (SPIE) Conference Series*, volume 4839 of *Society of Photo-Optical Instrumentation Engineers (SPIE) Conference Series*, pages 140–149.

Schmidt, T. O. B., Neuhäuser, R., Seifahrt, A., Vogt, N., Bedalov, A., Helling, C., Witte, S., and Hauschildt, P. H. (2008). Direct evidence of a sub-stellar companion around CT Chamaeleontis. *A&A*, 491:311–320.

Schneider, J., Dedieu, C., Le Sidaner, P., Savalle, R., and Zolotukhin, I. (2011). Defining and cataloging exoplanets: the exoplanet.eu database. *A&A*, 532:A79.

Scholz, R.-D. (2010). ULAS J141623.94+134836.3 - a faint common proper motion companion of a nearby L dwarf. Serendipitous discovery of a cool brown dwarf in UKIDSS DR6. *A&A*, 510:L8.

Serabyn, E., Mawet, D., Bloemhof, E., Haguenauer, P., Mennesson, B., Wallace, K., and Hickey, J. (2009). Imaging Faint Brown Dwarf Companions Close to Bright Stars with a Small, Well-corrected Telescope Aperture. *ApJ*, 696:40–46.

Siess, L., Forestini, M., and Dougados, C. (1997). Synthetic Hertzsprung-Russell diagrams of open clusters. $A\&A$, 324:556–565.

Simon, M., Close, L. M., and Beck, T. L. (1999). Adaptive Optics Imaging of the Orion Trapezium Cluster. AJ, 117:1375–1386.

Skrutskie, M. F., Cutri, R. M., Stiening, R., Weinberg, M. D., Schneider, S., Carpenter, J. M., Beichman, C., Capps, R., Chester, T., Elias, J., Huchra, J., Liebert, J., Lonsdale, C., Monet, D. G., Price, S., Seitzer, P., Jarrett, T., Kirkpatrick, J. D., Gizis, J. E., Howard, E., Evans, T., Fowler, J., Fullmer, L., Hurt, R., Light, R., Kopan, E. L., Marsh, K. A., McCallon, H. L., Tam, R., Van Dyk, S., and Wheelock, S. (2006). The Two Micron All Sky Survey (2MASS). AJ, 131:1163–1183.

Spiegel, D. S., Burrows, A., and Milsom, J. A. (2011). The Deuterium-burning Mass Limit for Brown Dwarfs and Giant Planets. ApJ, 727:57.

Stelzer, B. and Neuhäuser, R. (2000). X-ray emission from young stars in the Tucanae association. $A\&A$, 361:581–593.

Strassmeier, K., Washuettl, A., Granzer, T., Scheck, M., and Weber, M. (2000). The Vienna-KPNO search for Doppler-imaging candidate stars. I. A catalog of stellar-activity indicators for 1058 late-type Hipparcos stars. $A\&AS$, 142:275–311.

Struve, O. (1952). Proposal for a project of high-precision stellar radial velocity work. *The Observatory*, 72:199–200.

Sumi, T., Kamiya, K., Bennett, D. P., Bond, I. A., Abe, F., Botzler, C. S., Fukui, A., Furusawa, K., Hearnshaw, J. B., Itow, Y., Kilmartin, P. M., Korpela, A., Lin, W., Ling, C. H., Masuda, K., Matsubara, Y., Miyake, N., Motomura, M., Muraki, Y., Nagaya, M., Nakamura, S., Ohnishi, K., Okumura, T., Perrott, Y. C., Rattenbury, N., Saito, T., Sako, T., Sullivan, D. J., Sweatman, W. L., Tristram, P. J., Udalski, A., Szymański, M. K., Kubiak, M., Pietrzyński, G., Poleski, R., Soszyński, I., Wyrzykowski, Ł., Ulaczyk, K., and Microlensing Observations in Astrophysics (MOA) Collaboration (2011). Unbound or distant planetary mass population detected by gravitational microlensing. *Nature*, 473:349–352.

Swenson, F. J., Faulkner, J., Rogers, F. J., and Iglesias, C. A. (1994). The Hyades lithium problem revisited. ApJ, 425:286–302.

Takami, H., Takato, N., Hayano, Y., Iye, M., Oya, S., Kamata, Y., Kanzawa, T., Minowa, Y., Otsubo, M., Nakashima, K., Gaessler, W., and Saint-Jacques, D. (2004). Performance of Subaru Cassegrain Adaptive Optics System. $PASJ$, 56:225–234.

Thalmann, C., Carson, J., Janson, M., Goto, M., McElwain, M., Egner, S., Feldt, M., Hashimoto, J., Hayano, Y., Henning, T., Hodapp, K. W., Kandori, R., Klahr, H., Kudo,

T., Kusakabe, N., Mordasini, C., Morino, J.-I., Suto, H., Suzuki, R., and Tamura, M. (2009). Discovery of the Coldest Imaged Companion of a Sun-like Star. *ApJ*, 707:L123–L127.

Torres, C. A. O., da Silva, L., Quast, G. R., de la Reza, R., and Jilinski, E. (2000). A New Association of Post-T Tauri Stars near the Sun. *AJ*, 120:1410–1425.

Torres, C. A. O., Quast, G. R., da Silva, L., de La Reza, R., Melo, C. H. F., and Sterzik, M. (2006). Search for associations containing young stars (SACY). I. Sample and searching method. *A&A*, 460:695–708.

Torres, C. A. O., Quast, G. R., de La Reza, R., da Silva, L., and Melo, C. H. F. (2001). The Great Austral Nearby Young Association. In R. Jayawardhana & T. Greene, editor, *Young Stars Near Earth: Progress and Prospects*, volume 244 of *Astronomical Society of the Pacific Conference Series*, page 43.

Torres, C. A. O., Quast, G. R., Melo, C. H. F., and Sterzik, M. F. (2008). *Young Nearby Loose Associations*, page 757.

Trauger, J. T., Ballester, G. E., Burrows, C. J., Casertano, S., Clarke, J. T., Crisp, D., Evans, R. W., Gallagher, III, J. S., Griffiths, R. E., Hester, J. J., Hoessel, J. G., Holtzman, J. A., Krist, J. E., Mould, J. R., Scowen, P. A., Stapelfeldt, K. R., Watson, A. M., and Westphal, J. A. (1994). The on-orbit performance of WFPC2. *ApJ*, 435:L3–L6.

Troy, M., Dekany, R. G., Brack, G., Oppenheimer, B. R., Bloemhof, E. E., Trinh, T., Dekens, F. G., Shi, F., Hayward, T. L., and Brandl, B. (2000). Palomar adaptive optics project: status and performance. In Wizinowich, P. L., editor, *Society of Photo-Optical Instrumentation Engineers (SPIE) Conference Series*, volume 4007 of *Society of Photo-Optical Instrumentation Engineers (SPIE) Conference Series*, pages 31–40.

Tsuji, T., Nakajima, T., and Yanagisawa, K. (2004). Dust in the Photospheric Environment. II. Effect on the Near-Infrared Spectra of L and T Dwarfs. *ApJ*, 607:511–529.

Ubeda, L. e. a. (2011).

Unsöld, A. and Baschek, B. (1988). *Der neue Kosmos.*

van Leeuwen, F. (2007). Validation of the new Hipparcos reduction. *A&A*, 474:653–664.

Warmels, R. H. (1992). The ESO–MIDAS System. In D. M. Worrall, C. Biemesderfer, & J. Barnes, editor, *Astronomical Data Analysis Software and Systems I*, volume 25 of *Astronomical Society of the Pacific Conference Series*, page 115.

Watson, C., Corn, T., Churchwell, E. B., Babler, B. L., Povich, M. S., Meade, M. R., and Whitney, B. A. (2009). IR Dust Bubbles. II. Probing the Detailed Structure and Young Massive Stellar Populations of Galactic H II Regions. *ApJ*, 694:546–555.

White, R. J. and Ghez, A. M. (2001). Observational Constraints on the Formation and Evolution of Binary Stars. *ApJ*, 556:265–295.

Wizinowich, P., Acton, D. S., Shelton, C., Stomski, P., Gathright, J., Ho, K., Lupton, W., Tsubota, K., Lai, O., Max, C., Brase, J., An, J., Avicola, K., Olivier, S., Gavel, D., Macintosh, B., Ghez, A., and Larkin, J. (2000). First Light Adaptive Optics Images from the Keck II Telescope: A New Era of High Angular Resolution Imagery. *PASP*, 112:315–319.

Woitas, J., Köhler, R., and Leinert, C. (2001). Orbital motion in T Tauri binary systems. *A&A*, 369:249–262.

Zacharias, N., Finch, C., Girard, T., Hambly, N., Wycoff, G., Zacharias, M. I., Castillo, D., Corbin, T., Divittorio, M., Dutta, S., Gaume, R., Gauss, S., Germain, M., Hall, D., Hartkopf, W., Hsu, D., Holdenried, E., Makarov, V., Martinez, M., Mason, B., Monet, D., Rafferty, T., Rhodes, A., Siemers, T., Smith, D., Tilleman, T., Urban, S., Wieder, G., Winter, L., and Young, A. (2009). Third U.S. Naval Observatory CCD Astrograph Catalog (UCAC3). *VizieR Online Data Catalog*, 1315:0.

Zacharias, N., Urban, S. E., Zacharias, M. I., Wycoff, G. L., Hall, D. M., Monet, D. G., and Rafferty, T. J. (2004). The Second US Naval Observatory CCD Astrograph Catalog (UCAC2). *AJ*, 127:3043–3059.

Zuckerman, B., Song, I., and Webb, R. A. (2001). Tucana Association. *ApJ*, 559:388–394.

Zuckerman, B. and Webb, R. A. (2000). Identification of a Nearby Stellar Association in theHipparcos Catalog: Implications for Recent, Local Star Formation. *ApJ*, 535:959–964.

A   Python Programs

A.1   PSF Subtraction

```python
#————————————————————————
#modul − import
#————————————————————————

import numpy as np
import scipy
from scipy import ndimage as nd
from scipy import signal
import pyfits
import math
import matplotlib
import os
import random as rn
from scipy import *
from pylab import *


#————————————————————————
#functions for gauss − subtraction
#————————————————————————

def gauss_kern(size, sizey=None):
    """ Returns a normalized 2D gauss kernel array for convolutions """
    size = int(size)
    if not sizey:
        sizey = size
    else:
        sizey = int(sizey)
    x, y = mgrid[−size:size+1, −sizey:sizey+1]
    g = exp(−(x**2/float(size)+y**2/float(sizey)))
    return g / g.sum()

def blur_image(im, n, ny=None) :
    """ blurs the image by convolving with a gaussian kernel of typical
        size n. The optional keyword argument ny allows for a different
        size in the y direction.
    """
    g = gauss_kern(n, sizey=ny)
    improc = signal.convolve(im,g, mode='same')
    return(improc)

def subtract_gaussian_2(pic,out,n,ny=None):
```

```python
    """convolves image with gaussian of size n (and optional different ny
        in y)
      then subtracts it from original image and saves result in new fits
          file
    """
    file = pyfits.open(pic)
    scidata = file[0].data

    blurred = blur_image(scidata,n,ny)
    print shape(scidata)
    print shape(blurred)
    #subtracted = scidata[n:-n,n:-n] - blurred
    subtracted = scidata - blurred

    hdu = pyfits.PrimaryHDU(subtracted)
    hdu.writeto(out)

    return


def subtract_gaussian_folder(path,n,ny=None):
    listing = os.listdir(path)
    for infile in listing:
        subtract_gaussian_2(path + "\\" + infile , path + "\\" + infile.
            strip('.fits') + "_psf_subtracted_" + str(n) + ".fits",n,ny)
    return


#----------------------------------
#functions for rotation - subtraction
#----------------------------------


def rotation_return_data(pic,pangle,x,y):
    print "entered rotation return data"
    file = pyfits.open(pic)
    scidata = file[0].data
    header = file[0].header

    xcenter = header["naxis1"]
    xcenter = (xcenter) / 2 #+ 0.5
    ycenter = header["naxis2"]
    ycenter = (ycenter) / 2 #+ 0.5

    shift_x = xcenter - x
    shift_y = ycenter - y

    #shifts werden durchgefuehrt - Stern wird zentriert:
    centered = scidata
```

115

```
        centered = nd.shift(scidata, [shift_y,shift_x], output_type=None,
            output=None, order=3, mode='constant', cval=0.0, prefilter=True)

        #rotationen werden durchgefuehrt − zentrierter stern wird rotiert und
            abgezogen:
        diff_images = []
        print "start rotation"
        rot_angles = arange(0,360,pangle)
        for angle in rot_angles:
            rotated = nd.rotate(centered, angle, axes=(−1, −2), reshape=False
                , output_type=None, output=None, order=3, mode='constant',
                cval=0.0, prefilter=True)
            diff = centered − rotated
            diff_images.append(diff)

        #average:

        average = centered − centered
        i = 0

        for data in diff_images:
            average += data
            i += 1
        average = average / i
        print "about to exit"
        return average,shift_x,shift_y

def random_normal(x,y,sigma):
    x = rn.gauss(x,sigma)
    y = rn.gauss(y,sigma)
    return x,y



def rotation_mc(pic,pangle,x_first,y_first,boxsize,NoR):

    noise_array = []
    peak_array = []
    peak_abs_array = []
    x_array = []
    y_array = []
    shift_x =[]
    shift_y =[]

    x_array.append(x_first)
    y_array.append(y_first)

    for j in range(0,NoR,1):
        print "random run " + str(j)
```

```
        x_array.append(random_normal(x_first,y_first,boxsize)[0])
        y_array.append(random_normal(x_first,y_first,boxsize)[1])


path = os.path.dirname(pic)
coordinate_file = open(os.path.join(path,"coordinates.txt"),"w")
peak_file = open(os.path.join(path,"peak.txt"),"w")
peak_abs_file = open(os.path.join(path,"abs_peak.txt"),"w")
noise_file = open(os.path.join(path,"noise.txt"),"w")


for i in range(0,NoR+1,1):
    print i
    rotated,shiftx,shifty = rotation_return_data(pic,pangle,x_array[i
        ],y_array[i])
    print "rotation_complete"
    noise = np.std(rotated[y_first+shifty-boxsize:y_first+shifty+
        boxsize,x_first+shiftx-boxsize:x_first+shiftx+boxsize])
    peak = np.amax(rotated[y_first+shifty-boxsize:y_first+shifty+
        boxsize,x_first+shiftx-boxsize:x_first+shiftx+boxsize])
    noise_array.append(noise)
    shift_x.append(shiftx)
    shift_y.append(shifty)
    peak_array.append(peak)
    peak_abs_array.append(abs(peak))
    coordinate_file.writelines(str(x_array[i]) + "," + str(y_array[i
        ]) + "\n")
    peak_file.writelines(str(peak) + "\n")
    peak_abs_file.writelines(str(abs(peak)) + "\n")
    noise_file.writelines(str(noise) + "\n")


#minimum noise:
print "coordinates␣with␣minimal␣noise:"
print "——————————————————————————————"
print x_array[noise_array.index(min(noise_array))], y_array[
    noise_array.index(min(noise_array))]
print shift_x[noise_array.index(min(noise_array))], shift_y[
    noise_array.index(min(noise_array))]
print "\n"


#minimum peak:
print "coordinates␣with␣minimal␣peak:"
print "——————————————————————————————"
print x_array[peak_array.index(min(peak_array))], y_array[peak_array.
    index(min(peak_array))]
print shift_x[peak_array.index(min(peak_array))], shift_y[peak_array.
    index(min(peak_array))]
print "\n"


#minimum absolute peak:
```

117

```
print "coordinates_with_minimal_absolute_peak:"
print "————————————————————————————"
print x_array[peak_abs_array.index(min(peak_abs_array))], y_array[
    peak_abs_array.index(min(peak_abs_array))]
print shift_x[peak_abs_array.index(min(peak_abs_array))], shift_y[
    peak_abs_array.index(min(peak_abs_array))]

rotation_mk2(pic,pangle,"min_noise.fits",x_array[noise_array.index(
    min(noise_array))], y_array[noise_array.index(min(noise_array))])
rotation_mk2(pic,pangle,"min_peak.fits",x_array[peak_array.index(min(
    peak_array))], y_array[peak_array.index(min(peak_array))])
rotation_mk2(pic,pangle,"min_abs_peak.fits", x_array[peak_abs_array.
    index(min(peak_abs_array))], y_array[peak_abs_array.index(min(
    peak_abs_array))])

coordinate_file.close()
peak_file.close()
peak_abs_file.close()
noise_file.close()


return

#————————————————————————————
#functions for direct-subtraction
#————————————————————————————

def subtract(path,pic1,x1,y1,pic2,x2,y2):
    file1 = pyfits.open(path + "\\" + pic1)
    scidata1 = file1[0].data
    file2 = pyfits.open(path + "\\" + pic2)
    scidata2 = file2[0].data

    #Bilder alignen:
    shiftx = x1 - x2
    shifty = y1 - y2
    scidata2_shifted = nd.shift(scidata2, [shifty,shiftx], output_type=
        None, output=None, order=3, mode='constant', cval=0.0, prefilter=
        True)

    #peakwerte zum skalieren ermitteln:

    boxsize = 2

    peak1 = np.amax(scidata1[int(y1)-1-boxsize:int(y1)-1+boxsize, int(x1)
        -1-boxsize:int(x1)-1+boxsize])
    peak2 = np.amax(scidata2_shifted[int(y1)-1-boxsize:int(y1)-1+boxsize,
        int(x1)-1-boxsize:int(x1)-1+boxsize])
```

```
        print peak1
        print peak2

        # normieren :

        scidata2_shifted_norm = scidata2_shifted * ( peak1/peak2 )

        # abziehen :

        subtracted = scidata1 - scidata2_shifted_norm

        #schreiben :

        hdu = pyfits . PrimaryHDU ( subtracted )
        hdu . writeto ( path + "\\" + pic1 . strip ( " . fits " ) + "_minus_" + pic2 )


        return
```

A.2   Astrometric Measurements

```
#————————————————————————
#modul - import
#————————————————————————

from __future__ import division
import numpy as np
import scipy
import pyfits
import math
import matplotlib
import os
from scipy import ndimage
from scipy import *
from pylab import *


#————————————————————————
#functions for centre of light measurement
#————————————————————————

def give_Background ( scidata , startx , starty , boxsize ) :
    average_bg_down = np . average ( scidata [ starty -2*boxsize : starty+1-
        boxsize , startx -boxsize : startx+1+boxsize ] )
    average_stddev_down = np . std ( scidata [ starty -2*boxsize : starty+1-
        boxsize , startx -boxsize : startx+1+boxsize ] )
```

119

```
average_bg_up = np.average(scidata[starty+boxsize:starty+1+2*boxsize,
    startx-boxsize:startx+1+boxsize])
average_stddev_up = np.std(scidata[starty+boxsize:starty+1+2*boxsize,
    startx-boxsize:startx+1+boxsize])
average_bg_left = np.average(scidata[starty-boxsize:starty+1+boxsize,
    startx-2*boxsize:startx+1-boxsize])
average_stddev_left = np.std(scidata[starty-boxsize:starty+1+boxsize,
    startx-2*boxsize:startx+1-boxsize])
average_bg_right = np.average(scidata[starty-boxsize:starty+1+boxsize
    ,startx+boxsize:startx+1+2*boxsize])
average_stddev_right = np.std(scidata[starty-boxsize:starty+1+boxsize
    ,startx+boxsize:startx+1+2*boxsize])

average_BG = (average_bg_down + average_bg_up + average_bg_left +
    average_bg_right)/4
average_stddev = (average_stddev_down + average_stddev_up +
    average_stddev_left + average_stddev_right)/4

return average_BG, average_stddev

def center_of_light_3(pic, startx, starty, boxsize):

    startx = startx - 1
    starty = starty - 1

    image = pyfits.open(pic)
    scidata = image[0].data

    # Setze Bild Minimum auf 0:

    if np.nanmin(scidata) < 0:
        constant = abs(np.nanmin(scidata))
        scidata = scidata + abs(np.nanmin(scidata))

    # Messe Hintergrund und Standardabweichung:

    print "Background and noise measurement..."

    BG = []
    stddev = []

    for p in range(0,6):
        BG.append(give_Background(scidata, startx, starty, boxsize + p)[0])
        stddev.append(give_Background(scidata, startx, starty, boxsize + p)
            [1])

    average_stddev = np.average(np.array(stddev))
```

```
# Identifiziere Quellenpixel und setze alle anderen Pixel 0 ... dann
    messe :

print "Identify source pixels and measure ... "

x_range = int(scidata.shape[1])
y_range = int(scidata.shape[0])

measurement_x = []
measurement_y = []

scidata_save = scidata

for d in range(0,len(BG)):
    scidata = scidata_save
    for i in range(0,y_range):
        for j in range(0,x_range):
            if scidata[i,j] < (BG[d] + 3*stddev[d]):
                scidata[i,j] = 0

    scidata = remove_single_pixels(scidata)
    coords = ndimage.measurements.center_of_mass(scidata[starty-
        boxsize+d:starty+1+boxsize+d,startx-boxsize+d:startx+1+boxsize
        +d])
    measurement_x.append(coords[1] + (startx-boxsize+d))
    measurement_y.append(coords[0] + (starty-boxsize+d))

x_result = np.average(np.array(measurement_x))
y_result = np.average(np.array(measurement_y))

#Berechnung der Fehler:
#Uncertainty by Boxsize:

x_error_box = np.std(np.array(measurement_x))
y_error_box = np.std(np.array(measurement_y))

#Uncertainty by BG noise:

scidata = scidata - constant

for i in range(0,y_range):
    for j in range(0,x_range):
        if scidata[i,j] < 0:
            scidata[i,j] = 0

sum_pixelvalues = np.sum(scidata[starty-boxsize:starty+1+boxsize,
    startx-boxsize:startx+1+boxsize])
sum_normal = sum_pixelvalues
```

```
        x_error = 0
        y_error = 0
        x_error_sum = 0
        y_error_sum = 0

        box = scidata[starty-boxsize:starty+1+boxsize,startx-boxsize:startx
            +1+boxsize]

        for i in range(0,2*boxsize+1):
            for j in range(0,2*boxsize+1):
                if box[i,j] <> 0:
                    r_x = abs(j - coords[1])
                    r_y = abs(i - coords[0])
                    x_error = x_error + ((r_x/sum_normal) * average_stddev)
                        **2
                    y_error = y_error + ((r_y/sum_normal) * average_stddev)
                        **2
                    x_error_sum = x_error_sum + ((r_x/sum_normal) *
                        average_stddev)
                    y_error_sum = y_error_sum + ((r_y/sum_normal) *
                        average_stddev)

        x_error = math.sqrt(x_error)
        y_error = math.sqrt(y_error)

        #Resulting uncertainty:

        x_uncer = math.sqrt(x_error**2 + x_error_box**2)
        y_uncer = math.sqrt(y_error**2 + y_error_box**2)

        return x_result,y_result,x_uncer,y_uncer


def remove_single_pixels(data_array):

    #pixel am Rand des arrays werden nicht removed

    print "removing lone pixels..."

    x_range = int(data_array.shape[1])
    y_range = int(data_array.shape[0])

    test_sum = 0

    for h in range(1,y_range-1):
        for l in range(1,x_range-1):
            if data_array[h,l] <> 0:
```

```
        test_sum = data_array[h-1,l] + data_array[h,l-1] +
            data_array[h+1,l] + data_array[h,l+1] + data_array[h
            -1,l-1] + data_array[h+1,l+1] + data_array[h-1,l+1] +
            data_array[h+1,l-1]
        if test_sum == 0:
            data_array[h,l] = 0

    return data_array
```

A.3 LSMC Orbit Fit

```
#————————————————————
# Import Modules:
#————————————————————
from __future__ import division
from scipy import *
from pylab import *
from math import *
from numpy import *
from dates import *
from scipy import optimize
import random as rn
import numpy
import os
import matplotlib.cm as cm
from pylab import figure, show
import copy


#————————————————————
# allgemeine Variablen:
#————————————————————

pi = 3.14159265358979323846264338327950
G = 2.959122083e-4 #(AU M_sun days)
mesh = 0.005


#————————————————————
# Funktionen zur Orbitberechnung
#————————————————————

def arcsectoau(arcsec, parallax):
    parallax = parallax / 1000
    parsec = 1/parallax
    au = arcsec * parsec
    return au


# Berechnung der Orbit Periode aus Masse und a:
```

123

```
def periode(mass, distance, a):
    a = arcsectoau(a, distance)
    return math.sqrt(4*(pi**2)*(a**3)/(G * mass))

# Berechnung der mean anomaly:

def mean_anom(t, T_0, P):
    # t is time, T_0 is time of periastron, P is orbital period
    M = math.degrees((t - T_0) * 2 * pi / P)
    if M < 0:
        M = math.fmod(M, 360) + 360
    else:
        M = math.fmod(M, 360)

    return M

# Berechnung der eccentric anomaly:

def ecc_anom(M, e):
    # M is mean anomaly, e is eccentricity of orbit
    M = math.radians(M)
    E_n = M + e * sin(M) + (e**2 / M) * sin (2*M) # first approximation (
        aus Andreas Alzner chapter 7)
    E_n1 = E_n + (M - E_n + e*sin(E_n))/(1-e*cos(E_n))
    counter = 1

    while ((abs(E_n - E_n1) > 1e-5) and (counter < 50)):
        #print "E_n:" + str(E_n)
        counter = counter + 1
        E_n = E_n1
        E_n1 = E_n + (M - E_n + e*sin(E_n))/(1-e*cos(E_n))

    return math.degrees(E_n1)

# Berechnung der thiele-innes elemente:

def thiele_elements(a, i, node, peri):
    # a is semimayor axis, i is inclination, node is gross omega, peri is
        klein omega

    i = math.radians(i)
    node = math.radians(node)
    peri = math.radians(peri)

    A = a*(cos(peri)*cos(node) - sin(peri)*sin(node)*cos(i))
    B = a*(cos(peri)*sin(node) + sin(peri)*cos(node)*cos(i))
    F = a*(-sin(peri)*cos(node) - cos(peri)*sin(node)*cos(i))
```

```python
    G = a*(-sin(peri)*sin(node) + cos(peri)*cos(node)*cos(i))

    return A,B,F,G

# Umrechnung von Polar zu Kartesischen Koordinaten:

def sep_projection_tu(datatuple):

    sep = datatuple[0]
    sep_err = datatuple[1]
    pa = datatuple[2]
    pa_err =datatuple[3]

    pa_err = radians(pa_err)
    delta_ra = 0
    delta_dec = 0

    if pa < 45:
        pa = radians(pa)
        delta_ra = sin(pa) * sep
        delta_dec = cos(pa) * sep
        delta_ra_err = abs(sin(pa)) * sep_err + abs(cos(pa)) * sep *
            pa_err
        delta_dec_err = abs(cos(pa)) * sep_err + abs(sin(pa)) * sep *
            pa_err
    if (pa < 90) & (pa >= 45):
        pa = radians(pa)
        delta_dec = sin(pi/2 - pa) * sep
        delta_dec_err = abs(sin(pi/2 - pa)) * sep_err + abs(cos(pi/2 - pa
            )) * sep * pa_err
        delta_ra = cos(pi/2 - pa) * sep
        delta_ra_err = abs(cos(pi/2 - pa)) * sep_err + abs(sin(pi/2 - pa)
            ) * sep * pa_err
    if (pa < 135) & (pa >= 90):
        pa = radians(pa)
        delta_dec = -sin(pa - pi/2) * sep
        delta_dec_err = abs(sin(pa - 90)) * sep_err + abs(cos(pa-90)) *
            sep * pa_err
        delta_ra = cos(pa - pi/2) * sep
        delta_ra_err = abs(cos(pa - pi/2)) * sep_err + abs(sin(pa-pi/2))
            * sep * pa_err
    if (pa < 180) & (pa >= 135):
        pa = radians(pa)
        delta_ra = sin(pi - pa) * sep
        delta_ra_err = abs(sin(pi - pa)) * sep_err + abs(cos(pi - pa)) *
            sep * pa_err
        delta_dec = -cos(pi - pa) * sep
```

```
        delta_dec_err = abs(cos(pi − pa)) ∗ sep_err + abs(sin(pi − pa)) ∗
            sep ∗ pa_err
    if (pa < 225) & (pa >= 180):
        pa = radians(pa)
        delta_ra = −sin(pa − pi) ∗ sep
        delta_ra_err = abs(sin(pa − pi)) ∗ sep_err + abs(cos(pa − pi)) ∗
            sep ∗ pa_err
        delta_dec = −cos(pa − 180) ∗ sep
        delta_dec_err = abs(cos(pa − pi)) ∗ sep_err + abs(sin(pa − pi)) ∗
            sep ∗ pa_err
    if (pa < 270) & (pa >= 225):
        pa = radians(pa)
        delta_dec = −sin(1.5∗pi − pa) ∗ sep
        delta_dec_err = abs(sin(1.5∗pi − pa)) ∗ sep_err + abs(cos(1.5∗pi
            − pa)) ∗ sep ∗ pa_err
        delta_ra = −cos(1.5∗pi − pa) ∗ sep
        delta_ra_err = abs(cos(1.5∗pi − pa)) ∗ sep_err + abs(sin(1.5∗pi −
            pa)) ∗ sep ∗ pa_err
    if (pa < 315) & (pa >= 270):
        pa = radians(pa)
        delta_dec = sin(pa − 1.5∗pi) ∗ sep
        delta_dec_err = abs(sin(pa − 1.5∗pi)) ∗ sep_err + abs(cos(pa −
            1.5∗pi)) ∗ sep ∗ pa_err
        delta_ra = −cos(pa − 1.5∗pi) ∗ sep
        delta_ra_err = abs(cos(pa − 1.5∗pi)) ∗ sep_err + abs(sin(pa −
            1.5∗pi)) ∗ sep ∗ pa_err
    if pa >= 315:
        pa = radians(pa)
        delta_ra = −sin(2∗pi − pa) ∗ sep
        delta_ra_err = abs(sin(2∗pi − pa)) ∗ sep_err + abs(cos(2∗pi − pa)
            ) ∗ sep ∗ pa_err
        delta_dec = cos (2∗pi − pa) ∗ sep
        delta_dec_err = abs(cos(2∗pi − pa)) ∗ sep_err + abs(sin(2∗pi − pa
            )) ∗ sep ∗ pa_err

    return (delta_ra, delta_ra_err, delta_dec, delta_dec_err)


#—————————————————————————————
#Orbitfit mit vorgegebener Systemmasse
#—————————————————————————————

# Funktion zur zufaelligen Erzeugung von Orbitelementen aus
    gleichfoermiger Verteilung

def random_elements_mass_restricted(o_e_lim):
    #list of lists in der Reihenfolge: o_e=[a, i, node, peri, e, T_0]
    o_e = []
    for l in range(0, len(o_e_lim)):
```

126

```
            o_e.append(rn.uniform(o_e_lim[l][0],o_e_lim[l][1]))
    return o_e
```

Funktion zur Berechnung von Ra und Dec zu gegebenen Zeitpunkten aus Orbitelementen

```
def orbit_xy_fit_mass_restricted(o_e,mass_star,parallax_star,time_array):
    a = o_e[0]
    i = o_e[1]
    node = o_e[2]
    peri = o_e[3]
    e = o_e[4]
    T_0 = o_e[5]
    P = periode(mass_star,parallax_star,a)

    A,B,F,G = thiele_elements(a,i,node,peri)

    M = []
    E =[]

    for t in time_array:
        M.append(mean_anom(t,T_0,P))
        M_0 = mean_anom(t,T_0,P)
        E.append(math.radians(ecc_anom(M_0,e)))

    X = cos(E) − e
    Y = sqrt(1−e**2) * sin(E)

    x = A*X + F*Y
    y = B*X + G*Y

    return y,x
```

Funktion zur Berechnung von Differenzen zwischen Messungen und Orbitpunkten aus Orbitelementen

```
def orbit_error_func_mass_restricted(o_e,o_e_lim,mass_star,parallax_star,
    t,x,x_err,y,y_err):

    #————————————————————
    # boundaries
    # o_e=[a,i,node,peri,e,T_0]
    #————————————————————

    if o_e[0] < o_e_lim[0][0]: o_e[0] = o_e_lim[0][0]
    if o_e[0] > o_e_lim[0][1]: o_e[0] = o_e_lim[0][1]
    if o_e[1] < o_e_lim[1][0]: o_e[1] = o_e_lim[1][0]
    if o_e[1] > o_e_lim[1][1]: o_e[1] = o_e_lim[1][1]
```

```
if o_e[2] < o_e_lim[2][0]: o_e[2] = o_e_lim[2][0]
if o_e[2] > o_e_lim[2][1]: o_e[2] = o_e_lim[2][1]
if o_e[3] < o_e_lim[3][0]: o_e[3] = o_e_lim[3][0]
if o_e[3] > o_e_lim[3][1]: o_e[3] = o_e_lim[3][1]
if o_e[4] < o_e_lim[4][0]: o_e[4] = o_e_lim[4][0]
if o_e[4] > o_e_lim[4][1]: o_e[4] = o_e_lim[4][1]
if o_e[5] < o_e_lim[5][0]: o_e[5] = o_e_lim[5][0]
if o_e[5] > o_e_lim[5][1]: o_e[5] = o_e_lim[5][1]


return numpy.array((list(abs((x - orbit_xy_fit_mass_restricted(o_e,
    mass_star, parallax_star, t)[0]) / x_err)) + list(abs((y -
    orbit_xy_fit_mass_restricted(o_e, mass_star, parallax_star, t)[1]) /
    y_err))))**2

# Fitfunktion:

def fit_orbit_mc_mass_restricted_data_dump(t, x, x_err, y, y_err, o_e_lim,
    mass_star, parallax_star, path, Multiplier, NoR):

    fits_list = []
    chi_list =[]

    for z in range(0, Multiplier):

        chi_squr = []
        all_fits = []

        for l in range(0, NoR, 1):
            print z, ".", l
            o_e_guess = random_elements_mass_restricted(o_e_lim)
            fitparam_temp = optimize.leastsq(
                orbit_error_func_mass_restricted, o_e_guess[:], args=(
                o_e_lim, mass_star, parallax_star, t, x, x_err, y, y_err), maxfev
                =100, factor=0.1)
            chi = (orbit_error_func_mass_restricted(fitparam_temp[0],
                o_e_lim, mass_star, parallax_star, t, x, x_err, y, y_err))
            chi_squr_temp = sum(chi)
            chi_squr.append(chi_squr_temp)
            all_fits.append(fitparam_temp[0])

        FILE = open(os.path.join(path, "all_fits_" + str(z) +".txt"), "w")
        FILE_chi = open(os.path.join(path, "all_chi_" + str(z) +".txt"), "w
            ")

        fits_list.append(os.path.join(path, "all_fits_" + str(z) +".txt"))
        chi_list.append(os.path.join(path, "all_chi_" + str(z) +".txt"))

        for r in range(0, NoR, 1):
```

```
                FILE. writelines ( str ( list ( all_fits [ r ] ) ) . strip ( ' [ ] ' ) + "\n" )
                FILE_chi . writelines ( str ( chi_squr [ r ] ) + "\n" )

        FILE . close ( )
        FILE_chi . close ( )

    f = open ( os . path . join ( path , "all_fits_combined . txt" ) , "w" )
    for file in fits_list :
        f . write ( open ( file ) . read ( ) )
    f . close ( )

    f = open ( os . path . join ( path , "all_chi_combined . txt" ) , "w" )
    for file in chi_list :
        f . write ( open ( file ) . read ( ) )
    f . close ( )

    return

# Wrapper fuer die Fit Funktion :

def get_orbitfit_mc_mass_restricted ( file , o_e_lim , mass_star , parallax_star ,
    path , Multiplier , NoR ) :
    data = open ( file , "r" )
    lines = data . readlines ( )

    datapoints = [ ]
    ra = [ ]
    dec = [ ]
    ra_err = [ ]
    dec_err = [ ]
    epochs = [ ]
    Julian = [ ]

    for line in lines :
        datapoint = list ( str ( s ) for s in line . split ( ',' ) )
        for i in range ( 0 , 4 ) : datapoint [ i ] = float ( datapoint [ i ] )
        a = list ( sep_projection_tu ( tuple ( datapoint [ 0 : 4 ] ) ) )
        a . append ( datapoint [ 4 ] . strip ( "\n" ) )
        datapoints . append ( a )

    for l in datapoints :
        ra . append ( l [ 0 ] )
        dec . append ( l [ 2 ] )
        ra_err . append ( l [ 1 ] )
        dec_err . append ( l [ 3 ] )
        Julian . append ( l [ 4 ] )
        epochs . append ( epoch ( l [ 4 ] ) )
```

```
for l in range(0,len(Julian),1):
    Julian[l] = julian_date(Julian[l].split('.')[2],Julian[l].split('
        .')[1],Julian[l].split('.')[0],0,0,0)

data.close()

fit_orbit_mc_mass_restricted_data_dump(array(Julian),array(ra),array(
    ra_err),array(dec),array(dec_err),o_e_lim,mass_star,parallax_star,
    path,Multiplier,NoR)

return
```

A.4 Dynamic Range

```
#————————————————————————
#modul − import
#————————————————————————

from __future__ import division
import pyfits
import math
import matplotlib
import numpy as np
import sys
from scipy import *
from pylab import *
import os
import itertools
import scipy.interpolate as interpolate


#————————————————————————
#functions for dynamic range calculation
#————————————————————————

def return_dynamic_range_scale(pic, peakx, peaky, pixelscale, boxsize,
    s_n):

    file = pyfits.open(pic)
    header = file[0].header
    scidata = file[0].data

    maxpix_x=header["naxis1"]
    maxpix_y=header["naxis2"]

    if (maxpix_x < maxpix_y): maxpix = maxpix_x
    if (maxpix_x >= maxpix_y): maxpix = maxpix_y
```

```python
# peakintensitaet ermitteln:
if ((peaky-1-boxsize > 0) & (peaky-1+boxsize < maxpix-1) & (peakx-1-
    boxsize > 0) & (peaky-1+boxsize < maxpix-1)):
    peak = np.amax(scidata[peaky-1-boxsize:peaky-1+boxsize, peakx-1-
        boxsize:peakx-1+boxsize])
else:
    sys.exit("Boxsize violates image boundaries")

# noise Messungen: (i ist x und j ist y....immer dran denken das ist
    in python [y,x])
mag = []
dist = []


for i in range(boxsize, maxpix-1-boxsize, 1):
    for j in range(boxsize, maxpix-1-boxsize, 1):
        #distance = sqrt((peakx-1-i)**2+(peaky-1-j)**2)
        distance = sqrt((peakx-i)**2+(peaky-j)**2) * pixelscale
        if (distance < 5.1):
            noise = np.std(scidata[j-boxsize:j+boxsize, i-boxsize:i+
                boxsize])
            deltamag = 2.5 * log10(peak/noise) - 2.5 * log10(s_n)
            mag.append(deltamag)
            dist.append(distance)

temp = []
mag_av = []
dist_av = []

dist = np.array(dist)
ind=dist.argsort()
mag=np.array(mag)
mag = mag[ind]
dist= dist[ind]

dist_temp=dist[0]
dist_av.append(dist[0])

for l in range(0, len(mag)-1, 1):
    if (abs(dist_temp - dist[l]) < 0.05):
        temp.append(mag[l])
    else:
        dist_temp = dist[l]
        dist_av.append(dist[l])
        mag_av.append(np.average(temp))
        temp = []
mag_av.append(np.average(temp))

return dist_av, mag_av
```

```python
def return_dynamic_range_subtracted_scale(pic, peak_val ,peakx, peaky,
    pixelscale , boxsize , s_n):

    file = pyfits.open(pic)
    header = file[0].header
    scidata = file[0].data

    maxpix_x=header["naxis1"]
    maxpix_y=header["naxis2"]

    if (maxpix_x < maxpix_y): maxpix = maxpix_x
    if (maxpix_x >= maxpix_y): maxpix = maxpix_y

    # peakintensitaet ermitteln:
    peak = peak_val

    # noise Messungen: (i ist x und j ist y....immer dran denken das ist
        in python [y,x])
    mag = []
    dist = []

    for i in range(boxsize ,maxpix-1-boxsize ,1):
        for j in range(boxsize ,maxpix-1-boxsize ,1):
            #distance = sqrt((peakx-1-i)**2+(peaky-1-j)**2)
            distance = sqrt((peakx-i)**2+(peaky-j)**2) * pixelscale
            if (distance < 5.2): # hier die maximale distance aendern
                noise = np.std(scidata[j-boxsize:j+boxsize ,i-boxsize:i+
                    boxsize])
                deltamag = 2.5 * log10(peak/noise) - 2.5 * log10(s_n)
                mag.append(deltamag)
                dist.append(distance)

    temp = []
    mag_av = []
    dist_av = []

    dist = np.array(dist)
    ind=dist.argsort()
    mag=np.array(mag)
    mag = mag[ind]
    dist= dist[ind]

    dist_temp=dist[0]
    dist_av.append(dist[0])

    for l in range(0,len(mag)-1,1):
        if (abs(dist_temp - dist[l]) < 0.05):
```

```
                    temp.append(mag[l])
            else:
                dist_temp = dist[l]
                dist_av.append(dist[l])
                mag_av.append(np.average(temp))
                temp = []
    mag_av.append(np.average(temp))

    return dist_av, mag_av


#————————————————————————
#functions for dynamic range plots
#————————————————————————


def makeplot_dynamic_range_model(filename, modelfile, abs_starmag,
    dist_av, mag_av, sep = 1, mass = 0.076, plot_mass = True):

    #erwartet ein modelfile der Form :"mass_in_m_sun
        abs_mag_in_right_band"

    model = open(modelfile)
    lines = model.readlines()

    mod_mass = float(lines[0].split()[0])
    mod_mag = float(lines[0].split()[1])


    if plot_mass:
        # sucht das mass / mag paar aus dem Modelfile, das am besten zum
            "mass" argument passt
        help = abs(mod_mass-mass)
        for l in lines:
            if (abs(float(l.split()[0]) - mass) < help):
                mod_mass = float(l.split()[0])
                help = abs(float(l.split()[0]) - mass)
                mod_mag = float(l.split()[1])
        print mod_mass
        print mod_mag
        # sucht den magwert in der dynamic range Kurve der am naechsten
            am Modelwert liegt
        help = mod_mag
        for l in range(0,len(dist_av),1):
            if (abs(mod_mag - (mag_av[l] + abs_starmag)) < help):
                draw_mag = mag_av[l]
                help = abs(mod_mag - (mag_av[l] + abs_starmag))
                draw_sep = dist_av[l]

    model_line_sep = arange(0,dist_av[-1]+0.1,0.1)
    model_line_mag = arange(0,mag_av[-1]+1,0.1)
```

```
draw_sep_line = linspace(draw_sep,draw_sep,len(model_line_mag))
draw_mag_line = linspace(draw_mag,draw_mag,len(model_line_sep))

plt.figure()
plt.ylabel("$\mathrm{\Delta␣I␣\␣[mag]}$")
plt.xlabel("$\mathrm{separation␣\␣[arcsec]}$")
plot(dist_av,mag_av,"−")
plot(model_line_sep,draw_mag_line,"k—")
plot(draw_sep_line,model_line_mag,"k—")
ax = gca()

ax.annotate(str(mod_mass) + "$\mathrm{M_{\odot}}$", xy=(dist_av[−1] −
    1, draw_mag − 0.2), xytext=None,
arrowprops=None,)

#ax.set_ylim(ax.get_ylim()[::−1])
#ax.set_ylim(ax.get_ylim()[mag_av[−1]+0.5,0])
ylim([mag_av[−1]+0.5,0])
xlim([0,dist_av[−1]])
savefig(filename)
return
```

B Curiculum Vitae

Personal:

Name	Dipl.-Phys. Christian Ginski
Date of Birth:	15th April 1985
Nationality:	German
Office Adress:	Astrophysikalisches Institut und Universitätssternwarte
	Schillergässchen 2
	07745 Jena
e-mail:	ginski@astro.uni-jena.de

Education:

2009 - Present	PhD Student at the Astrophysical Institute and University Observatory Jena
	Topic: Direct imaging of substellar companions
	Supervisor: Prof. Dr. rer. nat. Ralph Neuhäuser
2009	Diploma Thesis at AIU Jena (grade: 1.7)
	Subject: Search for substellar companions around young stars with the Hubble Space Telescope
2003 - 2009	Study of physics at the Friedrich-Schiller-University Jena
1995 - 2003	Ernst-Abbe-Gymnasium Jena (High School)
	Abitur (High School Diploma) (grade: 1.1)

Languages:

German	native speaker
English	fluent, spoken daily
Latin	6 years of High School education
	certificate: Großes Latinum (grade: 1.0)

Research Interests:

- direct imaging of substellar companions

- multiplicity study of exoplanet hosts

- orbital dynamics

- extrasolar planet transit observations

- optical observations of isolated neutron stars

Teaching Experience:

- teaching assistant in physics laboratory

- teaching assistant in astronomical observations practical training

- seminar leader of "Astronomical observation techniques" seminar

- assistant in "Introduction to astronomy"

Public Presentations:

- "Astronomie heute und morgen" (german) lecture for german high school students 2009

- "Der Computer in der modernen Astronomie" (german) at the Urania Observatory Jena for the Night of Museums 2010

- "Deep AO imaging of substellar companions in beta pic" at "Planet Formation and Evolution" conference in Göttingen 2011

- "Orbital Motion of the Brown Dwarf Binary HD130948BC around its Primary" at the annual meeting of the Astronomische Gesellschaft in Heidelberg 2011

Observing Experience (as Proposal PI and/or Observer):

- 60/90 cm telescope of the AIU Jena for photometry and spectroscopy in the VIS ($>$ 100 nights)

- Calar Alto 2.2 m telescope for lucky imaging and photometry in the VIS

- ESO LaSilla NTT for wide field imaging in the NIR

- Subaru 8 m telescope for adaptive optics high resolution imaging in the NIR

Other:

- programming skills in Python, C and Visual Basic

- knowledge of standard astronomical software such as IRAF, MIDAS, GAIA, Eclipse

- 5 years of database administration at Asclepion Laser Technologies GmbH (2004-2009)

- project leader of AIU webpage redesign and implementation (www.astro.uni-jena.de)

- member of the "Deutsche Physikalische Gesellschaft"

C Publication List

C.1 Scientific papers

Ginski, C., Neuhäuser, R., Mugrauer, M., Schmidt, T. O. B., Adam, C. (2012). Orbital motion of the binary brown dwarf companions HD 130948 BC around their host star. *Monthly Notices of the Royal Astronomical Society*, submitted.

Ginski, C., Mugrauer, M., Seeliger, M., Eisenbeiss, T. (2012). A lucky imaging multiplicity study of exoplanet host stars. *Monthly Notices of the Royal Astronomical Society*, 421, 2498.

Mugrauer, M., Röll, T., **Ginski, C.**, Vogt, N., Neuhäuser, R., Schmidt, T. O. B. (2012). New observations of the PZ Tel system, its sub-stellar companion and debris disc. *Monthly Notices of the Royal Astronomical Society*, accepted.

The YETI Collaboration, Chen, W. P., Hu, S. C.-L., Errmann, R., Adam, C., Baar, S., Berndt, A., Bukowiecki, L., Dimitrov, D. P., Eisenbeiß, T., Fiedler, S., **Ginski, C.**, Gräfe, C., Guo, J. K., Hohle, M. M., Hsiao, H. Y., Janulis, R., Kitze, M., Lin, H. C., Lin, C. S., Maciejewski, G., Marka, C., Marschall, L., Moualla, M., Mugrauer, M., Neuhäuser, R., Pribulla, T., Raetz, S., Röll, T., Schmidt, E., Schmidt, J., Schmidt, T. O. B., Seeliger, M., Trepl, L., Briceño, C., Chini, R., Jensen, E. L. N., Nikogossian, E. H., Pandey, A. K., Sperauskas, J., Takahashi, H., Walter, F. M., Wu, Z.-Y., Zhou, X. (2012). A Possible Detection of Occultation by a Proto-planetary Clump in GM Cephei. *Astrophysical Journal*, 751, 118.

Neuhäuser, R., **Ginski, C.**, Schmidt, T. O. B., Mugrauer, M. (2011). Further deep imaging of HR 7329 A (η Tel A) and its brown dwarf companion B. *Monthly Notices of the Royal Astronomical Society*, 416, 1430.

Moualla, M., Schmidt, T. O. B., Neuhäuser, R., Hambaryan, V. V., Errmann, R., Trepl, L., Broeg, C., Eisenbeiss, T., Mugrauer, M., Marka, C., Adam, C., **Ginski, C.**, Pribulla, T., Rätz, S., Schmidt, J., Berndt, A., Maciejewski, G., Röll, T., Hohle, M. M., Tetzlaff, N., Fiedler, S., Baar, S. (2011). A new flare star member candidate in the Pleiades cluster. *Astronomische Nachrichten*, 332, 661.

Neuhäuser, R., Errmann, R., Berndt, A., Maciejewski, G., Takahashi, H., Chen, W. P., Dimitrov, D. P., Pribulla, T., Nikogossian, E. H., Jensen, E. L. N., Marschall, L., Wu, Z.-Y., Kellerer, A., Walter, F. M., Briceño, C., Chini, R., Fernandez, M., Raetz, S., Torres, G., Latham, D. W., Quinn, S. N., Niedzielski, A., Bukowiecki, Ł., Nowak, G.,

Tomov, T., Tachihara, K., Hu, S. C.-L., Hung, L. W., Kjurkchieva, D. P., Radeva, V. S., Mihov, B. M., Slavcheva-Mihova, L., Bozhinova, I. N., Budaj, J., Vaňko, M., Kundra, E., Hambálek, Ľ., Krushevska, V., Movsessian, T., Harutyunyan, H., Downes, J. J., Hernandez, J., Hoffmeister, V. H., Cohen, D. H., Abel, I., Ahmad, R., Chapman, S., Eckert, S., Goodman, J., Guerard, A., Kim, H. M., Koontharana, A., Sokol, J., Trinh, J., Wang, Y., Zhou, X., Redmer, R., Kramm, U., Nettelmann, N., Mugrauer, M., Schmidt, J., Moualla, M., **Ginski, C.**, Marka, C., Adam, C., Seeliger, M., Baar, S., Roell, T., Schmidt, T. O. B., Trepl, L., Eisenbeiß, T., Fiedler, S., Tetzlaff, N., Schmidt, E., Hohle, M. M., Kitze, M., Chakrova, N., Gräfe, C., Schreyer, K., Hambaryan, V. V., Broeg, C. H., Koppenhoefer, J., Pandey, A. K. (2011). The Young Exoplanet Transit Initiative (YETI). *Astronomische Nachrichten*, 332, 547.

Mugrauer, M., Neuhäuser, R., **Ginski, C.**, Eisenbeiss, T. (2010). Multiplicity study of exoplanet host stars. *Highlights of Astronomy*, 15, 694.

Maciejewski, G., Dimitrov, D., Neuhäuser, R., Niedzielski, A., Raetz, S., **Ginski, C.**, Adam, C., Marka, C., Moualla, M., Mugrauer, M. (2010). Transit timing variation in exoplanet WASP-3b. *Monthly Notices of the Royal Astronomical Society*, 407, 2625.

Eisenbeiss, T., **Ginski, C.**, Hohle, M. M., Hambaryan, V. V., Neuhäuser, R., Schmidt, T. O. B. (2010). New photometry and astrometry of the isolated neutron star RX J0720.4-3125 using recent VLT/FORS observations. *Astronomische Nachrichten*, 331, 243.

Raetz, S., Vaňko, M., Mugrauer, M., Schmidt, T. O. B., Roell, T., Eisenbeiss, T., Hohle, M. M., Koeltzsch, A., **Ginski, C.**, Marka, C., Moualla, M., Tetzlaff, N., Broeg, C., Neuhäuser, R. (2009). Photometric analysis of the eclipsing binary 2MASS 19090585+4911585. *Astronomische Nachrichten*, 330, 504.

Neuhäuser, R., Koeltzsch, A., Raetz, S., Schmidt, T. O. B., Mugrauer, M., Young, N., Bertoldi, F., Roell, T., Eisenbeiss, T., Hohle, M. M., Vaňko, M., **Ginski, C.**, Rammo, W., Moualla, M., Broeg, C. (2009). Photometric monitoring of the young star Par 1724 in Orion. *Astronomische Nachrichten*, 330, 493.

Koeltzsch, A., Mugrauer, M., Raetz, S., Schmidt, T. O. B., Roell, T., Eisenbeiss, T., Hohle, M. M., Vaňko, M., **Ginski, C.**, Marka, C., Moualla, M., Schreyer, K., Broeg, C., Neuhäuser, R. (2009). Variability of young stars: Determination of rotational periods of weak-line T Tauri stars in the Cepheus-Cassiopeia star-forming region. *Astronomische Nachrichten*, 330, 482.

Raetz, S., Mugrauer, M., Schmidt, T. O. B., Roell, T., Eisenbeiss, T., Hohle, M. M., Koeltzsch, A., Vaňko, M., **Ginski, C.**, Marka, C., Moualla, M., Tetzlaff, N., Seifahrt, A., Broeg, C., Koppenhoefer, J., Raetz, M., Neuhäuser, R. (2009). Planetary transit observations at the University Observatory Jena: TrES-2. *Astronomische Nachrichten*, 330, 459.

Eisenbeiss, T., Moualla, M., Mugrauer, M., Schmidt, T. O. B., Raetz, S., Neuhäuser, R., **Ginski, C.**, Hohle, M. M., Koeltzsch, A., Marka, C., Rammo, W., Reithe, A., Roell, T., Vaňko, M. (2009). New brown dwarf candidates in the Pleiades. *Astronomische Nachrichten*, 330, 439.

Mugrauer, M., Hohle, M. M., **Ginski, C.**, Vanko, M., Freistetter, F. (2009). Follow-up observations of Comet 17P/Holmes after its extreme outburst in brightness end of October 2007. *Astronomische Nachrichten*, 330, 425.

C.2   Scientific talks

- "Deep AO imaging of substellar companions in beta pic" at "Planet Formation and Evolution" conference in Göttingen, 2011 February 15

- "Orbital Motion of the Brown Dwarf Binary HD130948BC around its Primary" at the annual meeting of the Astronomische Gesellschaft in Heidelberg, 2011 September 20

D Declaration of authenticity

I hearby declare on oath that I created this work independently without the help of any third party and only with the aids and literature indicated. All results taken from other sources are indicated as such and the sources are listed accordingly.

The following person was directly involved in the creation of content shown in this work as described:

- The astrometric calibration of the 2006 Calar Alto observations of HD 130948 was done by Dr. rer. nat. Tobias O. Schmidt.

There were no additional persons directly involved in the creation of the content shown in this work. In particular noone received any monetarily benefits to aid or assist in this work. This work has not been submitted in any form for another degree or diploma at any university or other institute of tertiary education be it domestic or foreign. I am aware of the doctoral regulations of the faculty for physics and astronomy of the Friedrich-Schiller-University Jena.

I declare on oath that I said the truth and nothing but the truth to my best knowledge.

Ich erkläre hiermit an Eides statt, dass ich die vorliegende Arbeit selbstständing und nur unter zu Hilfe nahme der angegebenen Hilfsmittel und Literatur erstellt habe. Alle Resultate die aus anderen Quellen stammen sind als solche gekennzeichnet und die entsprechenden Quellen angegeben.

Die folgende Person war in der beschriebenen Weise direkt an der Erstellung dieser Arbeit beteiligt:

- Die astrometrische Kalibration der 2006 Calar Alto Beobachtungsepoche wurde von Dr. rer. nat. Tobias O. Schmidt durchgeführt.

Weitere Personen waren an der Erstellung dieser Arbeit nicht direkt beteiligt. Insbesondere hat niemand durch mich monetäre Mittel für Leistungen erhalten, die im Zusammenhang mit dem Inhalt dieser Arbeit stehen.

Diese Arbeit wurde bisher nicht, ganz oder in Teilen, einer anderen in- oder ausländischen Prüfungsbehörde vorgelegt. Die Promotionsordnung der Physikalisch-Astronomischen Fakultät der Friedrich-Schiller-Universität Jena ist mir bekannt.

Ich erkläre das ich nach bestem Wissen und Gewissen die Wahrheit gesagt und nichts verschwiegen habe.

....
Ort, Datum   Unterschrift